Pontificia Universidad Católica del Perú

Escuela de Posgrado

Tesis de Maestría

Characterization of carbon based nanostructures for the detection of tuberculosis

Para obtener el grado de:

Master of Science (M. Sc.)

en Ingeniería y Ciencia de los Materiales

|	
Presentado por:	Paulo Edgardo Muñante Palacin
Fecha y Lugar de Nacimiento:	05/08/1987 Ica, Perú
Tutor Responsable (TU Ilmenau):	Prof. Dr.-Ing. Rolf Grieseler
Professor Responsable (TU Ilmenau):	Prof. Dr.-Ing. habil. Lothar Spieβ
Professor Responsable (PUCP):	Prof. Dr. Francisco Rumiche Zapata
Fecha y Lugar:	04/10/2017, Lima

Dedication

To God

"so is my word that goes out from my mouth:
It will not return to me empty,
but will accomplish what I desire
and achieve the purpose for which I sent it."
Isaiah 55:11
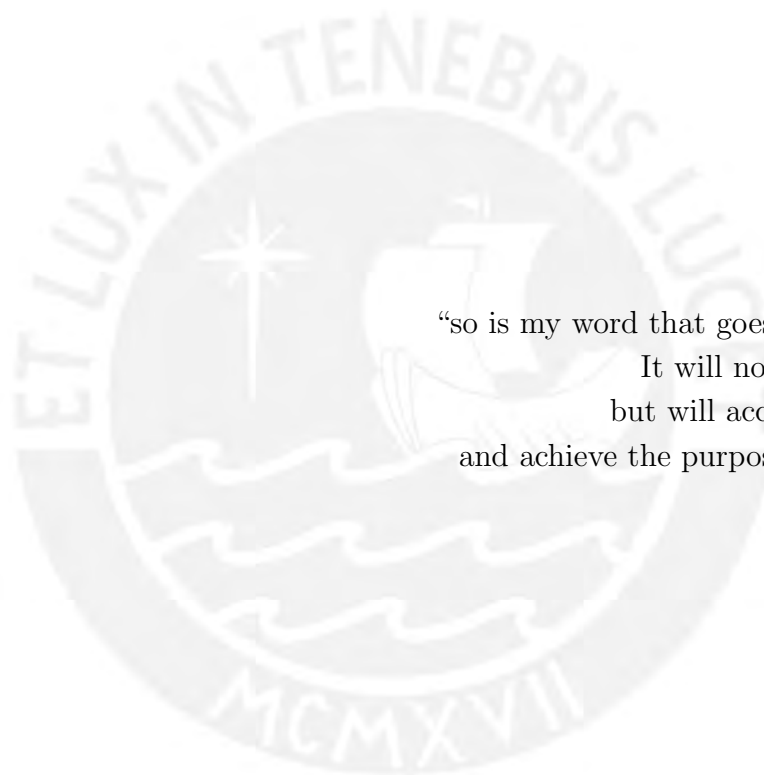
Acknowledgements

Primarily I want to thank God for the blessing of having allowed me to complete this stage of my life with the elaboration of this work, for the strength that gives us day by day and for guiding my life.

I would like to thank the institutes that allowed me to finish this work. To the financing provided by the "Proyecto de Innovación para la Competitividad" under the contract 202-Fincyt-IA-2013-Peru. To the TU-Ilmenau and PUCP and all the staff that form these great institutions.

I am deeply grateful to my supervisor, Dr. Francisco Rumiche, for allowing me to work in his research group and for all the support provided during all these years working with him and for his kind guidance.

I would like to express my deep gratitude to Dr. Rolf Grieseler for his useful courses, his suggestions, criticisms and guidance from the inception of my master project. I am thankful to Yana Krivoshapkina for her valuable help in AFM characterization.

I also wish to thank the Professors Roberto Lazarte and Paul Lean for the encouragement and supports.

Many thanks are given to Dr. Dominique Plee for his analysis and contribution in the research group, also to my friends Merlyn Rojas and Vanessa Estrada for all their help and collaboration in the development of this project.

Finally and most important, I want to thank infinitely (and can never be returned) all the support and affection received by my family: my parents Monica and Edgardo, Juan Pablo and Angie. And of course Maria Elena, the best of the companies, for her patience with love and having endured my months of writing.

To all those people who gave me their knowledge, motivated me to go forward and supported me throughout this stage of my life that culminates.

Contents

List of Figures

List of Tables

Abstract

Tuberculosis is a leading killing disease worldwide with more than 9 million people affected per year. Current diagnostic methods exhibit several disadvantages; one of the most promising alternatives to overcome this is the development of nanostructured diagnostic systems which are able to detect molecules associated with certain diseases. Graphene since its discovery has been the focus for the development of these sensing elements due to its excellent electronic properties.

In this work, a graphene-based field effect transistor (FET) has been developed for tuberculosis DNA detection, in order to set the basis for a diagnostic method that overcomes current limitations. The sensing elements composed of graphene monolayers were manufactured in the stages of annealing of the substrate, addition of the linker and functionalization with the addition of a probe DNA for tuberculosis detection. Additionally, two conditions for the sensing element were generated; one with the addition of a complementary DNA sequence ("DNA Target") and the other with a mismatched DNA sequence ("Non-complementary DNA"). The graphene and the transistor, in each stage of the manufacturing process, were structural, chemical and morphologically characterized by Raman Spectroscopy, Energy Dispersive X-ray Spectroscopy (EDS), Optical Microscopy, Laser Scanning Microscopy (LSM), Scanning Electron Microscopy (SEM) and Atomic Force Microscopy (AFM).

The results indicated an appropriate functionalization of the graphene surface with the linker, the immobilization of the probe tuberculosis DNA and the hybridization with the corresponding "DNA Target", demonstrated by observation of different homogeneous morphologies and an appropriate increase in the roughness in each stage of the manufacturing process. Also by the presence of characteristic peaks of nitrogenous bases and in the variation of graphene bands in the Raman spectrum. On the contrary, the sensor element with the "Non-complementary" showed an agglomeration of the molecules and segregation of salts on a heterogeneous surface. The results of the characterization are consistent with the electronic characteristics previously determined. This investigation contributes to a basis for the development of a tuberculosis detection system based on nanotechnology for clinical application.

Resumen

La tuberculosis es una de las principales enfermedades mortales en todo el mundo, con más de 9 millones de personas afectadas por año. Los métodos de diagnóstico actuales presentan varias desventajas; una de las alternativas más prometedoras para superar esto es el desarrollo de sistemas de diagnóstico nanoestructurados que son capaces de detectar moléculas asociadas con ciertas enfermedades. El grafeno desde su descubrimiento ha sido un foco para el desarrollo de estos elementos sensores debido a sus excelentes propiedades electrónicas.

En este trabajo, se ha desarrollado un transistor de efecto de campo basado en grafeno (FET) para la detección del ADN de la tuberculosis, con el fin de sentar las bases para un método de diagnóstico que supere las limitaciones actuales. Los elementos sensores compuestos de monocapas de grafeno se fabricaron en las etapas de recocido del sustrato, adición del linker y funcionalización con la adición de un probe ADN para la detección de tuberculosis. Adicionalmente, se generaron dos condiciones para los elementos de detección; uno con la adición de una secuencia de ADN complementaria ("DNA Target") y el otro con una secuencia de ADN no complementaria ("Non-complementary DNA"). El grafeno y el transistor, en cada etapa del proceso de fabricación, se caracterizaron estructural, química y morfológicamente por Espectroscopia Raman, Espectrometría de dispersión de energía de rayos X (EDS), Microscopía Óptica, Microscopía de Láser de Barrido (LSM), Microscopía Electrónica de Barrido (SEM) y Microscopía de Fuerza Atómica (AFM).

Los resultados indicaron una funcionalización apropiada de la superficie del grafeno con el linker, la inmovilización del probe ADN de tuberculosis y la hibridación con el correspondiente "DNA Target", demostrado por la observación de diferentes morfologías homogéneas y un aumento apropiado de la rugosidad en cada etapa del proceso de fabricación. También por la presencia de picos característicos de bases nitrogenadas y en la variación de las bandas de grafeno en el espectro Raman. Por el contrario, el elemento sensor con el "Non-complementary DNA" mostró una aglomeración de moléculas y segregación de sales sobre una superficie heterogénea. Los resultados de la caracterización son consistentes con las características electrónicas previamente realizadas. Esta investigación contribuye a dar una base para el desarrollo de un sistema de detección de la tuberculosis basado en la nanotecnología para uso clínico.

Zusammenfassung

Tuberkulose ist weltweit eine führende tödlichen Krankheiten mit mehr als 9 Millionen Neuinfektionen pro Jahr. Aktuelle diagnostische Methoden weisen mehrere Nachteile auf. Eine der vielversprechendsten Alternativen, um dies zu überwinden, ist die Entwicklung von nanostrukturierten Diagnosesystemen, die in der Lage werden, Moleküle zu erkennen, die mit bestimmten Krankheiten assoziiert sind. Seit seiner Entdeckung ist Graphen eine vielversprechende Möglichkeit für die Entwicklung dieser Sensorelemente aufgrund seiner hervorragenden elektronischen Eigenschaften.

In dieser Arbeit wurde ein Graphen-basierter Feldeffekttransistor (FET) für die Tuberkulose-DNA-Detektion entwickelt, um die Grundlage für ein diagnostisches Verfahren zu schaffen, das die gegenwärtigen Einschränkungen überwindet. Die Sensorelemente aus Graphen-monoschichten wurden in den Stufen: Glühen des Substrats, dem Zugeben des Linkers und der Funktionalisierung unter Zugabe einer Probe-DNA zur TB-Detektion hergestellt. Zusätzlich wurden zwei Sensorelemente hergestellt: Ein System mit der Zugabe einer komplementären DNA-Sequenz ("DNA Target") und die andere mit einer nicht übereinstimmenden DNA-Sequenz ("Non-complementary DNA"). Das Graphen und der Transistor wurden in jeder Stufe des Herstellungsprozesses strukturell, chemisch und morphologisch mittels Raman-Spektroskopie, energiedispersive Röntgenspektroskopie (EDS), Optische Mikroskopie, Laserscanning-Mikroskopie (LSM), Rasterelektronenmikroskopie (SEM) und Rasterkraftmikroskopie (AFM) charakterisiert.

Die Ergebnisse zeigten eine geeignete Funktionalisierung der Graphenoberfläche mit dem Linker, die Immobilisierung der Sonden - Tuberkulose - DNA und die Hybridisierung mit dem entsprechenden ("DNA Target"), nachgewiesen durch Beobachtung unterschiedlicher homogener Morphologien und eine entsprechende Erhöhung der Rauhigkeit in jedem Stadium des Herstellungsprozesses sowie durch die Anwesenheit von charakteristischen Peaks der stickstoffhaltigen Basen in der energiedispersiven Röntgenspektroskopie und durch die Variation von Graphen-Absorptionsbänder im Raman-Spektrum. Im Gegensatz dazu zeigte, das Sensorelement mit der "nicht-komplementären DNA" eine Agglomeration der Moleküle und die Segregation von Salzen auf einer heterogenen Oberfläche. Die Ergebnisse der Charakterisierung stimmen mit den zuvor durchgeführten elektronischen Merkmalen überein. Diese Untersuchung bildet die Grundlage für die Entwicklung eines Tuberkulose-Nachweissystems auf der Basis der Nanotechnologie für den klinischen Einsatz.

1 Introduction

1.1 Motivation

Tuberculosis (TB) is one of the major health problems globally and is considered to be a lethal and common disease caused by Mycobacterium tuberculosis [1]. A concern has arised lately since it is known to that tuberculosis is associated to other diseases and health issues such as HIV, diabetis, smoking, indoor air pollution, alcoholism, and malnutrition. TB affects nearly 9.4 million patients and resulting in 1.7 million deaths worldwide in 2011 [2]. It is estimated that in Peru a large percentage of the population carries the bacteria. Due to the high incidence of TB it is necessary to find ways of effective detection and diagnosis.

The main current diagnostic methods, such as Ziehl-Neelsen stain and fluorescent staining, work with sputum samples and are based on staining bacilli acid-resistant (BAAR). These methods are explained in the manuals Bacteriology National Institute of Health (NIH) and the World Health Organization (WHO) [3]. Nevertheless; in practice, they require extensive and exhausting work of laboratory workers, who, at the same time, should have good experience and expensive equipment as well as infrastructure. [4, 5].

One of the most promising alternatives to overcome the limitations of current methods is the development of nanostructured diagnostic systems based on graphene, due to its particular characteristics and large surface area that makes it a suitable candidate for biomolecular sensing. Different investigations for the detection of biomolecules based on graphene have been reported [6, 7] and even the detection of TB by different methods [8, 9].

In recent years few studies have been reported showing graphene based field effect transistors (FET) as sensing elements to detect different molecules and biomolecules [10, 11].

In the present thesis we report on the structural, chemical and morphological characterization of a graphene based field effect transistor for detecting tuberculosis. The different effects involved in each stage of the manufacturing process of the sensing element were investigated.

1.2 General objective

To perform structural, chemical and morphological characterization of nanostructured graphene-based sensing elements for the detection of tuberculosis.

1.3 Specific objectives

- To fabricate of graphene-based sensing elements for the detection of tuberculosis.

- To characterize them using techniques that allow to evaluate structure, chemical composition and morphology.

- To enlighten the behavior of the aggregated molecules at each stage of the surface modification procedures of the sensing element.

1.4 Thesis organization

The content of this thesis is organized as follows:

- Chater 2 starts with a brief overview of the state of the art of graphene and how is used as a sensing element. Main characterization techniques are also described. Furthermore a summary of different characterizations performed to graphene based biosensors are detailed and finally, the diagnosis and problematic of Tuberculosis is shown.

- Chater 3 presents the experimental procedure explained in detail. The fabrication of the sensing elements is described step by step and also the materials used are presented. Then the main techniques of characterization and parameters are summarized.

- Chater 4 shows and discusses the results of the structural, chemical and morphological characterization of each stage of the manufacturing process and also its behavior as a sensing element.

- Chater 5 concludes this thesis by mentioning the most important conclusions and presents some suggestions for possible future work.

2 State of technology

2.1 Graphene

Carbon is the fourth most abundant chemical element in nature and constitutes one of the basic elements for life. It has unique capability for combining with other elements and is also widely used in industry for materials manufacturing. Carbon has different allotropy forms, some of the most important recently studied are:

- Graphite: Is a stack of graphene layers, is soft, optical opaque, chemical active and is a good electric conductor. The most important applications are pencil tips, electrodes, and solid lubricants [12].

- Fullerenes: In 1985, Harold Kroto, Robert Curl and Richard Smalley discovered the furellenes, they are molecules of nanometre-size spheres of wrapped-up graphene. Furellenes have been used for medical applications as substitutive ligans or in biosensors devices.

- Nanotubes: In 1991, Ijima reported the preparation of new cylindrical structures called carbon nanotubes [13]. They are made of rolled-up sheets of graphene. Applications include field emission devices, fuel cells, cold cathodes and ultrahigh-strengh structural materials [14].

- Graphene: Mother of all graphitic forms was discovered in 2004 by Andrey Gueim and Konstantin Novosiolov, who were awarded the nobel prize in 2010. Since then, the research of graphene has grown exponentially.

Figure 2.1 shows the similarities of the allotropy carbon forms and graphene.

Graphene is a two-dimensional mono layer of sp^2 bonded carbon atoms (Figure 2.2) arranged in a honeycomb crystal structure with two carbon atoms in each unit cell. The carbon atoms are densely packed with and atomic thickness of 3.4 Å[15]. The sp^2 hybrids of each carbon atom contribute to form σ bonds with three other carbon atoms in a trigonal planar structure. These strong bonds maintain the interatomic distance of 0.142 nm [16], the shortest distance of all the materials.
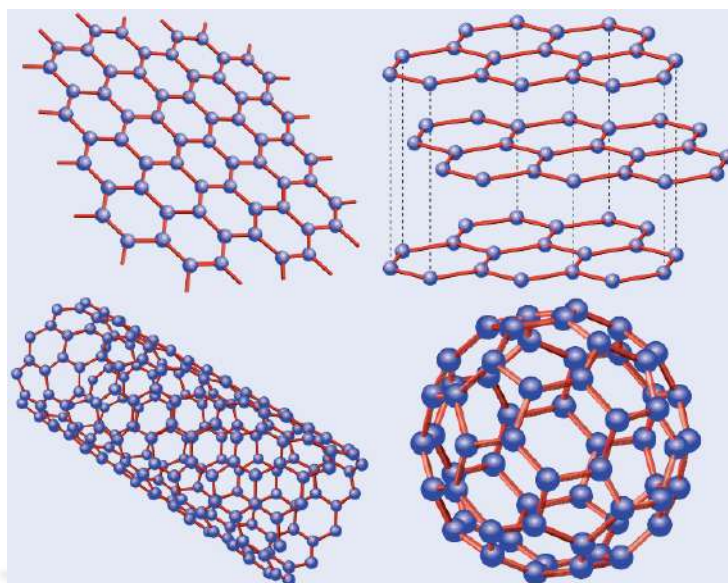
Figure 2.1: Graphene (top left) consists of a 2D hexagonal lattice of carbon atoms; graphite is a stack of graphene layers (top right); carbon nanotubes are rolled-up cylinders of graphene (bottom left); and a buckminsterfullerene (C60) molecule consists of graphene balled into a sphere by introducing some pentagons as well as hexagons into the lattice (bottom right). [14].
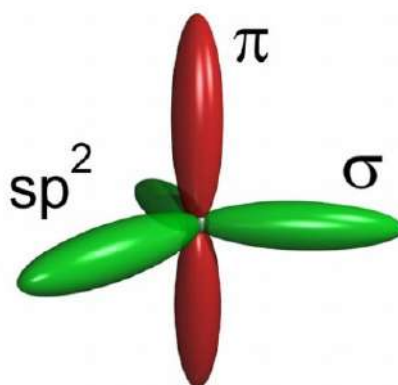
Figure 2.2: sp^2 and p orbitals of carbon atoms in graphene [17].

2.1.1 Properties

- Mechanical properties:
  Graphene has been reported to have the highest elastic modulus and strength, the breaking strength of graphene is 200 times higher than that for steel, making it the strongest material ever tested. Several researchers have determined by different kind of methods the intrinsic mechanical properties of the single, bilayer and multilayer graphene. A summarized list of the mechanical properties and methods to determine them are showed in Table 2.1.

Table 2.1: Mechanical properties of graphene. Modified from [18].

Method	Material	Mechanical properties	Reference
Nanoindentation in an AFM	Mono layer graphene	$E = 1 \pm 0.1$ TPa $\sigma_{int} = 130 \pm 10$ GPa at $\varepsilon_{int} = 0.25$	[19]
AFM	Mono layer Bilayer Tri-layer Graphene	$E = 1.02$ TPa; $\sigma = 130$ GPa $E = 1.04$ TPa; $\sigma = 126$ GPa $E = 0.98$ TPa; $\sigma = 101$ GPa	[20]
AFM	Stacks of graphene sheets (less than 5)	$E = 0.5$ TPa	[21]
Raman	Graphene	Strain $\sim 1.3\%$ in tension Strain $\sim 1.3\%$ in compression	[22]
Numerical simulations	Mono layer graphene	$E \geq 1$ TPa	[23]
Numerical simulations	Finite graphene sheets	$E \approx 1$ TPa; $\nu = 0.25$	[24]

- Thermal properties:
  The unique structure of graphene and its strong C-C bonding provides excellent thermal conductivity with low coefficient of thermal expansion, this properties are key factors for better performance and reliability of electronic components making graphene a good alternative for electronic devices where the considerable amount of heat generated during the device operation needs to be dissipated. The thermal properties of graphene are also greatly affected by phenomenon such as defect edge scattering [25] and isotopic doping [26] due to scattering or localization of phonons at the defect sites [27]. A summarized list of thermal properties and methods to determine them are shown in in

Table 2.2. where shows that graphene have higher thermal conductivity than graphene oxide and carbon nanotubes.

Table 2.2: Thermal properties of graphene and carbon allotropes based materials. Modified from [18].

Method	Material	Thermal conductivity	Reference
Thermal flash technique	Graphene oxide	~ 2000 W/mK	[28]
Microfabricated device heat transfer model	MWCNT	~ 3000 W/mK	[29]
Joule self-heating	Single wall CNT	~ 3500 W/mK	[30]
Electrical four-point measurement	Reduced graphene oxide flake	$0.14 - 0.87$ W/mK	[31]
Confocal micro-Raman spectroscopy	Single layer graphene	$4840 - 5300$ W/mK at RT	[32]
Confocal micro-Raman spectroscopy	Suspended graphene flake	$4100 - 4800$ W/mK at RT	[33]
Thermal measurement method	Single layer (suspended)	$3000 - 5000$ W/mK at RT (suspended)	[34]
Thermal measurement method	Single layer (on SiO$_2$ support)	600 W/mK at RT (on a SiO$_2$ support)	[34]

- Optical properties:
  Many reports confirmed that single layer graphene absorbs 2.3% of incident light over a broad wavelength range in spite of being just a monolayer (Figure 2.3) [35]. Also, graphene has been shown to transmit 97.7% of the total incident light [36] which are significant values for a single-atom thick material, likewise the optical contrast increase with increase in the number of layers of graphene [37]. These values describe the reason why graphene is almost transparent for the human eyes.
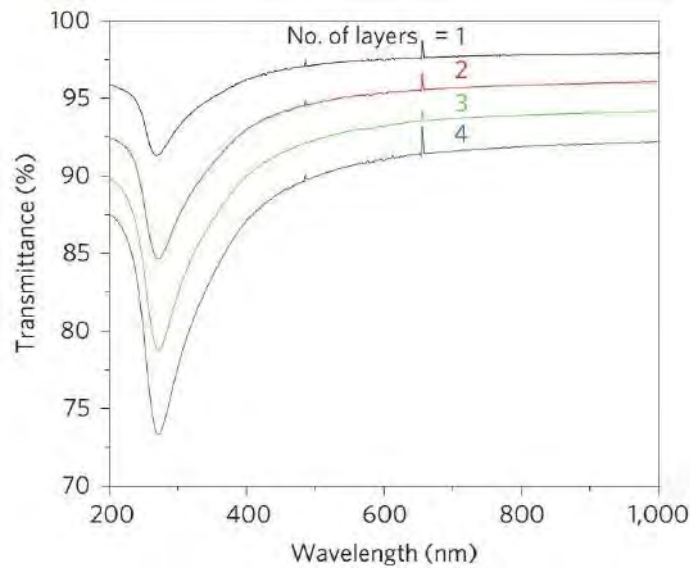
Figure 2.3: Representative of transmittance of different graphene layers. UV–vis spectra roll-to-roll layer-by-layer transferred graphene films on quartz substrates [35].

- Electrical transport property:

  In the same manner as the strong C-C bonding provides excellent thermal conductivity, it also gives excellent electrical conductivity. The metal or insulating properties of a material are determined by the position of the Fermi level(ε_f) and structure of electronic bands. The Fermi level corresponds to the highest occupied energy level. In Figure 2.4 the lowest unoccupied energy levels conform the conduction band (purple); the higher energy levels occupied, the valence band (fuchsia). In metals, the band of conduction and valence are overlapping. In non-metals, however, an energy gap that prevents the passage of electrons from one band to another appears. Graphene is a material out of the ordinary. Their electronic properties place it between metals and semiconductors [38].
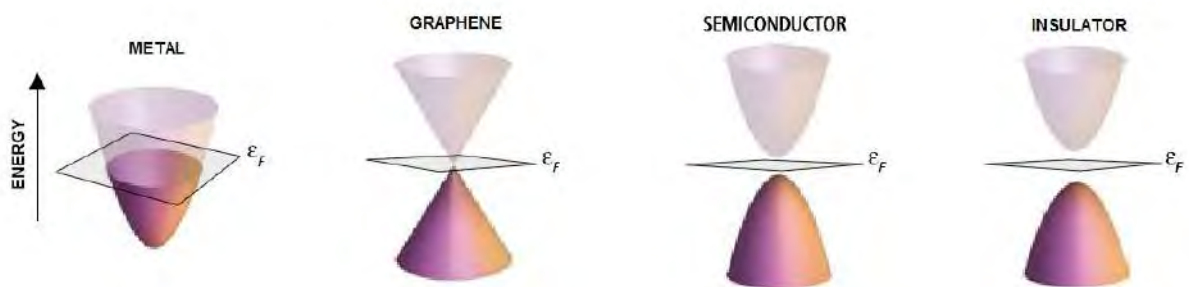
Figure 2.4: Dirac cones regarding the electronic properties. The cone below is the valence band (electrons), and the cone above is the conduction band (holes) [38].

High carrier mobilities have been reported for graphene, 15000 cm^2/Vs for graphene on

SiO$_2$ substrate [39], 25000 cm^2/Vs for epitaxial graphene [40] and higher than 200000 cm^2/Vs for suspended graphene [41, 42]. However, different scattering mechanisms, especially from charged impurity centers limit the mobility in electronic graphene devices [43].

2.1.2 Applications

The exceptional electrical conductivity and thermal properties of graphene can be useful not only in electronic devices but also in biomedical devices for measuring cell potential and as a substrate for conductive cell culture devices and biosensors [44, 45]. The transparent and flexible conductor is a great promise for solar cells [46] and touch panels for smartphones [47]. Also several investigations showed polymer matrix with dispersion of graphene powder for advanced composites [48, 49].

The 2D structure and presence of delocalized surface π electrons in graphene can be used for effective drug loading via hydrophobic interactions and $\pi - \pi$ stacking. Additionally, the large surface area of graphene allows the application for high density bio-functionalization via both covalent and non-covalent surface modification. Various studies have been made regarding the in-vivo behavior and bioactivity of graphene making graphene suitable for drug delivery, gene delivery and tissue engineering [50, 51].

The high carrier mobility in graphene sheets makes them attractive material for FETs [52]. A single molecule detection has been achieved, which demonstrates the potential high sensitivity of graphene-based sensors [53]. Chen et al. managed to fabricate and characterize a FET device for detecting DNA with graphene layers [54] and Huang et al. produced a graphene FET for detecting cellular activities, specifically Escherichia Coli [55].

The extraordinary mechanical properties also make graphene a suitable material for constructing Nanoelectromechanical Systems (NEMS) such as pressure sensors or resonators [56, 57] and also molecular sensors and electromechanical resonators [58, 59].

2.1.3 Synthesis methods

Different studies reported at least a dozen methods but basically there are two different approaches to prepare graphene. Exfoliation methods where graphene can be detached from an already existing graphite crystal and methods where graphene layer can be grown directly on a substrate surface.

- Mechanical exfoliation: In this method, graphene is detached from a graphite crystal using adhesive tape, graphite is made of sheets of graphene kept together by Van Der

Waals force. After peeling it off the graphite, this process can lead to multilayer and even single-layer graphene as it was done leading to its discovery [60].

Next, the graphene flakes are transferred onto a suitable substrate such as silicon dioxide on silicon with an oxide thickness of 90 nm or 300 nm in order to increase the contrast in visible range and to identify the graphene flakes [17, 61].

By this method is very difficult to obtain larger amount of graphene and is not suitable for industrial scale production.

- Epitaxial Growth on Silicon Carbide Single Crystal: This growth on surface method consists of sublimation of silicon atoms from the surface layers of silicon carbide (0001) substrate at the temperature of about 1300 °C in an ultrahigh vacuum environment and then cooling down [62, 63]. The produced graphene layers depend on the parameters used. Surface studies show that are strained with limited structural coherence length, 20 nm [64]. Therefore, the graphene is not perfectly homogeneous, due to defect or grain boundaries also high temperature and high cost of production are considered as serious disadvantage for application of this method.

- Chemical Vapour Deposition: A very popular growth technique is chemical vapour deposition. A transition metal film such as Ni, Co, Pt, Ir or Ru is used to decompose molecules of a hydrocarbon gas (methane, acetylene, propane etc) [65]. The temperatures and pressures depend on the metal substrate and gas type. Carbon atoms dissolve into the metal surface and then force to precipitate by cooling [65, 66, 67]. Transition metals are particularly appealing for obtaining large-area high quality graphene. This method is a promising technique used especially for flat displays and transparent electrode applications [68].

- Self Assembly of Soluble Graphene: Another growth technique is self assembly of soluble graphene where graphene sheets can be prepared by two-dimensional assembly of graphene suspended in organic solvent [69]. Although graphene obtained by this method has still relatively poor electrical quality, this technique shows the possibility of producing low cost and large-scale graphene for flexible and transparent electronics [61, 68].

In Figure 2.5 the most common methods of synthesis related to quality of graphene, cost and possible applications are shown. Table 2.3 shows that the properties of graphene vary according to the manufacturing process.
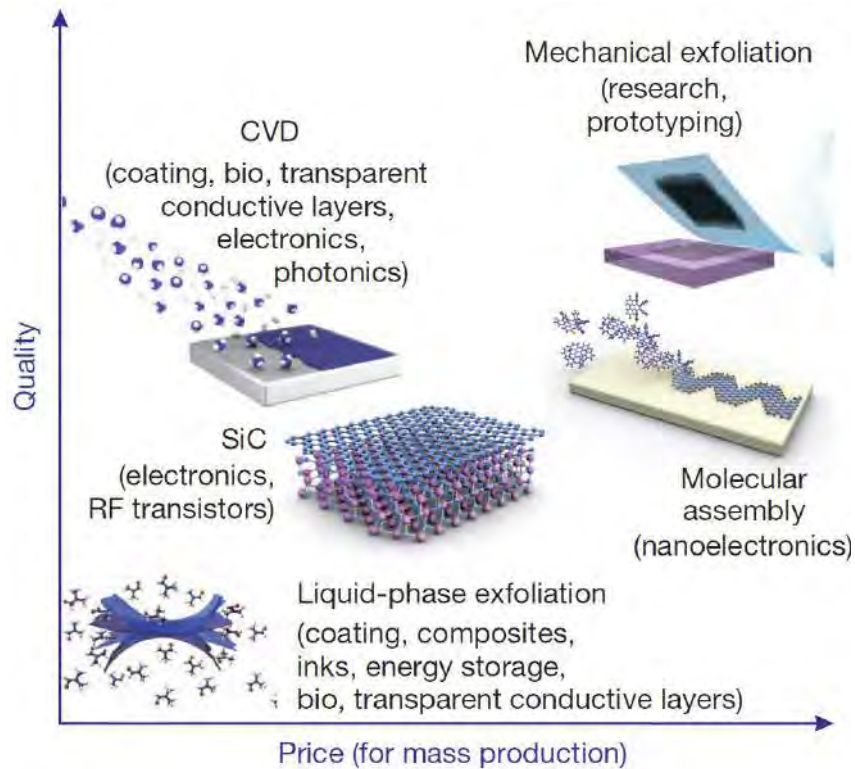
Figure 2.5: There are several methods of mass-production of graphene, which allow a wide choice in terms of size, quality and price for any particular application [70].

Table 2.3: Properties of graphene obtained by different methods. Modified from [70].

Method	Sample size (mm)	Charge carrier mobility (at ambient temperature) (cm^2/Vs)
Mechanical exfoliation	> 1	$> 2x10^5$ and $> 10^6$ (at low temperature)
Chemical exfoliation	Infinite as a layer of overlapping flakes	100 (for a layer of overlapping flakes)
Chemical exfoliation via graphene oxide	Infinite as a layer of overlapping flakes	1 (for a layer of overlapping flakes)
CVD	~ 1000	10,000
SiC	100	10,000

2.2 Graphene based biosensors

Biosensors can be simplified into two categories, label and non-label based. Label based technologies chemically modify a biological molecule with a fluorescent tag that can be seen

with a fluorescent microscope, however this method requires a lengthy labeling process and expensive detection equipment [71]. Label free technologies do not require any tagging to identify specific molecules and are ideal for quick and accurate diagnosis [72].

The use of nanostructures in electronic devices has allowed the development of biological and chemical sensors and is label-free [73, 74, 75]. Being the most studied alternative method observation of changes in the electrical, magnetic and optical device, information is obtained about the state of the device, from which one can elucidate the status of the analyte. Graphene biological sensors are examples of label free technologies that are currently under development [76].

2.2.1 Graphene biosensors

Nowadays, there have been several research works regarding the use of graphene for the detection of biomolecules. The understanding of the interaction between DNA and graphene is the key to the development of biological devices on substrates of conjugated carbon. The main interaction of DNA and graphene is based on stacking non-covalent π - π bonds that is shown in Figure 2.6 [77].

The stacking of nitrogenous bases leads to variation in the electrical response of DNA sensors [78] and is responsible for adsorption of the DNA nanostructure on graphene [79].

The recognition of the DNA immobilization on graphene is an important step in the development of biosensor. The bonding involves covalent and non-covalent processes. The first provides stability, but reduces the electronic properties desired for graphene. On the other hand, noncovalent immobilization maintains the structure of graphene with its electronic properties [80, 81]. It has been shown that the bond between graphene and nucleotides is dominated by non-covalent interactions [77, 82].

2.2.2 Graphene field effect transistors

Field effect transistor (FET) is a voltage controlled device which is capable of varying a current across a semiconducting channel by the application of an electric field. In a graphene field effect transistor (GFET)(see Figure 2.7) the graphene sheet acts as the semiconducting channel between two metal source and drain electrodes which lie atop an electrical insulator such as SiO_2. When charged biological molecules bind on the surface of the semiconducting graphene sheet in the GFET there is a measureable change in resistance [72].

Several investigations show the development in the use of GFET. Ohno et al. [7] successfully used a label free GFET device to detect bovine serum albumin, immunoglobulin E [76], and show that GFET has sensitivity under several hundred pico moles per liter [84]. Different sensors structures based on graphene with its corresponding analyte are shown in Table 2.4.
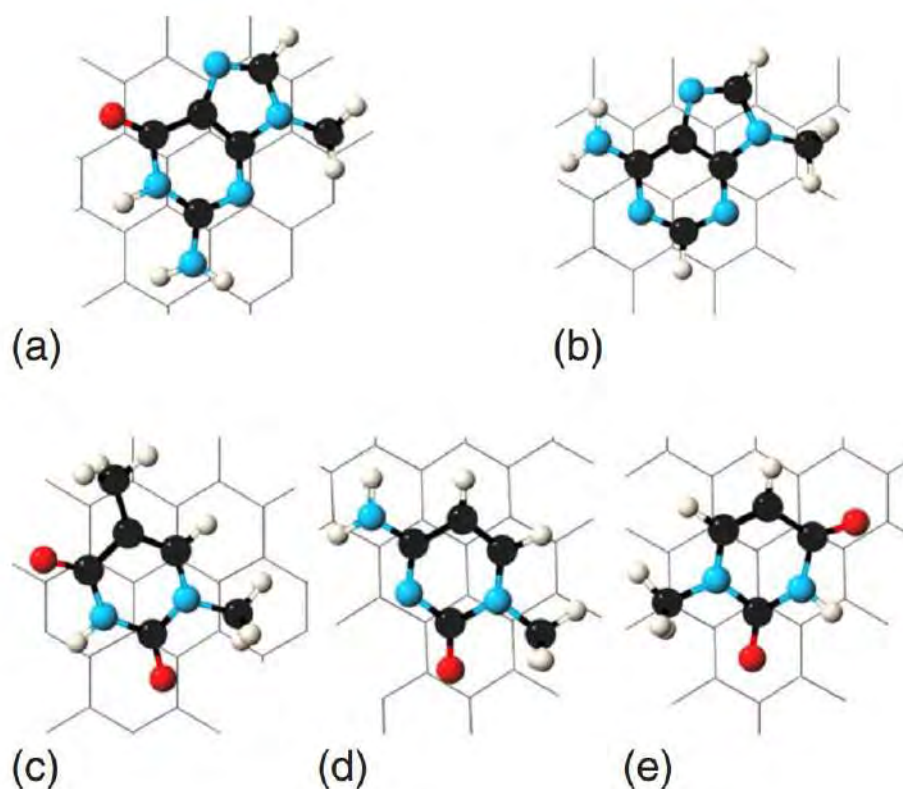
Figure 2.6: Equilibrium geometry of nucleobases on top of graphene based on density functional calculations: (a) guanine, (b) adenine, (c) thymine, (d) cytosine and (e) uracil [77].
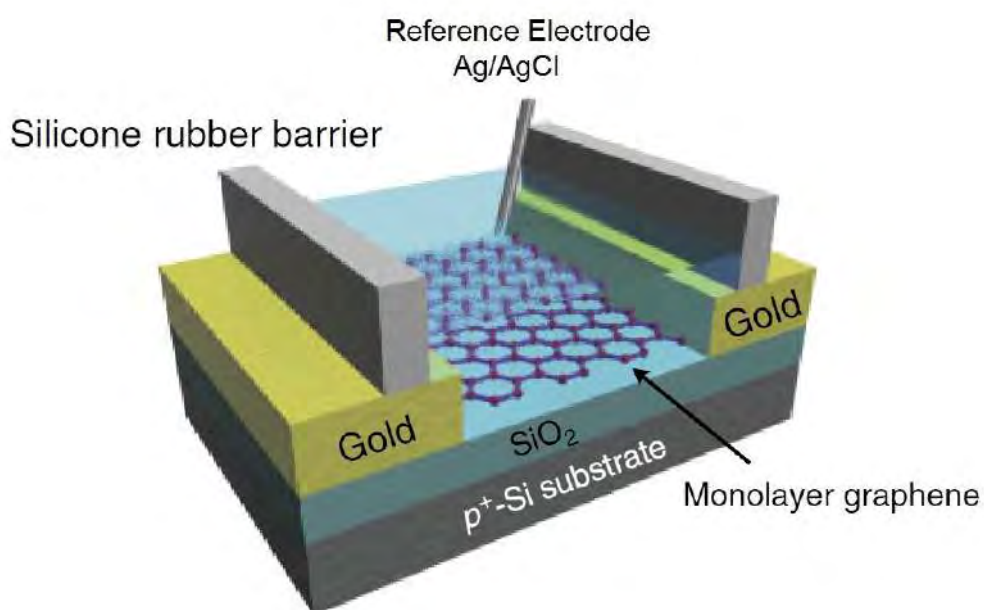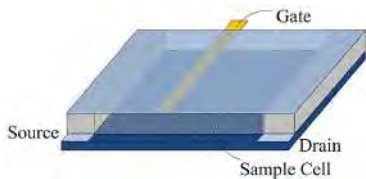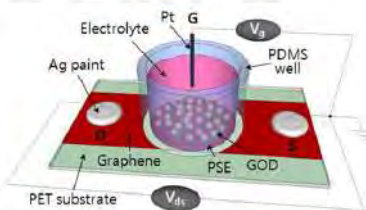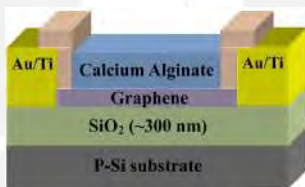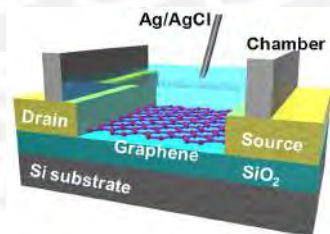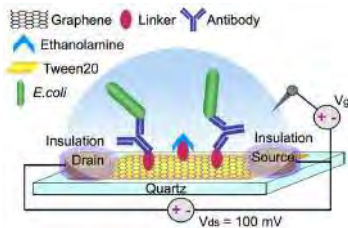
Figure 2.7: Schematic representation of a field effect transistor based on graphene[83].

Table 2.4: Different sensors structures based on graphene.

Structure (based on graphene)	Scheme	Analyte	Reference
Substrate: Glass Source and drain: indium tin oxide (ITO) Gate: Au Extraction electrodes with silver conductive paint Reservoir: PET		Adenosine triphosphate (ATP)	[10]
Substrate: PET Source and drain: Conductive silver paint Gate: Platinum wire Reservoir: PDMS		Glucose	[11]
Substrate: Si/SiO$_2$ Source and drain: Lithography Au/Ti Gate: Ag/AgCl Reservoir: Epoxy		Alanine aminotransferase	[85]
Substrate: Si/SiO$_2$ Source and drain: Ni/Au Gate: Ag/AgCl Cover: Silicone rubber		K or Na ions in a solution	[86]
Substrate: Quartz Source and drain: Silver conductive paint Gate: Ag/AgCl Silicone rubber to insulate the electrodes and form the recording chamber		E. coli bacteria	[87]

2.3 Characterization techniques

2.3.1 Analyzes of the structural and chemical properties

2.3.1.1 Raman Spectroscopy

Raman spectra are obtained by irradiating a sample with a powerful laser source of visible or infrared monochromatic radiation. During the process, the spectrum of radiation scattered at an angle, usually 90°, using a suitable spectrometer is recorded. To avoid fluorescence, wavelengths of excitation are removed from an absorption band of the analyte. The intensities of the Raman lines are at most 0.001% of the source intensity. This might seem more difficult to detect and measure the Raman vibrational bands in the infrared. However, the Raman radiation is diffused in the visible and near-infrared regions, for which there are already very sensitive detectors [88]. The Raman experiment is illustrated in Figure 2.8.
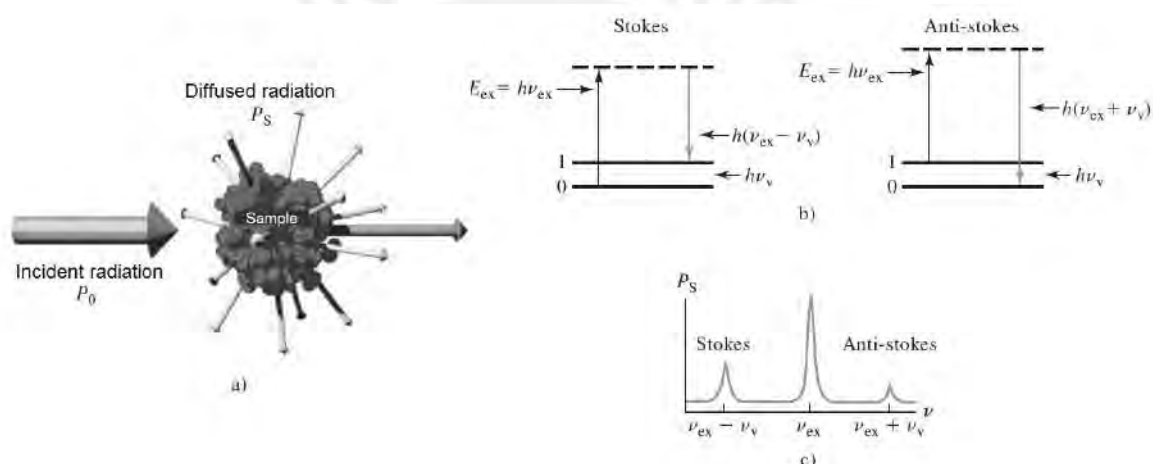
Figure 2.8: Origin of the Raman spectra [88].

In Figure 2.8, inelastic scattering in Raman spectroscopy occurs: a) When the frequency ν_{ex} incident radiation collides with the sample, the excited molecules of the sample move from one of its fundamental vibrational mode to a higher called virtual state, which is represented by the discontinuous level b). When the molecule relaxes, sometimes it returns to the first vibrational state, as noted, and emits a photon energy $E = h(\nu_{ex} - \nu_v)$ where ν_v is the frequency of the vibrational transition. Alternatively, if the molecule is in the first excited vibrational state, it could absorb a quantum of the incident radiation, be excited to virtual state and relax to the fundamental vibrational state. This process causes that a photon energy is emitted $E = h(\nu_{ex} + \nu_v)$. In both cases, the emitted radiation and incident radiation differ in the vibrational frequency of the molecule ν_v. c) The resulting spectrum of the diffused radiation in inelastically form shows three peaks, namely, one in $\nu_{ex} - \nu_v$ (Stokes), a second intense peak in ν_{ex} to the radiation diffused without frequency change and a third (anti-stokes) in $\nu_{ex} + \nu_v$. The intensities of the Stokes and antiStokes peaks

give quantitative information, and the position of the peaks provides qualitative data of the molecule in or on top of the sample [88].

2.3.1.2 Energy Dispersive X-ray Spectroscopy (EDS)

In a scanning electron microscope (SEM), the electron beam of high energy (1 to 30 keV) incident on the surface of a sample gives origin to different signals, one is x-ray photons. X-ray photons emerging from the specimen have energies specific to the elements in the specimen; these are the characteristics X-ray that provide the SEM with analytical capabilities. Other photons that have no relationships to the specimen elements constitute the continuum background of the spectrum. An example of the characteristic spectrum result is shown in Figure 2.9
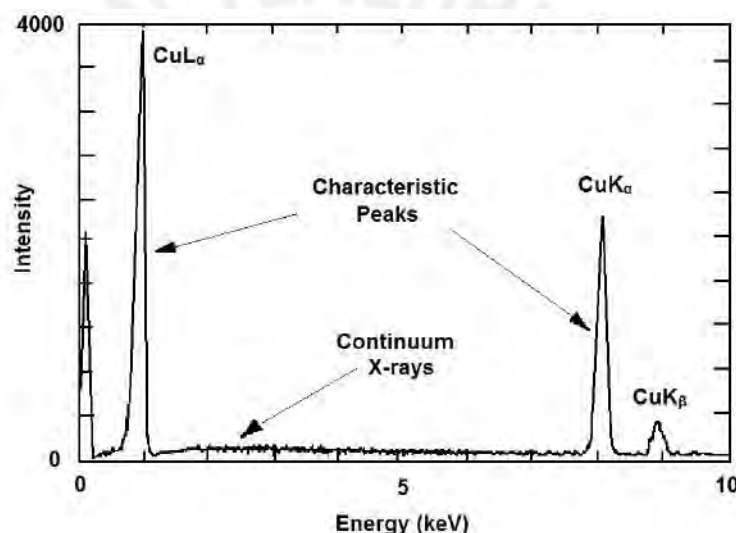
Figure 2.9: X-ray spectrum of copper showing K-series and L-series x-ray peaks and the continuous x-ray spectrum obtained with a Si(Li) EDS detector with an ultra-thin (diamond) x-ray window. Natural widths of peaks are much narrower than measured here. A noise peak is measured at very low energies. [89].

There are two processes of interaction between the sample and the electron beam that give rise to the emission of X-rays. One is originated from the fact that electrons to the beam are braking when they reach the sample surface. Part of the energy that electrons bring is emitted as electromagnetic radiation of very short wavelength (0.1 to 20 Å) in the range corresponding to radiation X. The total spectrum of energies corresponding to the X-rays emitted is called continuous spectrum. The amount of energy emitted by braking of the electron of the incident beam is not always the same and its maximum value corresponds to the condition of full braking, in which case it is equal to the energy of the incident beam (E_0).

The other process is originated from the electron energy of the incident beam that may be partially transferred to the atoms of the sample kicking out electrons of different orbitals. Electronic vacancies thus created are immediately filled by some electron of higher orbitals and the energy difference is emitted as X-rays. The energy of this X-rays is equal to the difference of the energies of the two levels concerned, and therefore has a characteristic value. By analysing the energy of the X-rays, called characteristic radiation, it is possible to identify the elements in the sample.

2.3.2 Analyzes of the morphological properties

2.3.2.1 Optical Microscopy

As seen in 3.1.1 graphene is considered an almost transparent material to the human eye. One could imagine then, that the optical microscopy may not be a suitable characterization technique. To overcome this problem, multi-reflection/interference effects can improve the contrast of the sample, this is realized through optical microscopy via the color contrast caused by the light interference effect at the SiO_2 substrate, which is modulated by the graphene layer [90, 91].

To obtain the mentioned effects, the incidence light passing from air onto a graphene sheet/SiO_2/Si tri-layer system should be considered, as shown in Figure 2.10. When a light front meets an interface, for example, the air/graphene or graphene/SiO_2 interface, a portion of the beam is reflected and the rest is transmitted, and thus, an infinite number of optical paths is possible [92].
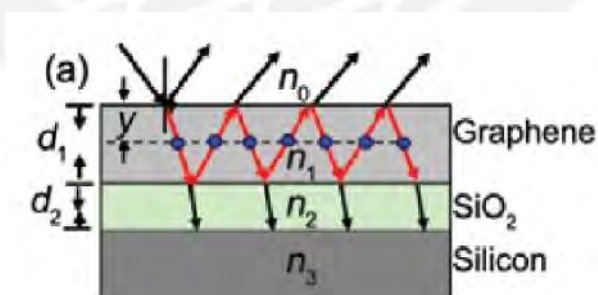
Figure 2.10: Schematic laser reflection and transmission at a certain depth y in graphene sheets deposited on a SiO_2/Si substrate. $n_0 = 1$ is the refractive index of air, $n_1 = 2.6 - 1.3i$, $n_2 = 1.46$, $n_3 = 4.15 - 0.044i$, are the refractive indices of graphite, SiO_2, and Si at 532 nm, respectively, $d1$ is the thickness of graphene which is estimated as $d_1 = N \triangle d$, where $\triangle d = 0.335$ nm is the thickness of single layer graphene and N is the number of layers, and d_2 is the thickness of SiO_2 and the Si substrate is considered as semi-infinite [92].

2.3.2.2 Confocal Laser Scanning Microscopy

The Confocal Laser Scanning Microscopy (CLSM) is a fluorescence-based imaging technique and offers a higher resolution than fluorescence microscopy due to its point illumination and detection properties [93]. The illumination in a confocal microscopy is achieved by a collimated laser beam across the specimen. This laser beam is reflected by a dichroic mirror and passes through the objective lens of the microscope in a focused manner on the specimen, which excites fluorescence probe in the sample. So, light is emitted at a longer wavelength which can come through the dichroic mirror and is again focused at the upper pinhole aperture (see Figure 2.11) [94]. With CLSM, out-of-focus light (coming from places of the specimen above or below the focus plane) is cut off before the beam hits the electronic detector due to the addition of a spatial filter containing an aperture, – the pinhole or slit – the point detection.

Just the in-focus light can pass through the pinhole (termed confocal aperture), reach the detector, and then form the image with more details because the blurring from out-of-focus has vanished. By using CLSM, it is possible to obtain high-resolution images from the samples, which increases the accuracy of the microscopic images [93, 95].
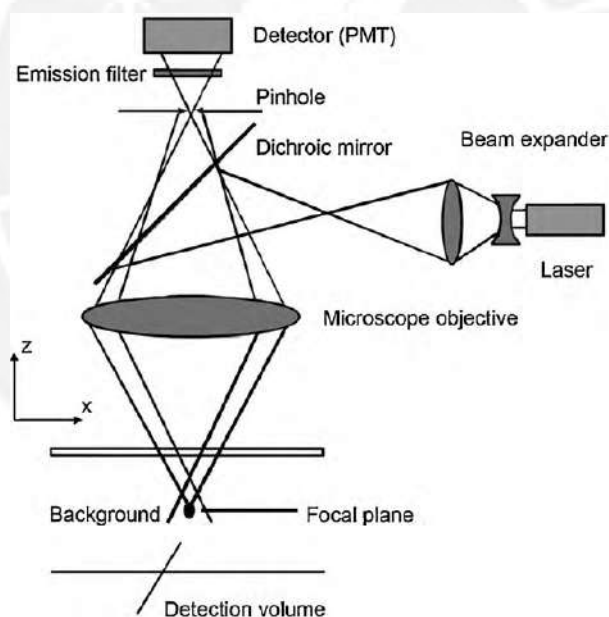
Figure 2.11: Schematic illustration of the CLSM [94].

2.3.2.3 Field Emission Scanning Electron Microscopy (FESEM)

The Scanning Electron Microscope (SEM) is an instrument that has been developed commercially from 1965 [96]. It was created from the work of Von Ardenne in 1938 and Zworykin in 1942 [97]. This instrument allows the observation and characterization of heterogeneous organic and inorganic materials on a nanometer (nm) to micrometer (μm) scale. SEM has

the capability of obtaining three-dimensional-like images of the surfaces of a very wide range of materials. The main use of this instrument is to obtain topographic images in the magnification range 10-10000x although it is possible to reach up to 1000000x [89].

The scanning electron microscope (SEM) uses a very thin and focused beam of high-energy electrons to generate an image and a variety of signals at the surface of solid specimens. The signals that derive from electron-sample interactions reveal information about the morphology of the surface, chemical composition, and crystalline structure and orientation of materials constituting the sample. The types of signals produced from the interaction of the electron beam with the sample include secondary electrons, backscattered electrons, characteristics x-rays, and other photons of various energies. These signals are obtained from specific emissions volumes within the sample (see Figure 2.12).
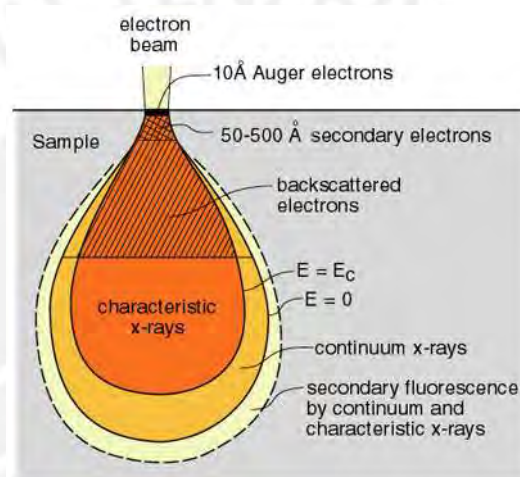
Figure 2.12: Different signals in the interaction volumen [98].

The imaging signals of greatest interest are the secondary and backscattered electrons because these vary primarily as a result of differences in surface topography. In secondary electron emission (emissive mode) the topographic contrast is the dominant and often masks the effects due to the variation in chemical composition of the sample, also is the most used for imaging in biology and the study of materials, given interest clear images and well-focused on those details that are not visible with other microscopes.

The backscattered electrons (reflective mode) are more efficient to detect variations in the chemical composition of the sample and can reveal details that are not visible in emissive mode. The reflective mode is widely used for flat surfaces (little topographic contrast).

Characteristic x-rays are also emitted as a result of electron bombardment. The analysis of the characteristic x-radiation emitted are used in EDS (see 3.3.1.2).

2.3.2.4 Atomic Force Microscopy (AFM)

AFM was first demonstrated in 1986 by Binnig, Quate and Gerber [99], to overcome the limitations in scanning tunnelling microscope (STM) that the substrate studied must be sufficiently conducting to support a tunnel current. This technique allows to see and measure surface structure with unprecedented resolution and accuracy.

An AFM is rather different from other microscopes, because it does not form an image by focusing light or electrons onto a surface, like an optical or electron microscope. An AFM physically "feels" the sample's surface with a sharp probe, building up a map of the height of the sample's surface.

Figure 2.13 shows a comparison between several types of microscopes and profilometers; the limitation of the AFM is that is not practical to make measurements on areas greater than about 100 μm. This is because as we said the AFM requires mechanically scanning the probe over a surface, and scanning such a large area would mean scanning very slowly.
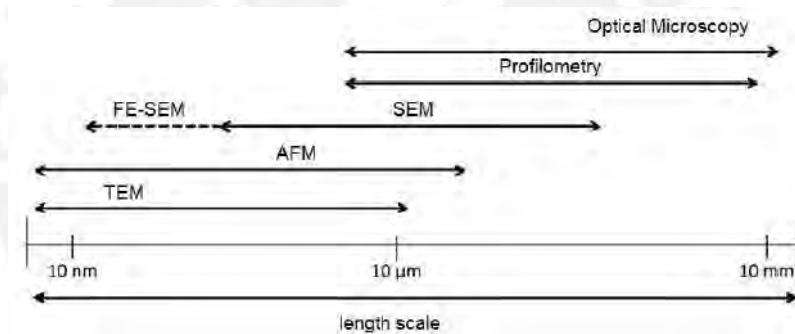
Figure 2.13: Comparison of length-scales of various microscopes [100].

Comparing AFM with a profilometer, the AFM has a greater x-y resolution because in the AFM the probe is sharper, the applied force in profilometer is around 10^{-6} N while in AFM is 10^{-9} N or less. Table 2.5 presents a comparison between AFM and SEM.

The operation of an AFM relies on the surface forces acting on a sharp tip that is usually supported on the end of a microcantilever whose minute deflections can be carefully monitored and it is in close proximity to a surface, these surface forces are ubiquitous and exist between tips of any material and substrates of any material. There are three main operation modes for an AFM: contact, non-contact and tapping. Contact mode was the first mode developed for AFM, a schematic representation of AFM and force regimes for operation modes are shown in Figure 2.14 .

Table 2.5: Comparison of AFM with SEM [100].

	AFM	SEM
Sample preparation	little or none	from little to a lot
Resolution	0.1 nm	5 nm
Relative cost	low	medium
Sample environment	any	vacuum (SEM) or gas (environmental SEM)
Depth of field	poor	good
Sample type	conductive or insulating	conductive
Time for image	2-5 minutes	0.1-1 minute
Maximum field of view	100 μm	1 mm
Maximum sample size	unlimited	30 mm
Measurements	3 dimensional	2 dimensional
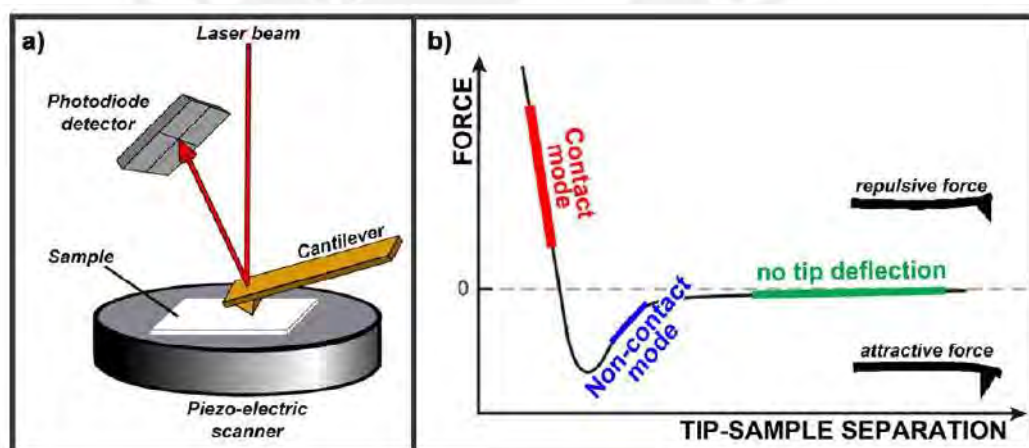
Figure 2.14: Atomic force microscopy. a) Schematic presentation of AFM; b) Force regimes governing AFM measurement [101].

2.4 Characterization of Graphene based biosensors

In this chapter, a summary of several investigations related to the characterization by different methods of graphene and biosensor base on graphene is presented. First, we will show investigations that produced and characterized bare graphene for use in different purposes. Some are shown below:

Z. H. Ni et al. [91] made an investigation about how to determinate the thickness of graphene using reflection and contrast spectroscopy. They discriminated the single-layer, bilayer, and multiple-layer graphene (<10 layers) on Si substrate with a 285 nm SiO_2 capping

layer by using contrast spectra, which were generated from the reflection light of a white light source. Figure 2.15 shows the optical image for different thickness of graphene and compared with Raman spectroscopy.
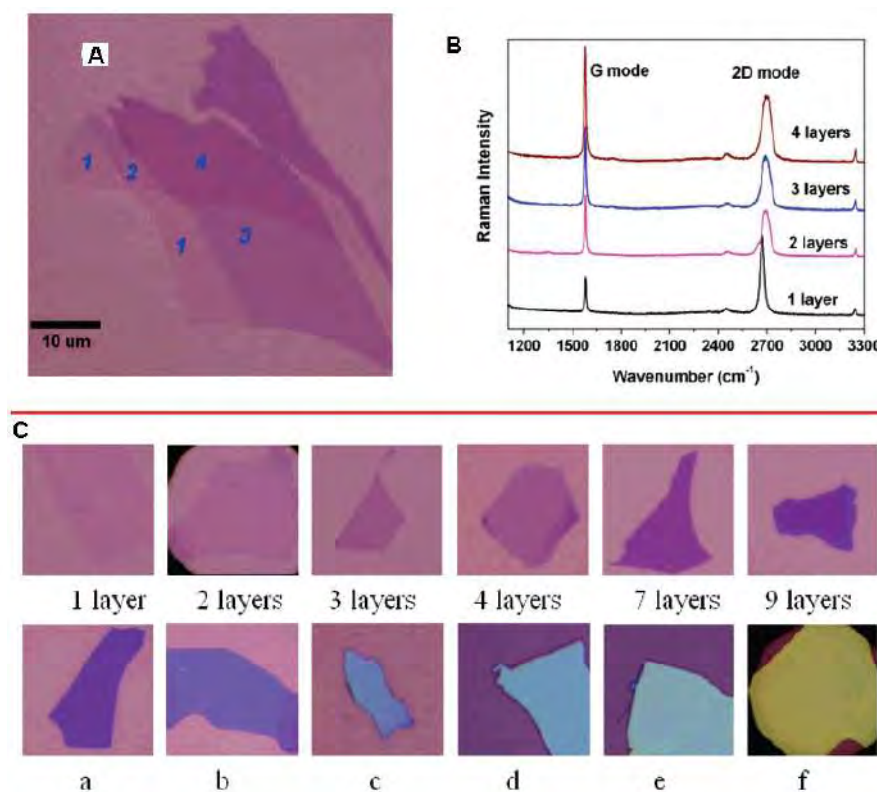
Figure 2.15: (A) Optical image of graphene with one, two, three, and four layers. (B) Raman spectra as a function of number of layers. (C) Optical image of different thickness. Besides the samples with one, two, three, four, seven, and nine layers, samples a, b, c, d, e, and f are more than 10 layers and the thickness increases from a to f [91].

Raman spectroscopy can provide a quick and effective way for structure and quality characterization of graphene. Carbon allotropes show their fingerprints under Raman spectroscopy mostly by D, G, and 2D peaks around 1350 cm^{-1}, 1580 cm^{-1} and 2700 cm^{-1}, respectively due to the change in electron bands.

The G peak or band is derived from the motion of two adjacent carbon atoms in the plane of a graphene lattice [102].This peak corresponds to the high-frequency E_{2g} phonon at the center of Brillouin zone, which corresponds to in-plane vibrations of sp^2 carbon atoms. The G band is observed both in graphene and in planar lattice vibrations in highly ordered pyrolytic graphite which exhibit an optical response at 1582 cm^{-1} [103]. Although the intensity increases with the number of graphene layers [104]. Comparison of Raman spectra between graphite, single and few layer graphene are shown in Figure 2.16.
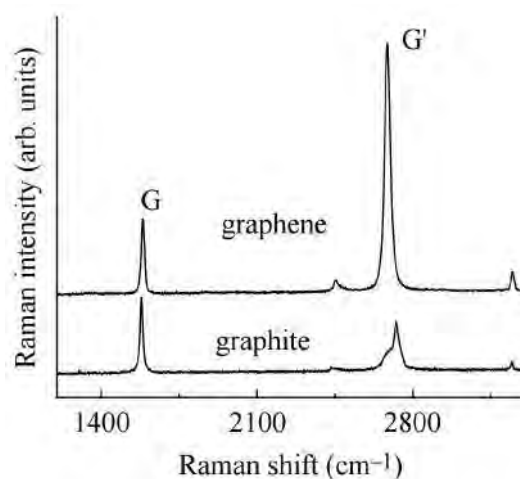
Figure 2.16: Comparison of Raman spectra at 514 nm for bulk graphite and graphene. [105].

The D band (located at $\sim 1350\ cm^{-1}$) originates from disorder in the sp^2-hybridized carbon atoms, characteristic for lattice distortions in the curved graphene sheets and/or tube ends . The D band typically contains defects and in the edges of a graphene flake. For these reason it is called the defective band and is usually used as a measure of the quality of the graphene flakes [104, 105].

Finally, the 2D or G´ band, at $\sim 2700\ cm^{-1}$, is the second order effect of the D band and it does not need the presence of defects or edges for its activation similar to the G band, the 2D band is present in all types of sp^2 carbon materials [103]. To this 2D band relies most of the graphene characterization because its shape and intensity strongly depend on the number of graphene layers [105].

The origin of the differences in the 2D band while increasing the number of layers is the appearance of multiple vibration modes when, in spite of having one monolayer of graphene, the measured sample has several layers. In multilayer graphene the D band is the result of the addition of two peaks and the 2D band results from the addition of four different peaks. The shape of the 2D band changes because of the relative intensity of these peaks varies depending on the number of the layers. Hence, graphene monolayer has a very narrow 2D band with intensity roughly four times greater than those of the G band whereas increasing the number of graphene layers makes that the 2D/G intensity ratio decrease and the 2D band becomes broader and upshifted [105].

Although these are the main peaks and they are reliable enough to characterize graphene, disorder induced Raman features can also appear as a second band typically labeled D' and occur around approximately $1620\ cm^{-1}$ [106]. D and D' bands have been observed on graphene lattices after inducing defects by the deposition of SiO$_2$ [107]. The 2D peak is the D

peak overtone, and the 2D' peak ($\sim 3248\ cm^{-1}$) is the D' overtone ($\sim 1620\ cm^{-1}$). Because the 2D and 2D' peaks originate from a process where momentum conservation is satisfied by two phonons with opposite wave vectors, no defects are required for their activation, and are thus always present [105, 108].

The band at $\sim 2450\ cm^{-1}$ in Figure 2.17 was first reported in graphite by Nemanich [109]. Its interpretation was subject to debate but it is assigned a combination of a D phonon and D" phonon peak and it is known as a weak defect-induced one phonon process and should be observed at $\sim 1100\ cm^{-1}$ [110], it is indicated as D + D" or also called G* peak [111].
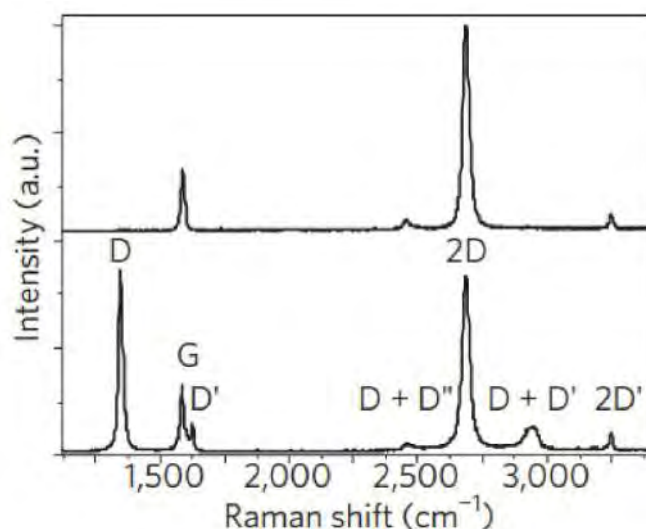
Figure 2.17: Raman spectra of pristine (top) and defected (bottom) graphene. The main peaks are labelled. [105].

Lee et al. [112] reported the characterization of structural features in CVD graphene by scanning electron microscopy (SEM). For the analysis of this investigation folding lines are invisible in a backscattering electron SEM image (Figure 2.18 (A)), they are clearly observed in secondary electron SEM images collected by the Everhart-Thornley Detector (ETD)and Through the Lens Detector (TLD) with a magnetic immersion lens, where they appear as lower brightness compared to the brightness of monolayer graphene regions. Shown in Figure 2.18 (B) and (C), folding lines appear with better contrast in the SEM images taken with TLD than those taken with ETD. Additionally to graphene folding lines, many dark spots (yellow circles in Figure 2.18 A–C) are also visible on the SEM images and these areas correspond to few-layer graphene. Also besides dark graphene folding lines, narrow bright lines were found in the transferred graphene on SiO$_2$ (Figure 2.18 E-F). As shown in 2.18 (A), these lines are wrinkles in graphene which were introduced during the transfer process.
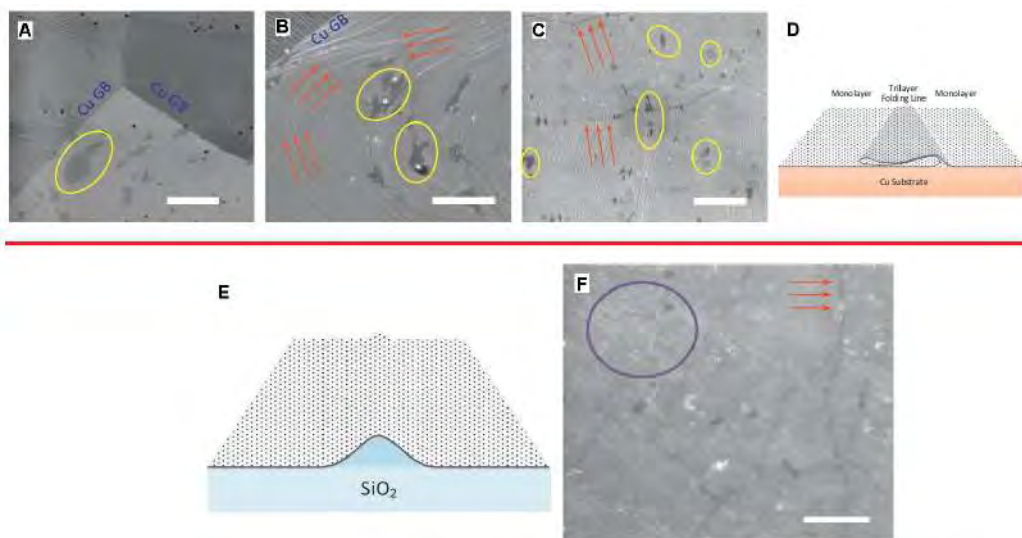
Figure 2.18: (A) 5 kV SEM images of graphene on Cu substrates with different detectors. High magnification SEM images using (A) backscattering detector (B) ETD, and (C) TLD. (D) A schematic illustration of a folding line. (E) An illustration of a graphene wrinkle. (F) 5 kV SEM images of transferred graphene on the SiO_2/Si substrate using a TLD. The red arrows indicate graphene folding lines, the yellow circles present multilayer graphene regimes, and each blue text of 'Cu GB' indicates a Cu grain boundary, the violet circle marks the region with many graphene wrinkles. Scale bars in (A)–(C), (F) are 5 μm [112].

Also, Giacchetti et al. [113] fabricated a single-layer graphene films that were grown by CVD and characterized by optical microscopy, atomic force microscopy (AFM) and Raman spectroscopy, showing excellent uniformity. Figure 2.19 presents the results of this process.

Characterization of biosensor base on graphene is more complicated and is related to the comparison with bare graphene and how the added molecules will behave interacting between the graphene and between each other, and also the characterization of the electrical characteristics. In this thesis we will emphasize the structural, chemical and morphological characterization. Some research results on this topic are shown below:

Wojcik et al. [72] fabricated and characterized a field effect transistor biosensor for the detection of thrombin protein. In the process of the fabrication they evaluated the effect of the annealing in CVD graphene by atomic force microscopy (AFM), the GFET was annealed at 400°C while flowing of 0.85 SLM Ar and 0.95 SLM H_2 for 1 hour. The intention of this annealing process was to improve the thrombin aptamer functionalization scheme by cleaning the surface of the graphene.
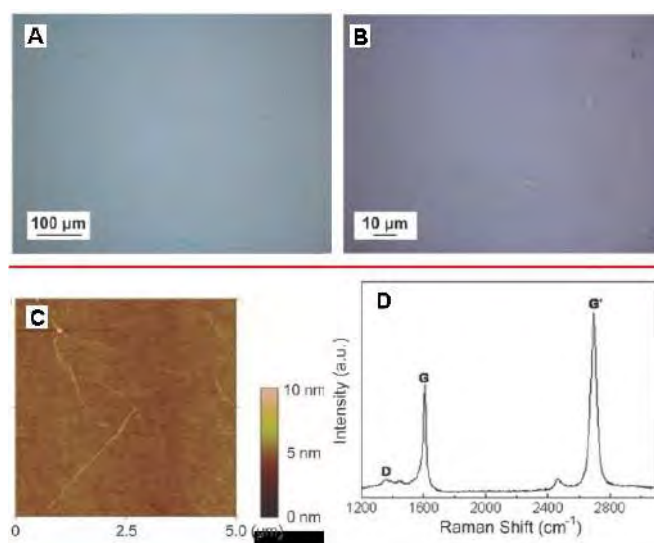
Figure 2.19: (A) and (B) optical micrograph of CVD-grown graphene on a silicon substrate. Single layer graphene with uniformity greater than 95% is obtained. (C) AFM image of the graphene shows excellent uniformity. (D) Raman spectrum confirms the presence of monolayer graphene [113]

The AFM analysis in Figure 2.20 of the graphene channel in the GFET device before the annealing shows that the average height of the graphene surface above the substrate is ∼2-3 nm. The corresponding height profile shows that there are large ∼1-4 nm structures on the graphene surface. The AFM analysis after annealing shows a drastic improvement in height characteristics. A height profile was taken at the approximate location of the height profile from the pre-annealing AFM image and shows that the average height of the graphene surface above the substrate after the anneal was reduced to ∼0.5 nm. Also, we can see that there was a thin coat of residue on the graphene surface before the anneal and that most of this residue was removed after the annealing.

For the functionalization of Thrombin Aptamer they used amine-reactive 1-pyrenebutanoic acid succinimidyl ester (PBASE) as the linker molecule between the graphene surface and thrombin aptamer. The PBASE non-covalently binds to the graphene surface via π-π stacking. After the addition of the PBASE comes the procedure of the addition of the thrombin aptamer which is an aptamer DNA oligonucleotide with the base sequence of 5'-/5Amino C6/GGT TGG TGT GGT TGG-3'. The oligonucleotide came synthesized with an amine group which reacts with the amine-reactive PBASE molecule. In Figure 2.21 an AFM image of the bare graphene channel before functionalization is shown. There are particles on the graphene sheet which are present in both the AFM analysis and height profile, however the average height of the graphene surface is ∼0.5 nm. After functionalization of the PBASE and thrombin aptamer the height profile of the graphene surface increased to ∼3 nm, suggesting that the thrombin aptamer was bound to the PBASE on the graphene surface [72].
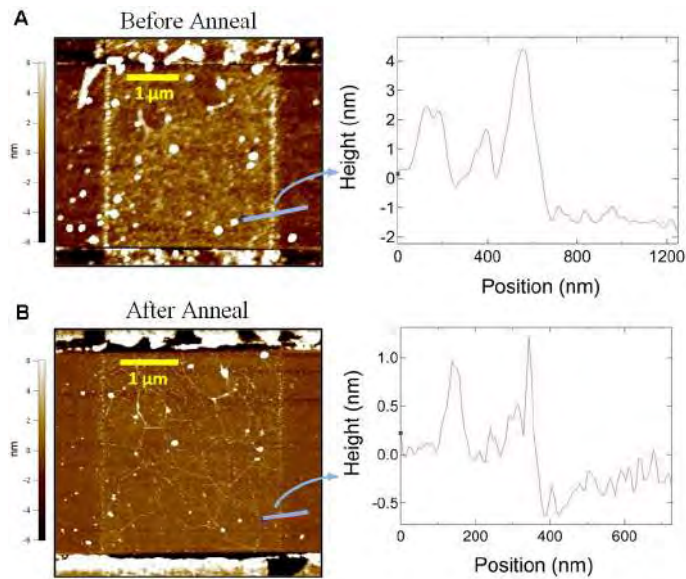
Figure 2.20: (A) AFM image of graphene channel in GFET before anneal and corresponding height profile marked by a blue line. (B) AFM image of graphene channel in GFET after anneal and corresponding height profile marked by a blue line. The electrodes are located at the top and bottom ∼0.5 μm portions of both AFM images. A color map of the height range is located at the left of each AFM image [72].
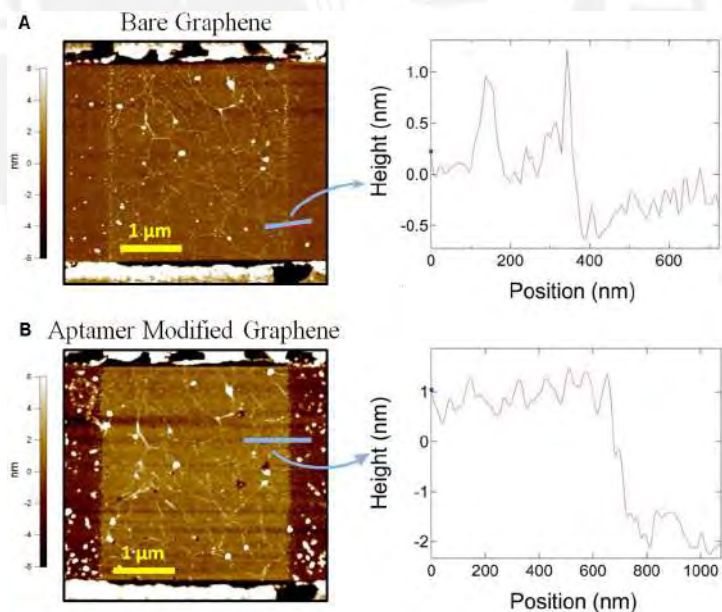
Figure 2.21: (A) AFM image of bare graphene channel in GFET and corresponding height profile marked by a blue line. (B) AFM image of aptamer modified graphene channel in GFET and corresponding height profile marked by a blue line. The electrodes are located at the top and bottom ∼0.5 μm portions of both AFM images. A color map of the height range is located at the left of each AFM image [72].

In another publication also made by Wojcik et al. [114] with the same biosensor, they show the interfase between the gold electrodes and the bare graphene, also with the presence of an aptamer over the surfaces, as shown in Figure 2.22.
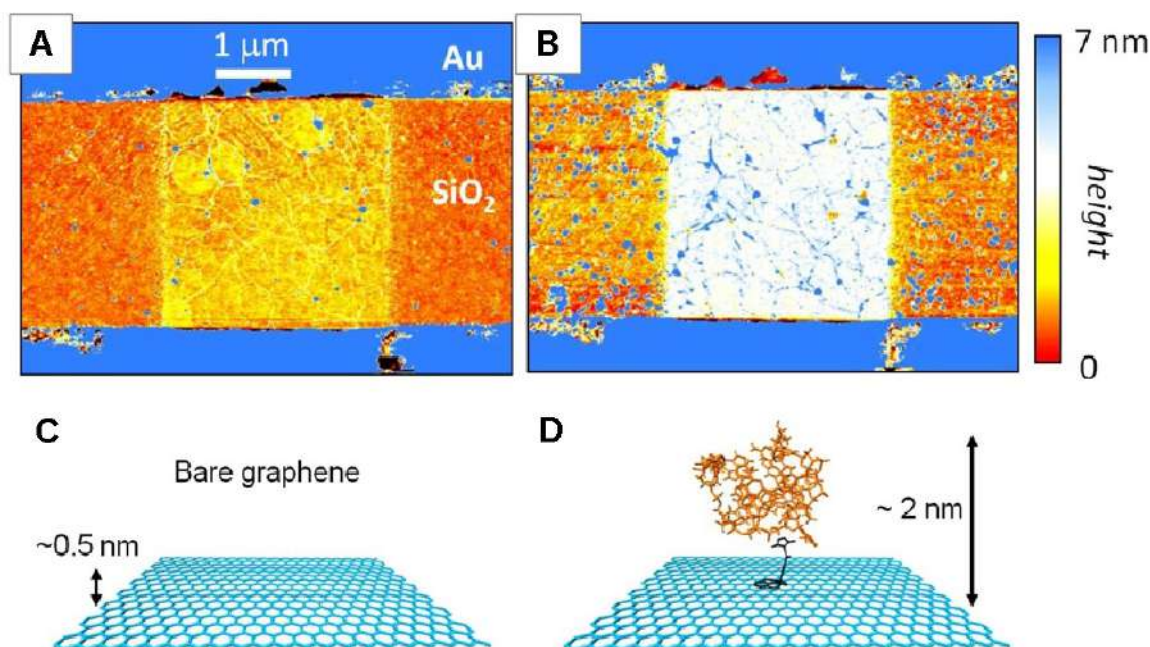
Figure 2.22: Functionalization of the graphene surface. (A) Atomic force microscopy image showing the bare graphene channel (3 x 3 μm²) on a SiO$_2$ substrate. A pair of gold electrodes are seen at the top and bottom of the image. The color scale represents surface height. The bare graphene surface is $\sim$0.5 nm above the substrate. (B) Atomic force microscopy image of the same device after treating the surface with PBASE and aptamer. The functionalized graphene surface is $\sim$2 nm above the substrate. (C) Illustration of the bare graphene surface, consistent with the first AFM image. (D) Illustration of the functionalized graphene surface showing the molecular structure of PBASE (black) and the molecular structure of the aptamer. The expected size of the PBASE–aptamer construct is consistent with the second AFM image [114].

Yeon Hwa Hwak et al. [115] fabricated a flexible glucose sensor using CVD-Grown graphene-based field effect transistor. The source and drain electrodes were prepared by using conductive silver paint and epoxy resin at the two opposite ends of the graphene film on the Polyethylene terephthalate (PET) substrate which made the device flexible. A custom designed polydimethylsiloxine (PDMS) well was attached on top of the graphene channel. The surface of graphene was functionalized with linker molecules (1-pyrenebutanoic acid succinimidyl ester (PBASE)) in order to immobilize the enzymes that induce the catalytic response of glucose. Then was functionalized with glucose oxidase (GOD).

A summary of their results are shown in Figure 2.23, to validate the graphene film the substrate was analyzed by Raman spectroscopy as shown in Figure 2.23 (A). According to the Raman spectroscopy results, G and 2D peaks were found at around 1585 and 2674 cm^{-1} respectively. The full-width-at-half-maximum (FWHM) of the 2D Raman peak was about 31 cm^{-1} and the intensity ratio of the 2D Raman peak to the G peak was about 2.65, representing the monolayer characteristics of the graphene film.

A characterization by AFM was performed in every step of the procedure (Figure 2.23 (C), where the averaged thickness of the graphene layer is ∼0.5 nm which does not deviate much from the original thickness of graphene ∼0.35 nm, reported in the literature.
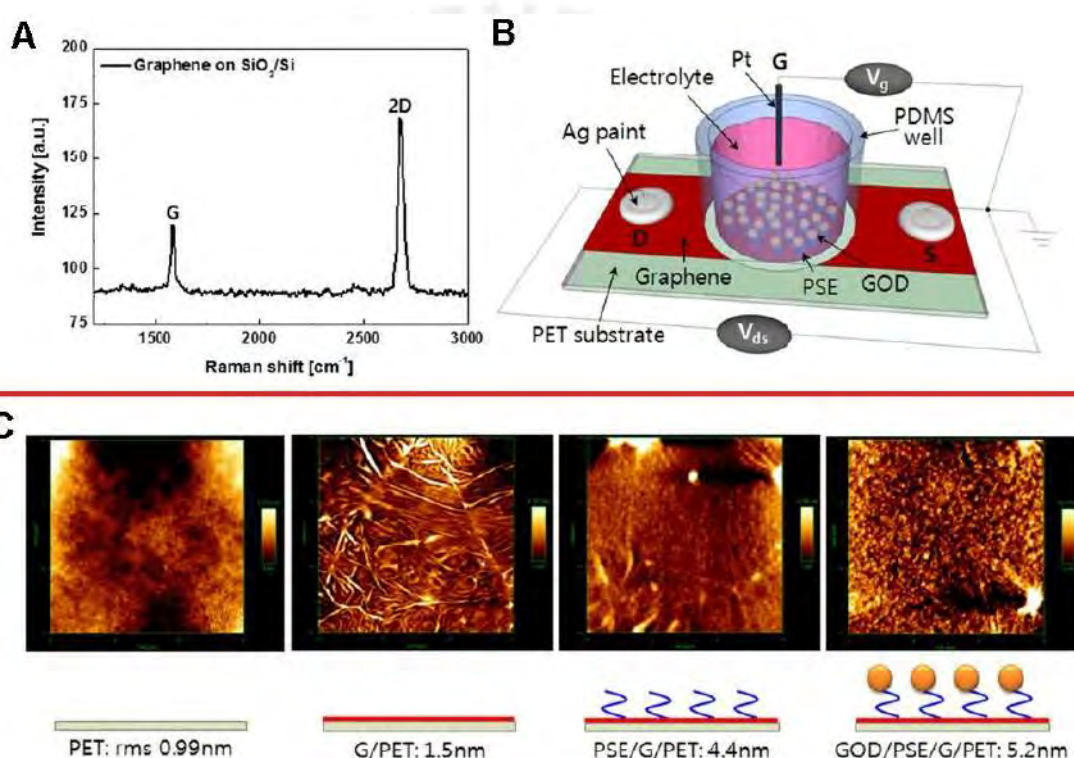
Figure 2.23: Fabricated CVD-grown graphene-based FET sensor; (A) Raman spectra of the monolayer graphene film on a SiO₂ deposited Si substrate, (B) experimental apparatus of the solution gated CVD graphene sensor, (C) AFM images for the surface modification procedures. The scanning area is 3 mm. [115].

Shi-Rui Guo et al. [116] fabricated a label-free DNA detector using large area CVD graphene-based field effect transistor. In Figure 2.24 (A) a schematic illustration of the graphene device where the contact electrodes were made of Ti/Au is presented. Then, to achieve the non-covalent functionalization they use 1-Pyrenebutanoic acid succinimidyl ester (PBASE) and a probe DNA sequence of (5'-3') Amine-AAC-TGC-CAG-CCT-ATG-TCC-AA, and a complementary DNA sequence of (5'-3') FAM-TTG-GAC-ATA-GGC-TGG-CAG-

TT (Figure 2.24 (B).

In Figure 2.24 (C-B) they show the characterization by AFM of the graphene before and after the probe DNA immobilization and also in Figure 2.24 (E-F) the images of graphene before and after photolithography. To characterize the graphene they use Raman spectroscopy, which results are shown in Figure 2.24 (C), where the difference between few-layer, bilayer and monolayer graphene can be observed.
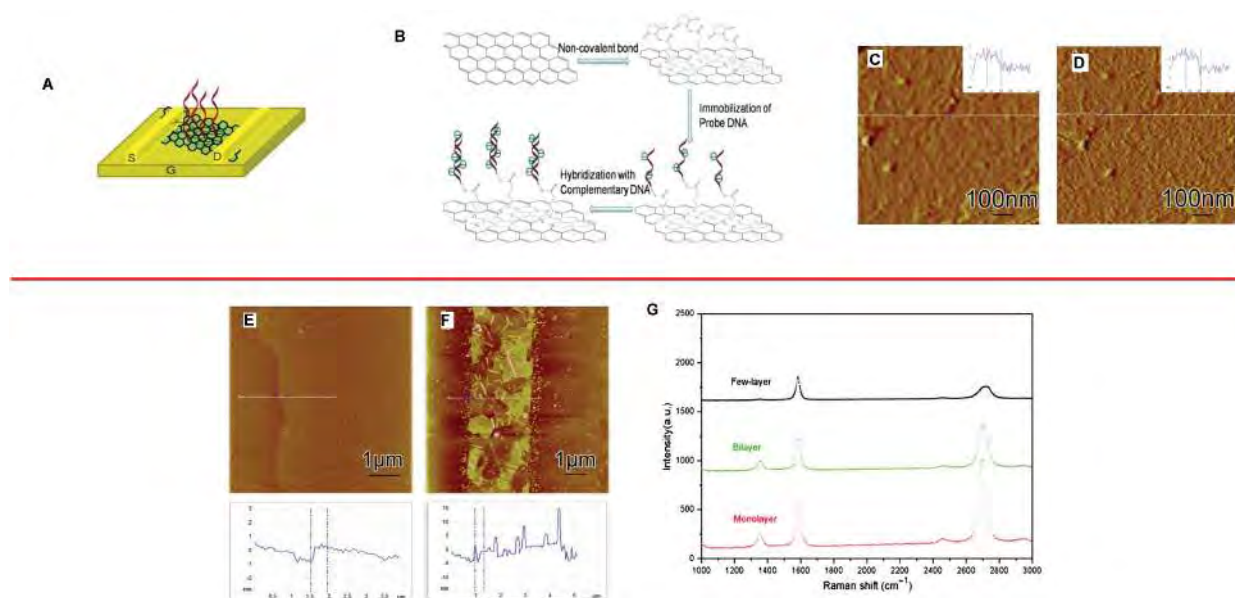
Figure 2.24: (A) Schematic illustration of graphene device; (B) Schematic illustration of the graphene sensor concept: modifying graphene with non-covalent bond and its binding of DNA strand. (C-D) AFM images of graphene before (C) and after (B) probe DNA immobilization. (E-F). AFM images of graphene before (E) and after (F) photolithography. (G) Raman spectra of the synthesized CVD graphene [116].

Tzu-Yin Chen et al. [54] fabricated a label-free electrical detector of DNA hybridization using a field effect transistor based on CVD grown graphene. The device fabrication involved the preparation of CVD graphene, transference on a SiO_2 substrate, the placement of the silver paint as a source and drain electrodes and the creation of a silicone rubber reservoir. Single-stranded DNA molecules with these sequences: 5'–AGG TCGCCGCCC-3' (as probe) and 3'–TCC AGCGGCGGG-5' (as complement "target") dissolved in phosphate buffered saline (PBS) were tested.

Figure 2.25 presents a summary of the results of their investigation, Figure 2.25 (A-C) shows the difference that produce the annealing in the graphene, characterized by Raman spectroscopy and in transfer curves. The Raman spectrum for as-transferred sample exhibits features of high-quality single-layer graphene: a symmetric 2D band ($\approx 2700\ cm^{-1}$) with

a full width at half maximum of 30.2 cm^{-1} and a high I_{2D}/I_G ratio (1.95). After thermal cleaning in H_2/Ar environment (20/80 sccm) at 450°C, a shift in G band (from 1588.6 to 1592.0 cm^{-1}) and 2D band (from 2701.9 to 2716.9 cm^{-1}) occurs.

They also analyzed the effect of graphene surface condition to the DNA sensing performance by differentiating the used PMMA layer (as a graphene transfer supporting layer) and replaced by a layer of Au film. The Raman spectra in Figure 2.25 (D) shows that both gold-transferred graphene and annealed PMMA-graphene exhibit a G-band at 1595.7 and 1591.7 cm^{-1} in addition to 2D-band at 2719.8 and 2720.3 cm^{-1} correspondingly. The I_{2D}/I_G ratio of the gold-transferred sample (1.81) is comparable to that (1.58) of the annealed PMMA one, this suggests that the graphene transferred by PMMA and Au are comparable in film quality. The AMF image shows in Figure 2.25 (D-F) that the graphene layer is still covered with some PMMA residues even after annealing. In clear contrast, the surface of the gold-transferred graphene is relatively much cleaner, as demonstrated in Figure 2.25 (D).
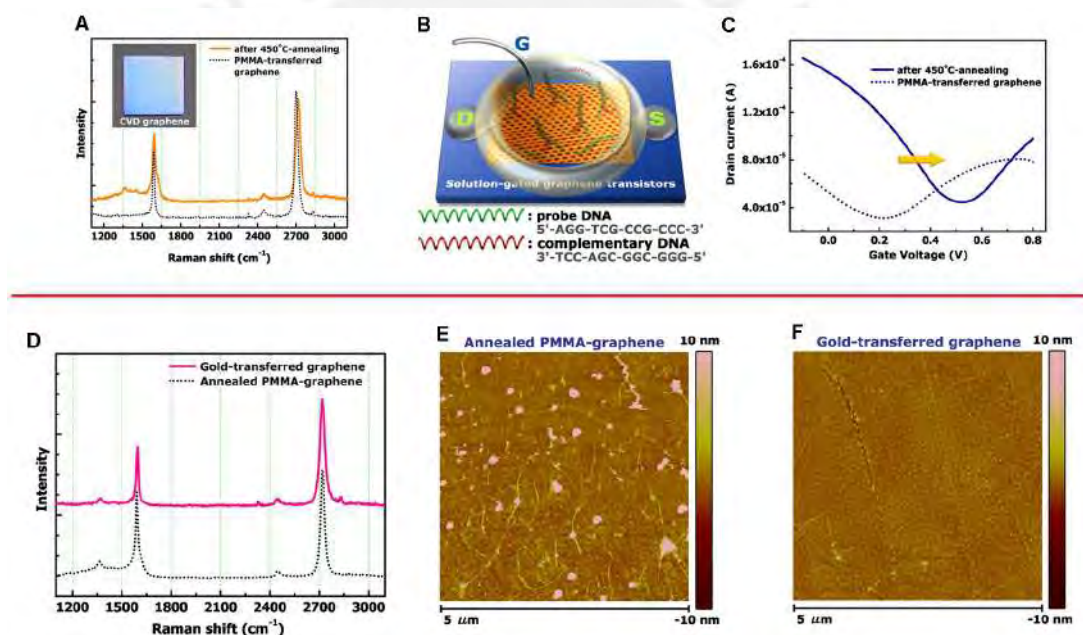
Figure 2.25: (A) Raman spectra of single-layer CVD graphene before and after thermal cleaning. The inset shows a graphene sheet set on a silicon substrate. (B) Schematic illustration of a graphene FET in liquid-gated configuration. (C) Transfer curves of a liquid-gated graphene FET before and after annealing. (D) Raman spectra of graphene sheets prepared by gold-transfer and PMMA-transfer methods, respectively. (E) (F) AFM images of PMMA- and gold-transferred graphene. Note that annealing was performed for the PMMA-transferred sample. [54].

Yinxi Huang et al. [87] fabricated CVD graphene-based biosensors for electrically detection of E. coli bacteria. The fabrication of the graphene device involves the placement of the electrodes (source and drain) made by silver conductive paint and the insulate of the elec-

trodes with silicone rubber. A linker molecule (1-pyrenebutanoic acid succinimidyl ester) was used for the immobilization of the DNA and then functionalized with anti-E. coli antibodies. Additionally of this process they used ethanolamine to quench the unreacted succinimidyl ester group on linker molecules and followed by Tween 20 to passivate uncoated graphene area.

Figure 2.26 (A-B) shows the results of the characterization of the CVD graphene by Raman spectroscopy and AFM, the Raman spectrum taken at a darker spot (indicated by a circle in the Raman map) exhibits the characteristic spectrum of single-layered graphene with a sharp 2D peak and a ratio between 2D and G band (I_{2D}/I_G) of $\sim$4.0 (solid trace in Figure 2.26 (A)). In contrast, the spectrum in a brighter spot (indicated by a square) exhibits an attenuated 2D band and a low I_{2D}/I_G ($\sim$0.5), indicating its few-layered structure (dotted trace). As observed, the graphene film is continuous, uniform, and dominantly single-layered while some wrinkles are observed in the AFM analysis. Additionally Figure 2.26 (C) shows an illustration of the E. coli attached onto the antibody functionalized graphene film and Figure 2.26 (D) presents the CVD-grown graphene exhibiting the characteristic ambipolar field-effect-behavior and how each functionalization step led to a shift in the transfer curve (drain-source current I_{ds} versus the solution-gate voltage V_g).

Finally, Jin Heak Jung et al. [117] attempted to elucidate the importance of graphene surface quality for their use as a FET biosensor by comparing two types of CVD graphene transfer using polymer-mediated transfer and Au mediated transfer. The procedure of the transfer of graphene can be seen in reference [117]. The fabrication of their sensor to detect a protein biomarker for cancer (carbohydrate antigen 19-9 (CA 19-9)) involved the development of CVD graphene transferred to SiO_2 substrate, and the use of chromium/Au layers as source and drain electrodes, the adition of a PDMS well attached to the graphene channels for the sensing experiments, the use of 1-pyrenebutanoic acid succinimidyl ester (PBASE) as a linker molecule and the antibodies (Ab) probes.

The surfaces of the graphene samples transferred by the PMMA and Au transfer methods were investigated by AFM, for the graphene transferred using a PMMA layer, polymer residues could be clearly observed while no polymer residues were observed on the graphene transferred using the Au layer method (Figure 2.27 (A-B)). The root-mean squared (RMS) surface roughnesses of the graphene surfaces from the AFM analysis were 4.2 and 1.2 nm for the graphene transferred by the PMMA and Au methods, respectively. The AFM results indicated that a smoother and cleaner graphene surface free of polymer residue was obtained by the Au transfer method. Also Raman spectroscopy was performed for the comparison, lower signal to-noise ratio and intensity of G and 2D peaks as well as absence of low-frequency background (1100–1600 cm^{-1}) in the Raman spectra from Au-transferred graphene compared to those of PMMA-transferred graphene (Figure 2.27 (C-E)) confirm the surface cleanness of Au-transferred graphene.
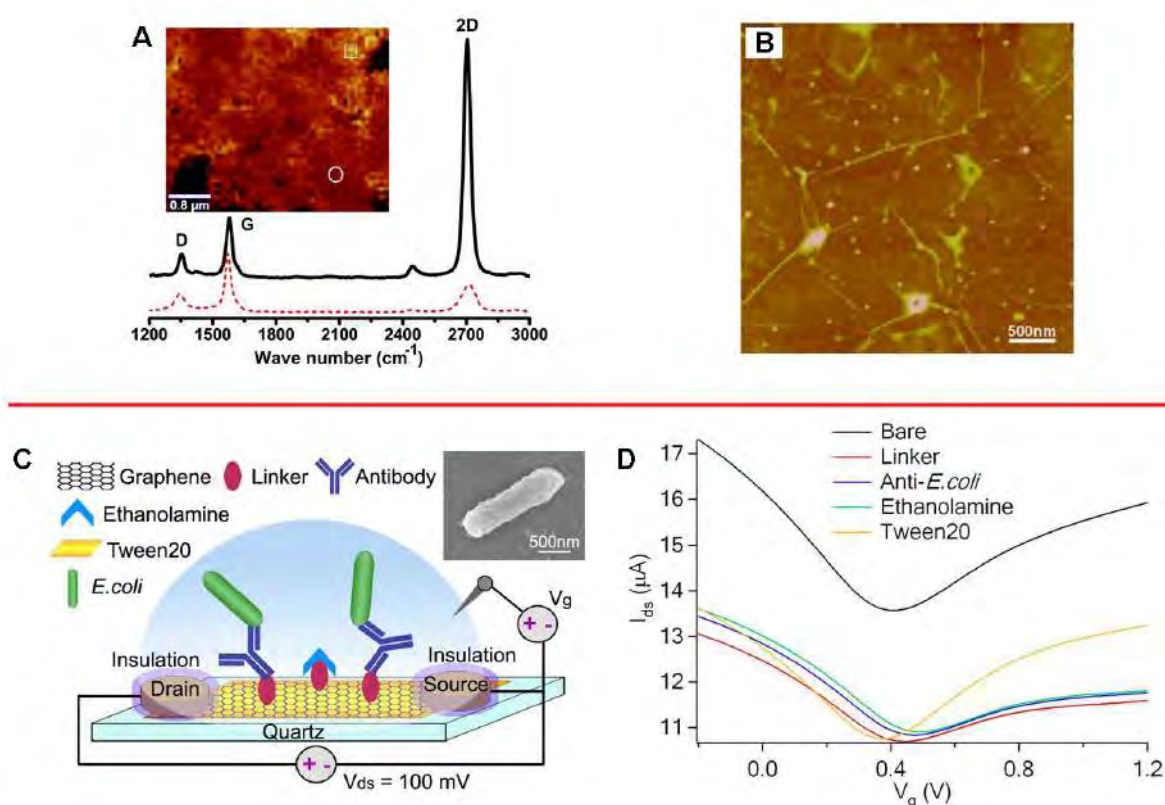
Figure 2.26: (A) Raman map and spectrum of graphene film. The map is constructed by plotting the peak width at half height of the 2D-band as the pixel intensity. Scale bar = 0.8 mm. (B) AFM image of the graphene film. Scale bar = 500 nm. (C) Illustration of anti-E. coli antibody functionalized graphene- FET for detection of E. coli. Inset: Scanning electron microscopy (SEM) image of an E. coli on antibody functionalized graphene. (D) Transfer curves of a graphene FET before functionalization and after functionalizing sequentially with linker molecules, anti-E. coli antibodies, ethanolamine and Tween 20. $V_{ds} = 100$ mV [87].

Figure 2.28 (A) shows an illustration of the antibody successfully attached on linker-functionalized graphene channels. A characterization by AFM was performed after the immobilization of antibodies probes with the linker for both types of sensors. In Figure 2.28 (B) weakly bright areas indicate Ab probe molecules, wherein the surface roughness of PMMA-transferred graphene with Ab probes ($\sim$2.2 nm) decreased from that of the PMMA-transferred graphene FET with no Ab probes ($\sim$4.2 nm), Thus, as shown in Figure 2.28 (C)), the surface roughness of the Au-transferred graphene with Ab probes increased from $\sim$1.2 for the Au-transferred graphene FET with no Ab probes to $\sim$2.8 nm.
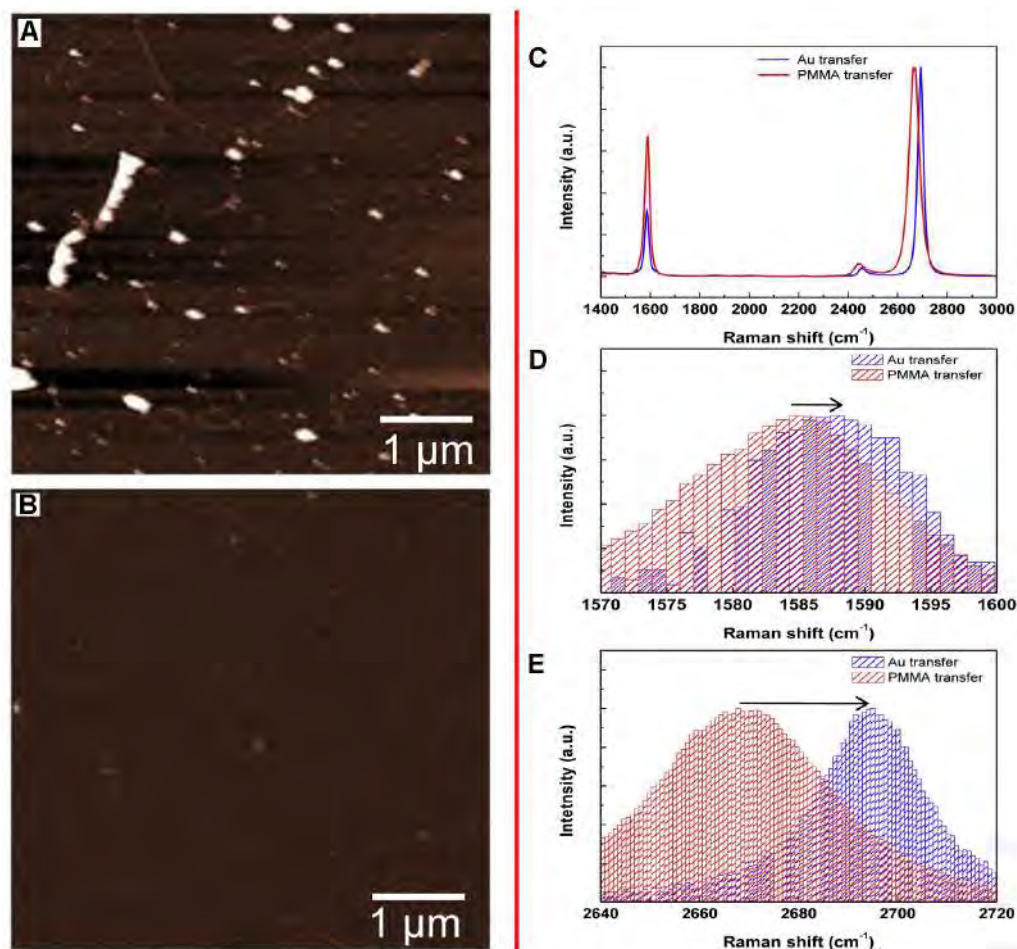
Figure 2.27: (A) AFM image of the graphene surface after removal of the PMMA layer using acetone (RMS surface roughness = ~4.2 nm). (B) AFM image of the graphene surface after removal of the Au layer by a KI/I$_2$ solution (RMS surface roughness = ~1.2 nm). (C) Raman spectra of graphene transferred by two different methods, (D) histogram distributions of variation in the G band positions, and (E) histogram distributions of variations in the 2D band [117].

The result in the transfer characteristics indicated changes of I$_D$ and V$_{DP}$ with surface modification. With the attachment of Ab probe molecules, V$_{DP}$ did not shift significantly; however, the hole current increased slightly. Also the Raman spectra after functionalization by linker molecules, shows that the G and 2D bands decreased from 1584.82 and 2694.97 to 1583.78 and 2669.45 cm^{-1}, respectively [117].
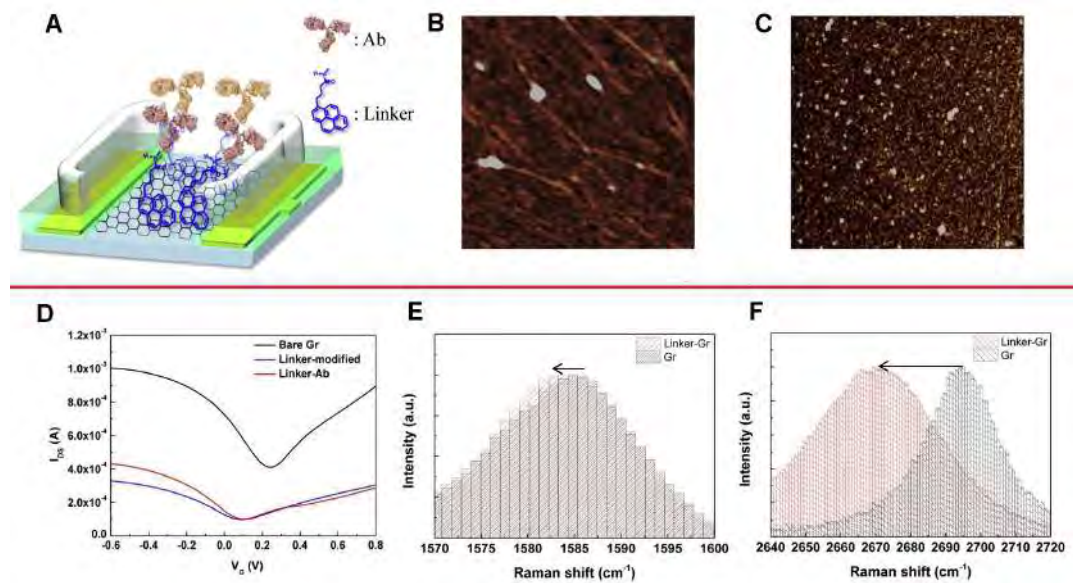
Figure 2.28: (A) Illustration of Ab functionalized graphene FET for CA 19-9 detection, (B) AFM images of graphene after immobilization of Ab probes with PBASE as a linker molecule on PMMA-transferred graphene (RMS surface roughness (∼4.2 nm), (C) AFM image after immobilization of Ab with the linker on Au-transferred graphene (RMS surface roughness ∼2.8 nm), (d) transfer characteristics of graphene FET with no modification (bare graphene channel), after modification by linker and after Ab functionalization obtained at $V_{DS} = 100$ mV. The variations in the Raman spectra were measured after removal of solution; (E) G band position and (F) 2D band. [117].

2.5 Tuberculosis: diagnosis and problematic

Tuberculosis (TB) is an infectious bacterial disease caused by the bacillus Mycobacterium tuberculosis, also known as Koch's bacillus. Mainly it affects the lungs (pulmonary TB) but can affect other organs or tissues (extrapulmonary TB) as skin, bones, kidneys and brain [3]. TB can occur in any organ; since the bacillus spreads throughout the body and can be set anywhere in the body. But nevertheless; usually between 80% and 85% of cases, TB manifests as lung disease, because the bacillus needs plenty of oxygen to multiply [118].

The tuberculosis bacillus spreads through the air when infected people expel the bacteria by coughing, sneezing, talking or spitting. Infection occurs when the bacteria that can remain airborne for several hours until inhaled. After infection the bacteria multiply slowly, after one to two months the first injuries occur, it is at that moment in which the immune system is activated to fight the bacteria. In 90% of cases the situation is stabilized and tuberculosis can be kept inactive or dormant for several years, in this state the infected person has no symptoms and cannot spread the disease. On the other hand, if the immune system fails to control the infection, it is derived active tuberculosis [119].

In 1993, the World Health Organization (WHO) declared tuberculosis as a global public health emergency. At that time they were presented about 7 to 8 million cases and 1.3 to 1.6 million deaths per year due to this disease. In 2011 approximately 9 million new cases and 1.4 million deaths were estimated. Tuberculosis is considered the second leading cause of death from an infectious disease worldwide and it is estimated that one third of the world population is infected.

In 2013, there were an estimated 9.0 million incident cases of TB (range, 8.6 million − 9.4 million) globally, equivalent to 126 cases per 100 000 population. The absolute number of incident cases is falling slowly (Figure 2.29), at an average rate of 1.5% per year 2000 − 2013 and 0.6% between 2012 and 2013 [3].
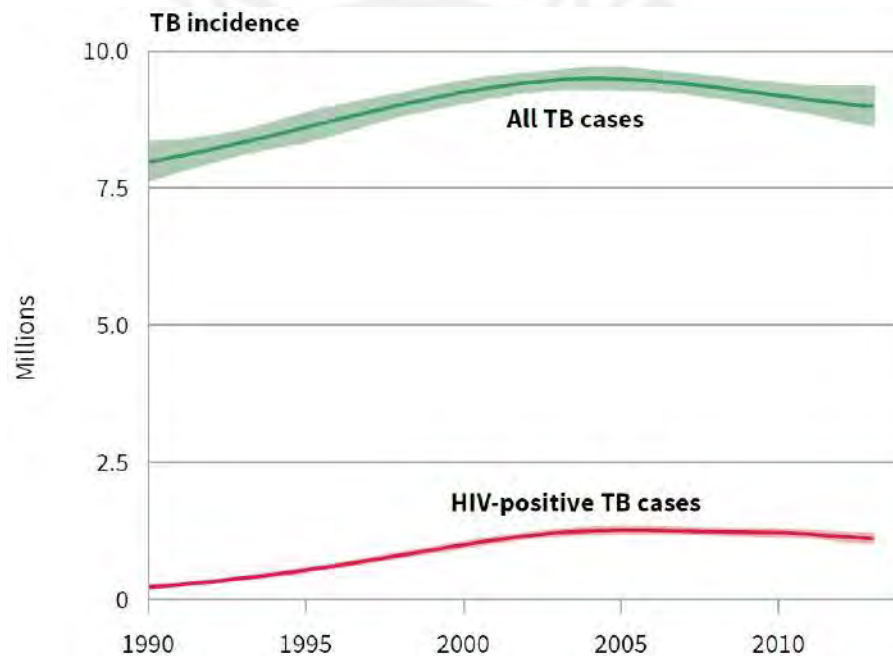
Figure 2.29: Estimated absolute numbers of TB cases and deaths (in millions per year), 1990–2013 [3].

In Peru, for 2010, 32.477 cases of tuberculosis were diagnosed in all its forms, most concentrated in Lima, of which 28.297 were new, corresponding to them about 17,264 were cases of pulmonary tuberculosis with positive bacilloscopy. It was estimated that in Peru in 2012, between 30% and 40% of the population were infected with the TB bacteria (not all developed the disease). Of this percentage the largest ratio would be among health workers and public transport workers. In both cases, transmission is performed by the conditions of their occupation, so one can think of TB as an occupational disease [120].

During the last decades the Ministry of Health of Peru has implemented one of the best strategies for prevention and control of tuberculosis, recognized and awarded internationally by the WHO, by conducting training workshops for control and prevention, and also has recently published a new law in 2016 for the rights and responsibilities of people with tuberculosis [121]. All this effort has reduced significantly the incidence rate and mortality due to tuberculosis in Peru; however, despite the efforts made by the Ministry of Health, Peru still has one of the highest rates of incidence and mortality of America.

Farga and Caminero [122] indicate that the increase of tuberculosis worldwide is because of the following reasons:

- Increased risk populations in crowded urban areas

- Pandemic infection of HIV / AIDS in both urban and rural areas

- Increased poverty in Peru

- Migration from the countryside to the city and the return of people affected by TB to their communities.

- Neglect of TB programs in Peru

- Multi-resistant tuberculosis in Peru

Different techniques exist to diagnose TB, the most common used in Peru are:

- Examination of sputum or bacilloscopy: The main way to diagnose TB. It involves taking samples of sputum in order to observe bacillus that cause the disease through a microscope. These samples must be deposited in plastic disposable containers, totally clean, dry and wide-mouth screw cap.

- Cultivation of sputum: It is a more sensitive test that bacilloscopy to give the diagnosis, the result is given after 8 weeks. It is indicated for people with suspected TB but whose bacilloscopy was negative, or is also used for monitoring.

- Chest x-ray test: Is an essential and very useful in the diagnosis of TB, can see the extent of lung disease, its evolution and its aftermath.

Of these techniques, one of the most used is the examination of sputum or bacilloscopy for being effective, simple, inexpensive and relatively quick; besides being recommended by WHO is the staining Ziehl Neelsen method. This technique is based on staining acid-fast bacillus (AFB) of the sputum samples of patients following the principle of acid-fast, when the smear is stained with carbol fuchsin, it solubilizes the lipoidal material present in the Mycobacterial cell wall but by the application of heat, carbol fuchsin further penetrates

through lipoidal wall and enters into cytoplasm. Then after all cell appears red. Then the smear is decolorized with decolorizing agent (3% HCL in 95% alcohol) but the acid fast cells are resistant due to the presence of large amount of lipoidal material in their cell wall which prevents the penetration of decolorizing solution. The non-acid fast organism lack the lipoidal material in their cell wall due to which they are easily decolorized, leaving the cells colorless. Then the smear is stained with counterstain, methylene blue. Only decolorized cells absorb the counter stain and take its color and appears blue while acid-fast cells retain the red color. This identifies the TB bacillus as a fuchsia red swab on a color background for easy viewing (see Figure 2.30) [118]. This process incurs a series of procedures if the person in charge has no special care may suffer contagion so the staff must have good training and care in the use of the technique [123].

Figure 2.30: Visualization of Mycobacterium tuberculosis using the Ziehl-Neelsen method [118].

Recent advances in methodologies based on the polymerase chain reaction (PCR) to detect the gene of tuberculosis, such as quantitative PCR, probe assays line, or nucleic acid amplification tests (NAATs), make it possible to create new rapid diagnostic tests [5, 124]; although these diagnostic methods require sophisticated laboratory facilities and highly qualified staff, which implies a high cost in implementation.

With this background the use of nanomaterials is a good alternative to develop new rapid and low-cost methods to diagnose and identify Mycobacterium tuberculosis bacillus with good sensitivity and specificity.

3 Experimental procedure

In this chapter, the experimental procedure is explained in detail. First, the fabrication of the sensing elements is described step by step and also the materials used are presented. Then, the procedures and the experimental parameters used in the characterization techniques such as Raman Spectroscopy, Energy Dispersive X-ray Spectroscopy (EDS), Optical Microscopy, Laser Scanning Microscopy (LSM), Field Emission Electron Microscopy (FE-SEM) and Atomic force Microscocy (AFM) characteristics and parameters are mentioned.

3.1 Manufacturing process of the sensing element

The manufacturing process of the sensing element presented in this study is based as a field effect transistor with a liquid gate (a similar structure is show in Figure 2.7). The substrate was obtained from Graphenea [125]. This substrate is a monolayer graphene transferred to a silicon - silicon dioxide wafers, with thicknesses of 500 μm and 285 nm respectively, the dimensions of the wafers were 10 x 10 mm^2 fabricated by chemical vapor deposition.

Therefore, fabrication process started by positioning the substrates into a thermal evaporator (Quorum Q150R ES Figure 3.1 (B)) for gold deposition to create the source and drain electrodes. For this deposition, a copper mask with the dimensions required of three electrodes of 10 x 1 mm^2 was used and aligned on the substrate (Figure 3.1 (A)). The evaporator parameters that were used for gold deposition in all the devices manufactured were: Sputtering current of 50 mA, tooling factor of 2.70 and time of exposure of the sample of 300 s.

After the deposition of the electrodes, the substrates were exposed to a thermal annealing process at 250 °C for 30 min in order to reduce graphene defects, eliminate adsorbed species and to lower the contact resistance. A vacuum furnace with nitrogen gas flow shown in Figure 3.2 was used.

Afterward applying the thermal annealing process, a polydimethylsiloxane container (PDMS) was applied manually over the source and drain electrodes for protection and for electrical insulation (Figure 3.3). The wall of PDMS also serves as a container for the solutions that were added in the following steps. This process creates two sensing elements per graphene
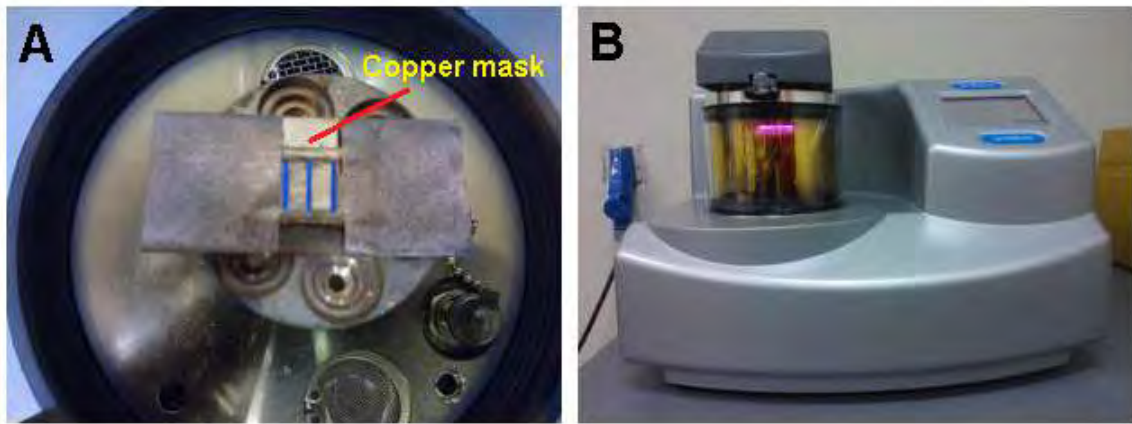
Figure 3.1: Process of deposition of the gold electrodes on the substrate with graphene. A) Alignment of the mask with the dimensions of the electrodes to be deposited on graphene. B) Equipment for the deposition of metals by thermal evaporation Quorum Q150R ES.
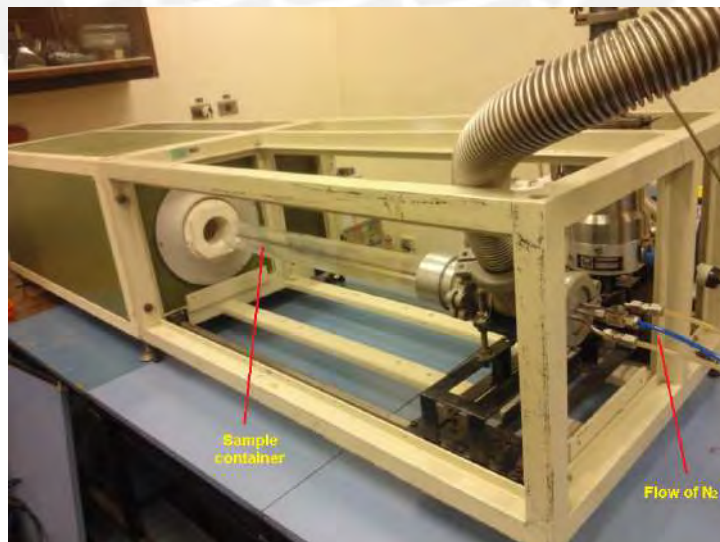
Figure 3.2: Thermal annealing furnace with vacuum system and nitrogen gas flow.

substrate with an active area of approximately 3.5 x 7 mm^2.
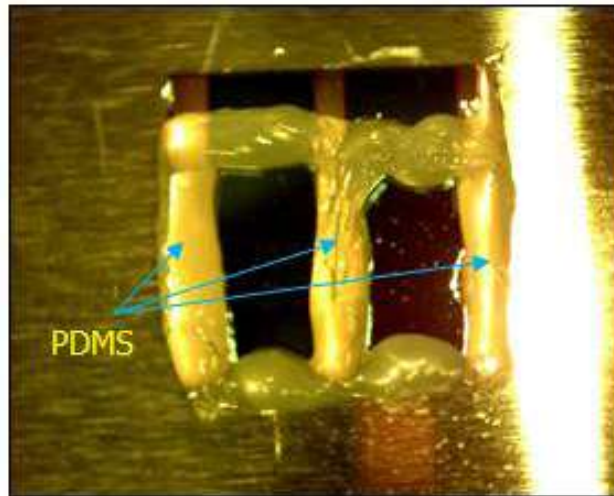
Figure 3.3: PDMS protection on the sensing element.

The succinimidyl ester of 1-pyrenebutanoic acid (PBASE) dissolved in methanol at a concentration of 4.6 x 10^{-7} mg/mL was used as a linker (Sigma-Aldrich) between the graphene surface and the oligonucleotide, the linker will have an interaction π - π with the surface graphene (see Figure 3.4). For each transistor (sensing element), 30 μL of the linker-methanol solution were deposited by drop casting technique, and was let dry for 4 hours until the methanol was completely evaporated.
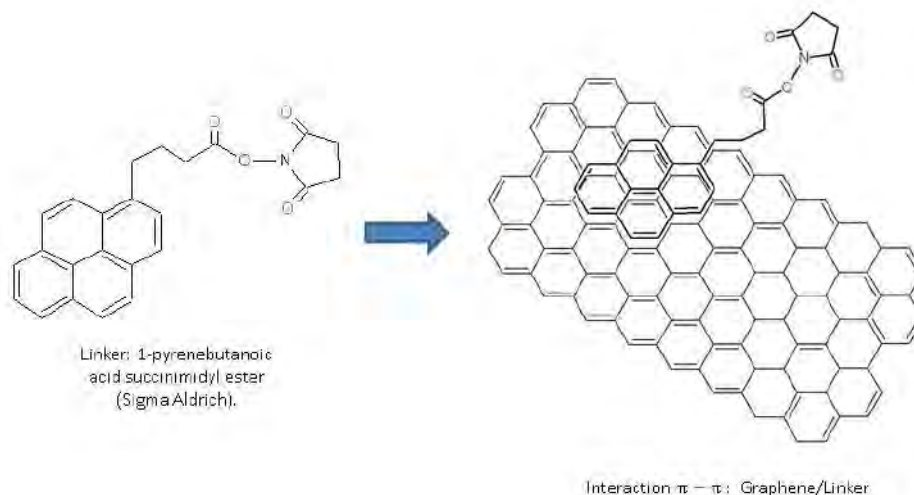
Figure 3.4: Structure of the linker.

The recognition oligonucleotide (probe) chain 5' - CCA GGT CGA CAC ATA GGT GAG GTC- 3' modified with amine in 5', which was dissolved in phosphate buffer solution (PBS)

with pH 8.6, was used. This modification of amine in 5' will have an effective interaction between the oligonucleotide and the linker with a strong amide covalent bond. 30 μL of DNA probe solution were deposited over the linker by drop casting technique. The time for promoting bonding between linker and probe DNA was 16 hours. With the addition of the oligonucleotide (see Figure 3.5) the manufacturing process of the sensing element is completed, and then the elements that allow us to evaluate the performance of the sensing elements are added, the Figure 3.6 shows its final structure.
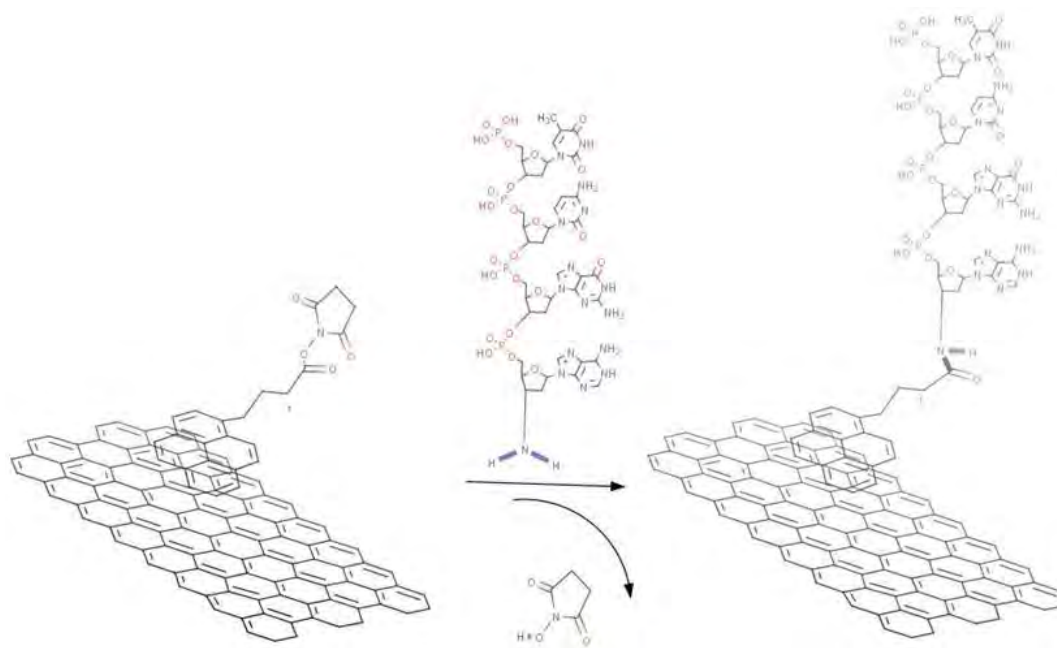
Figure 3.5: Resulting structure with the addition of oligonucleotide (probe).

As a "DNA Target" sequence the complementary strand 5' - GGT CCA GCT GTG TAT CCA CTC CAG - 3' specific for Mycobacterium Tuberculosis dissolved in PBS (pH 8.6) was used. To evaluate the specificity a "Non-complementary DNA" as a mismatched sequence 5' - CCT GCG AGC GTA GGC GTC GGT GAC - 3' with no amine modification was used in another sample after the adittion of the probe. Both "DNA Target" and "Non-complementary DNA" were dissolved in PBS with a concentration of 0.01 nM and added at a temperature of 60°C by drop casting technique. All DNA sequences were synthesized and supplied by ThermoFisher Scientific (Invitrogen) [126].

Measurements were conducted in the following stages and identified accordingly: only graphene (G), graphene with linker (G-L), graphene with linker and probe DNA (G-L-O), after hybridization with "DNA Target" (G-L-O-T) and a different sample with "Non-complementary DNA" (G-L-O-NC). All the mentioned steps are summarized in the Figure 3.7.
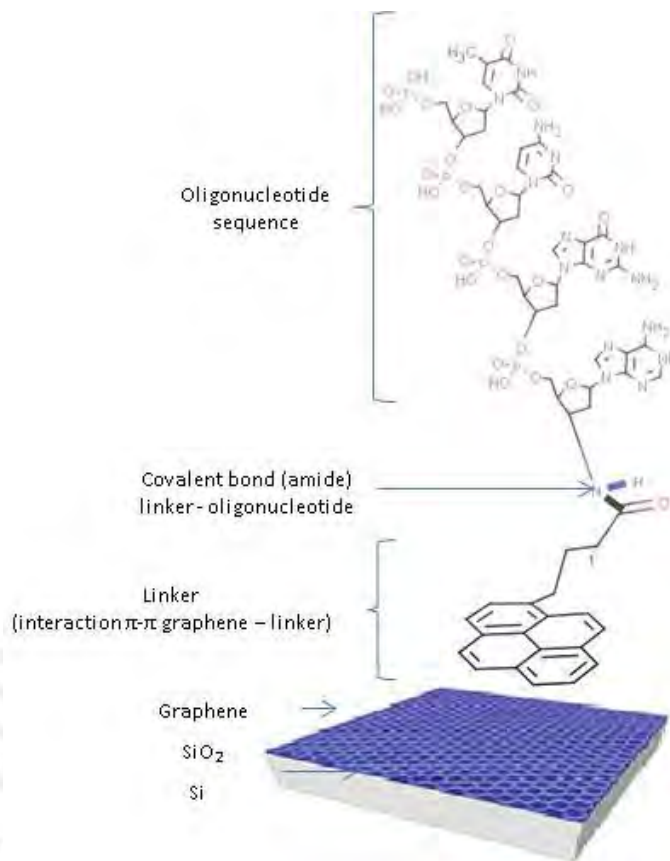
Figure 3.6: Final structure of the sensing element.
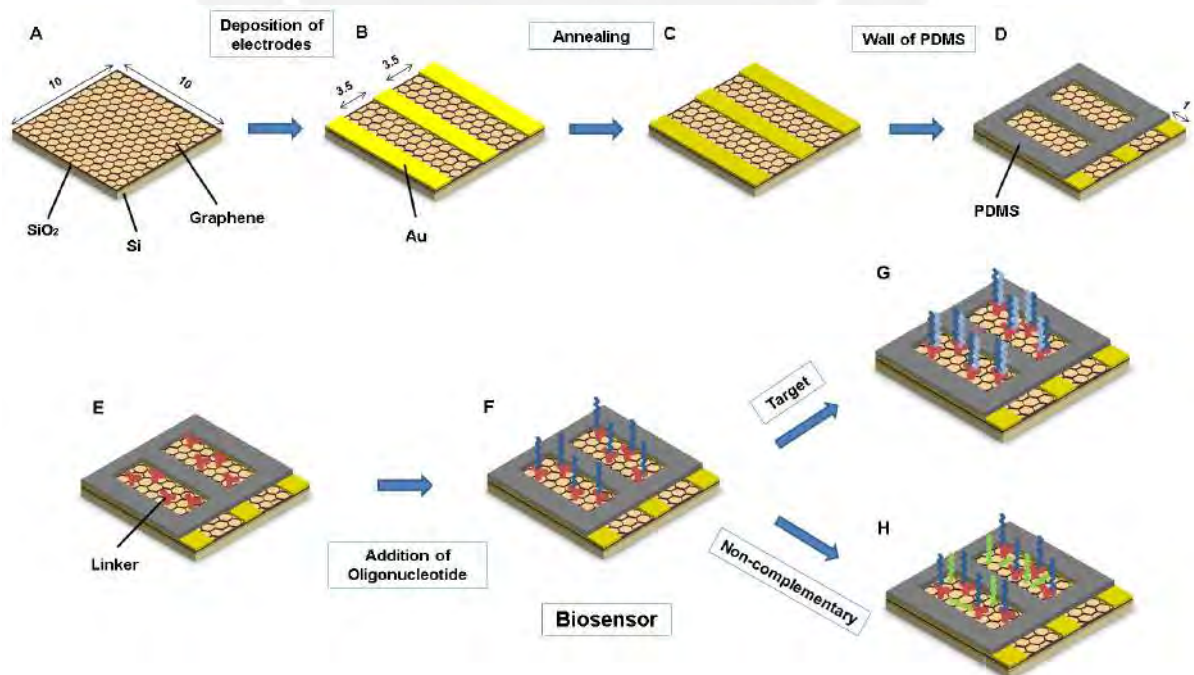
Figure 3.7: Step by step of the manufacturing process.

3.2 Characterization techniques

3.2.1 Structural and chemical

3.2.1.1 Raman Spectroscopy

The graphene on the Si/SiO_2 sustrate was fabricated by CVD, in order to verify the graphene structure, Raman spectrum was taken using Qontor inVia Raman microscope with a 514 nm excitation input. Also the Raman spectra was taken in order to analyze the structure of the interaction area and the behavior with the linker and the nitrogenous bases. An analysis range of 450 to 3200 cm^{-1} was used in order to find the different signals of the aggregated elements.

3.2.1.2 Energy Dispersive X-ray Spectroscopy (EDS)

To evaluate the chemical composition of the sample at each step of the fabrication, an EDS detector (Thermo SDD-Detector System NORAN7) installed in a FESEM Hitachi S4800-II was used.

The elements present in the sensing element that should be present in the result of the chemical analysis are the following:

- Substrate:
    - Si, SiO_2, C
- Addition of Linker
    - Linker: 1-pyrenebutanoic acid, succinimidyl ester (PBASE) ($C_{24}H_{19}NO_4$)
    - Solution: Methanol (CH_3OH)
- Addition of Oligonucleotide (also "DNA Target" and "Non-complementary DNA")
    - Nitrogenous bases
        * Probe: 5' - CCA GGT CGA CAC ATA GGT GAG GTC- 3'
        * DNA Target: 5' - GGT CCA GCT GTG TAT CCA CTC CAG - 3'
        * Non-complementary DNA: 5' - CCT GCG AGC GTA GGC GTC GGT GAC - 3'
    - Phosphate buffer solution (PBS) - Composed of the salts : Na_2HPO_4 + KH_2PO_4

As for the voltage used, this must be at least two times for the highest energy line and no more than 10 to 20 times the lowest energy line of interest. Because at lower voltages the fraction of the interaction volume where the element can be excited becomes very small and one will not be able to generate many X-rays of that energy. When the voltage number is excessive, the proportion of the interaction volume for which the low energy x rays can escape without being absorbed also becomes small giving a small peak [89]. Since EDS is not accurate for low atomic number elements (C, B, N, O) a 5 kV was used for bare graphene. Line scan analysis was performed at 20 kV for the Au electrode chemical composition variation. 10 kV for G-L, G-L-O, G-L-O-T and G-L-O-NC was used. The time of acquisition of all measures was 90 seconds.

3.2.2 Morphological

3.2.2.1 Optical Microscopy

Optical microscopy characterization was performed with a Leica DMI 500M inverse system microscope with a Digital Camara DFC 450C and the software Leica Application Suite to observe possible defects or presence of multilayers in the basic morphology of the substrate. Images were taken at 500X and 1000X.

3.2.2.2 Laser Scanning Microscopy (LSM)

In order to evaluate the height of the deposition of gold electrodes with respect to the surface of graphene a 3D-Laser-Scanning-Microscope LEXT OLS4100 was used at 100X.

3.2.2.3 Field Emission Scanning Electron Microscopy (FESEM)

To evaluate the surface and topography contrast a Field Emission Scanning Electron Microscopy Hitachi S 4800-II was used. This FESEM is equipped with the following detectors:

- SE detector in sample chamber

- SE detector above the objective lens (through-the-lense detector) with energy filter (ExB filter)

- BSE detector (photodiode detector)

- EDS detector (Thermo SDD detector system NORAN7)

- STEM detector

A scheme of detector related to the signal information is shown in Figure 3.8. The Upper SE detector provides surface information (including voltage contrast), the Lower SE topographic contrast and the Uppper SE(BSE) compositional with topographic information. In

this thesis Upper SE together with Lower SE was used, giving the label SE(M) in the images and also the Upper SE(BSE) detector with the label SE(U,LAX) in the images. Images were taken with 5 kV for bare graphene and 10 kV for all the following steps mentioned. A extractor current of 10 μA, a probe current set to normal, Focus Mose set to Ultra High Resolution and a working distance equal to or greater than the Z height of the stage were also used.
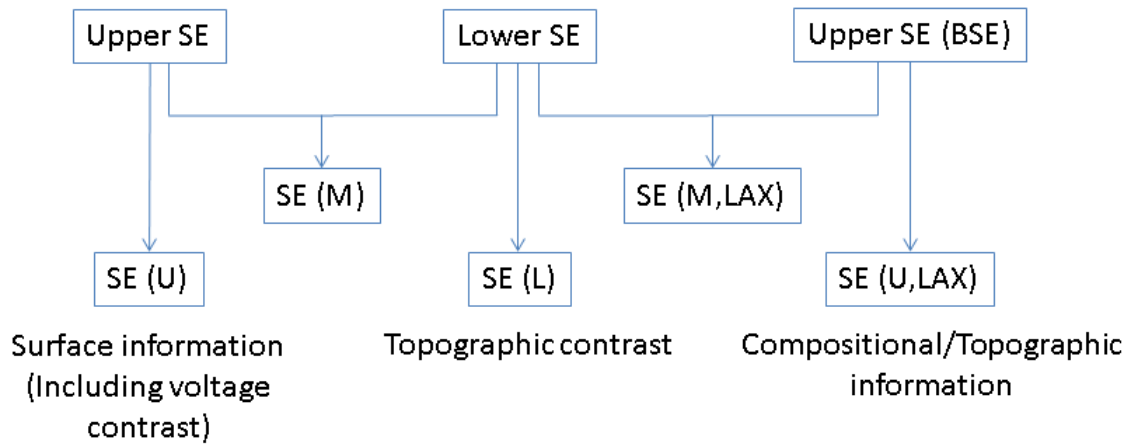
Figure 3.8: Scheme of detector related to the signal information.

3.2.2.4 Atomic Force Microscopy (AFM)

The results in the AFM will give more information on the topography in each stage of the manufacturing process of the sensing element and the detection process. The AFM gives greater resolution in images of 10 x 10 μm. An AFM Cypher SPM System Asylum Research was used. The AFM was set to Tapping Mode, FB gain of 0.3 and a set point of 5 with a NSG10 silicon AFM cantilever.

4 Results and discussion

This chapter is dedicated to present and discuss the results of the characterization of the nanostructured sensing element fabricated as explained in the previous chapter (Figure 3.7). The discussion follows the sequence of fabrication, stage by stage. The stages correspond to: bare graphene, gold deposition + annealing, addition of the linker and the addition of the oligonucleotide (probe). Additionally, two sensing elements were characterized, one with the addition of the "DNA Target" and the other with the "Non-complementary DNA". The characterization contemplated the analysis by: Optical Microscopy, Laser Scanning Microscopy, Atomic Force Microscopy (AFM), Field Emission Scanning Electron Microscopy (FESEM), Energy Dispersive X-ray Spectroscopy (EDS) and Raman Spectroscopy. Each of these techniques served to find particular characteristics in each stage and to elucidate, the behavior of the aggregated molecules over the surface of the sensing element.

4.1 Bare graphene

Many researchers have been in the search for an appropriate substrate where in the wavelength range of maximal sensitivity one can achieve the maximum optical contrast of the carbon atom monolayer . In the case of commonly used oxide-covered silicon wafers, by adjusting the silica thickness to 90 or 300 nm, the reflected light intensity is maximal at about 550 nm, that is at the maximum of the human eye sensitivity [127]. The contrast between graphene and the substrate can be as high as 12% so the short optical path added by graphene (monolayer) can be easily seen [56]. Graphene used in this thesis work was deposited over a SiO_2 thickness of 285 nm so Figure 4.1(A) shows that at 500X it is possible to distinguish folding lines (red arrows), Figure 4.1(B) at 1000X folding lines were observed and small areas of multilayer graphene islands (yellow circles).

Also, the surface of bare graphene was analyzed at 5 kV and detector setting of SE(M), since the volume of interaction is less and allows us to observe the details in the small thickness of graphene over the SiO_2 surface. Figures 4.2 (A-E) depict that is possible to observe the graphene at different magnification levels (1000X, 4500X, 10 000X, 20 000X, 30 000X respectively) were it is important to note regions of multilayer graphene (yellow circles) and also the presence of several folding lines (red arrows) very similar to Jaesung Lee et al. investigation [128].
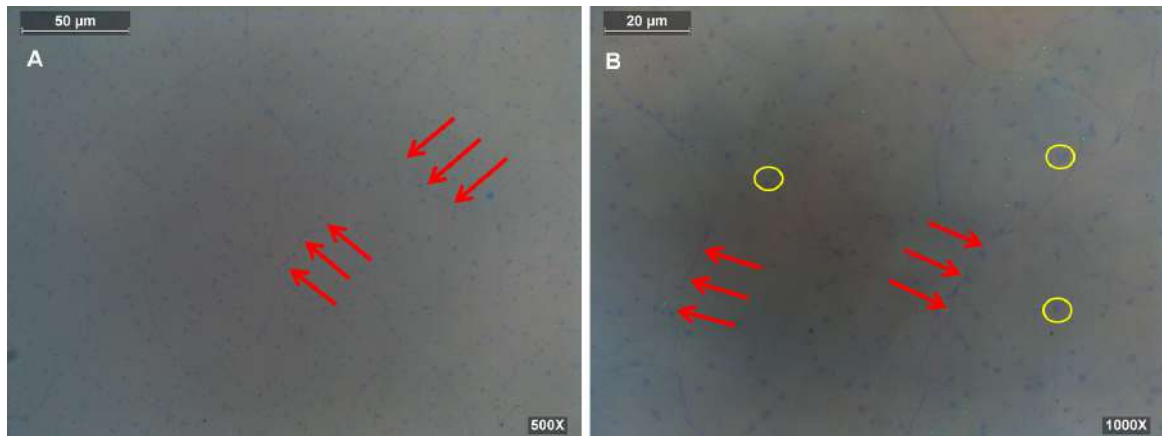
Figure 4.1: Optical microscopy of bare graphene. (A)500X, (B)1000X.
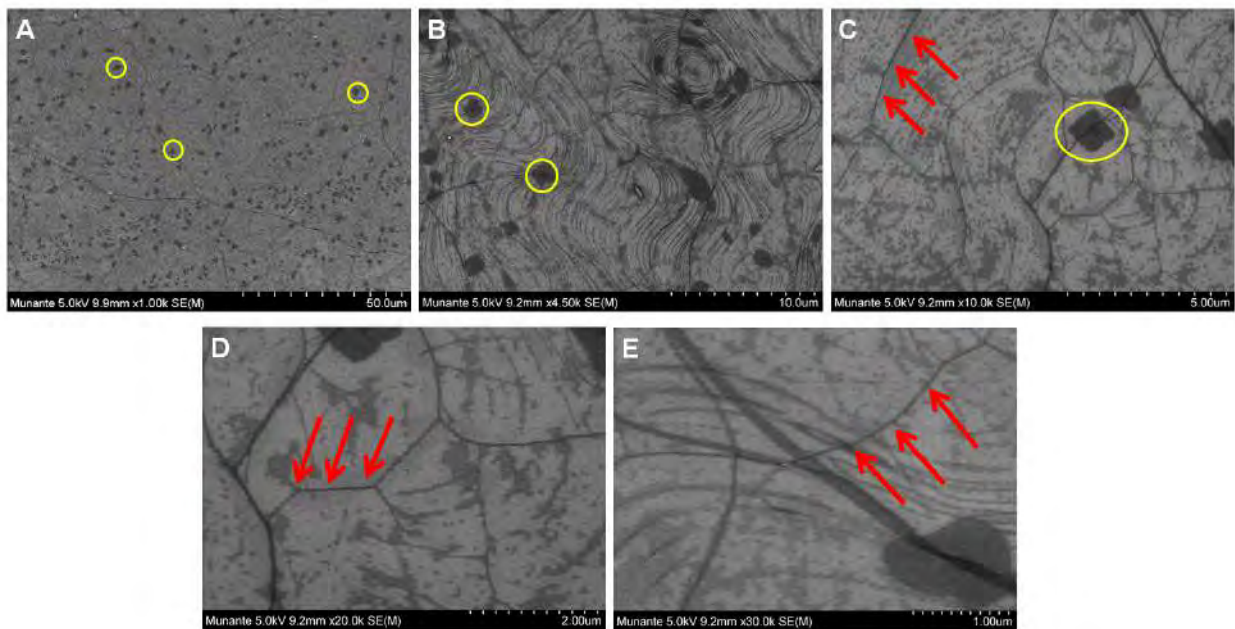
Figure 4.2: 5kV FESEM images of bare graphene. All samples were performed using SE(M) mode. (A)1000X, (B)4500X, (C)10 000X, (D)20 000X, (E)30 000X.

AFM analysis shown in Figures 4.3 and 4.4 two different areas of the graphene channel before the annealing designated as A1 and A2 respectively. They show that the average height of the graphene surface above the substrate is ~ 2 nm for both areas. There is also fencing like structures indicated with blue arrows of ~ 7 nm for A1 and ~ 4.5 nm for A2. Also the RMS surface roughnesses were 3.224 and 1.586 nm for A1 and A2 respectively, showing that the roughness varies according to the different areas taken.

An EDS at 5kV was performed over the surface of the graphene, the main elements that correspond to the graphene substrate (C, O, Si) were observed (Figure 4.5).
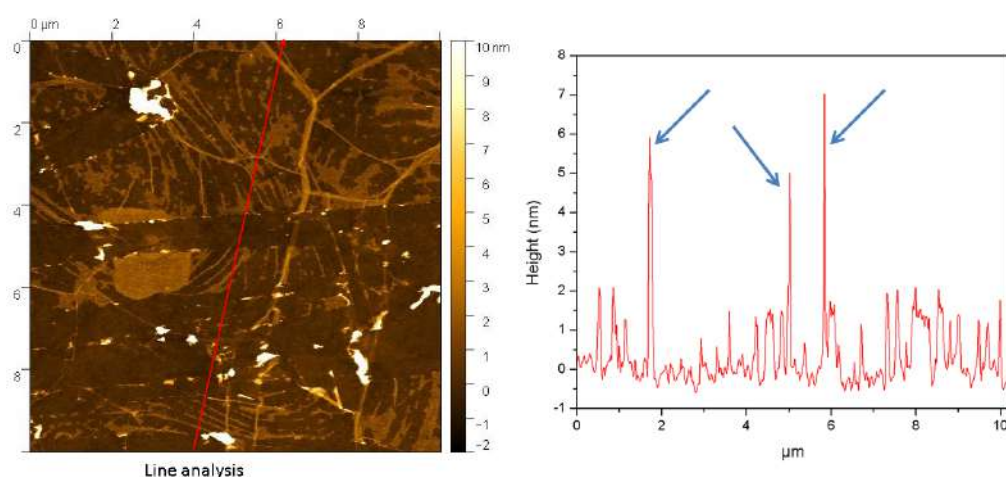
Figure 4.3: AFM image of graphene channel before annealing (left) and line analysis (right) taken in A1 area.
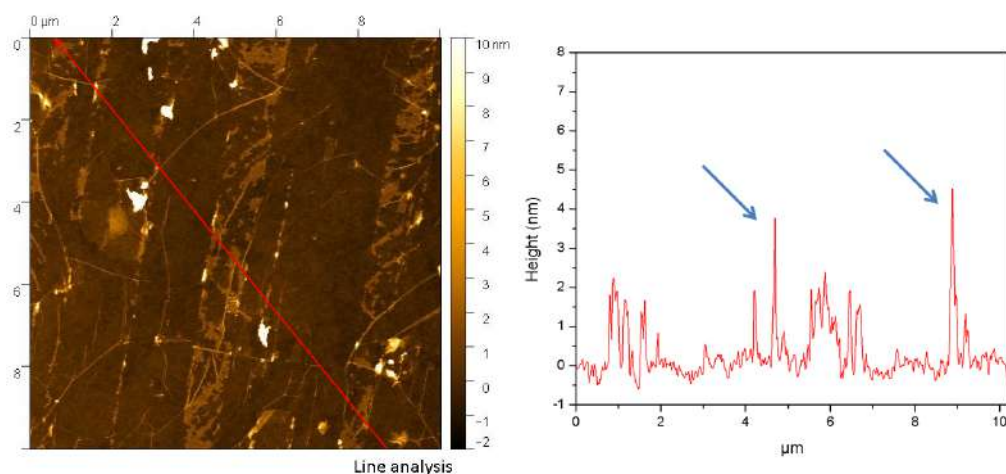
Figure 4.4: AFM image of graphene channel before annealing (left) and line analysis (right) taken in A2 area.

A raman spectroscopy analisis was performed over the bare graphene surface to evaluate their structure, according to the results (Figure 4.6) the G and 2D (G') peaks were found at around 1592 and 2690 cm^{-1} respectively. The G band is due to E$_{2g}$ mode at the gamma point which stems from the stretching of the C-C bond in graphitic materials. The 2D (G') band is related to identify the number of layers by the shape and intensity of the signal. The intensity ratio of the 2D Raman peak to the G peak was about 1.4, representing the monolayer characteristics of the graphene film (monolayer structure if ratio >1), this result is very similar to the data provided by Graphenea [125]. Additionally, a low intensity band is observed at 1350 cm^{-1}, which suggests the presence of small defects, particularly related to vacancies, dislocations and mechanical deformations.
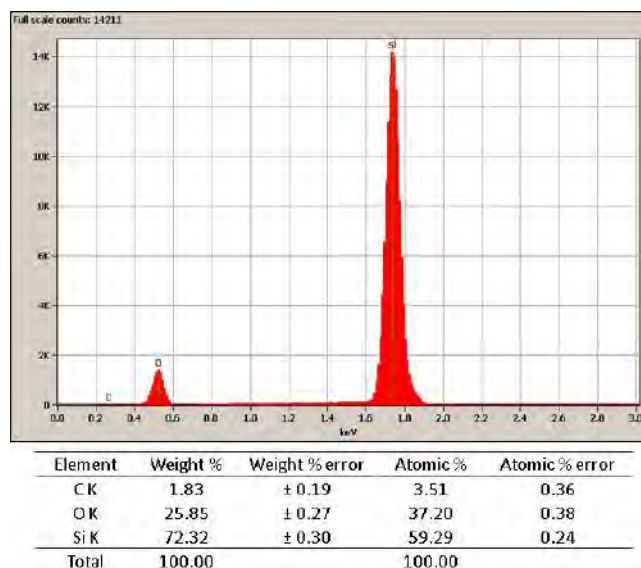
Figure 4.5: Eds at 5kV analysis of bare graphene.
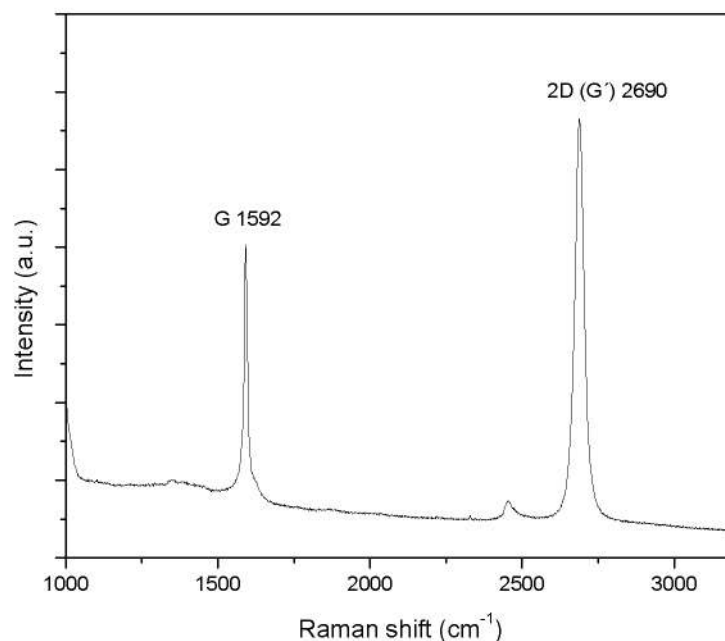
Figure 4.6: Raman spectra of bare graphene.

4.2 Bare graphene, gold deposition + annealing

By using Laser Scanning Microscopy it was possible to evaluate the transition step between the gold eletrodes and the surface of the graphene, it can be seen in Figure 4.7(A) that this step covers a length of approximately 70 μm. An analysis of the cross section reveals that

the height of the electrodes is about 175 nm (see Figure 4.7(B)).
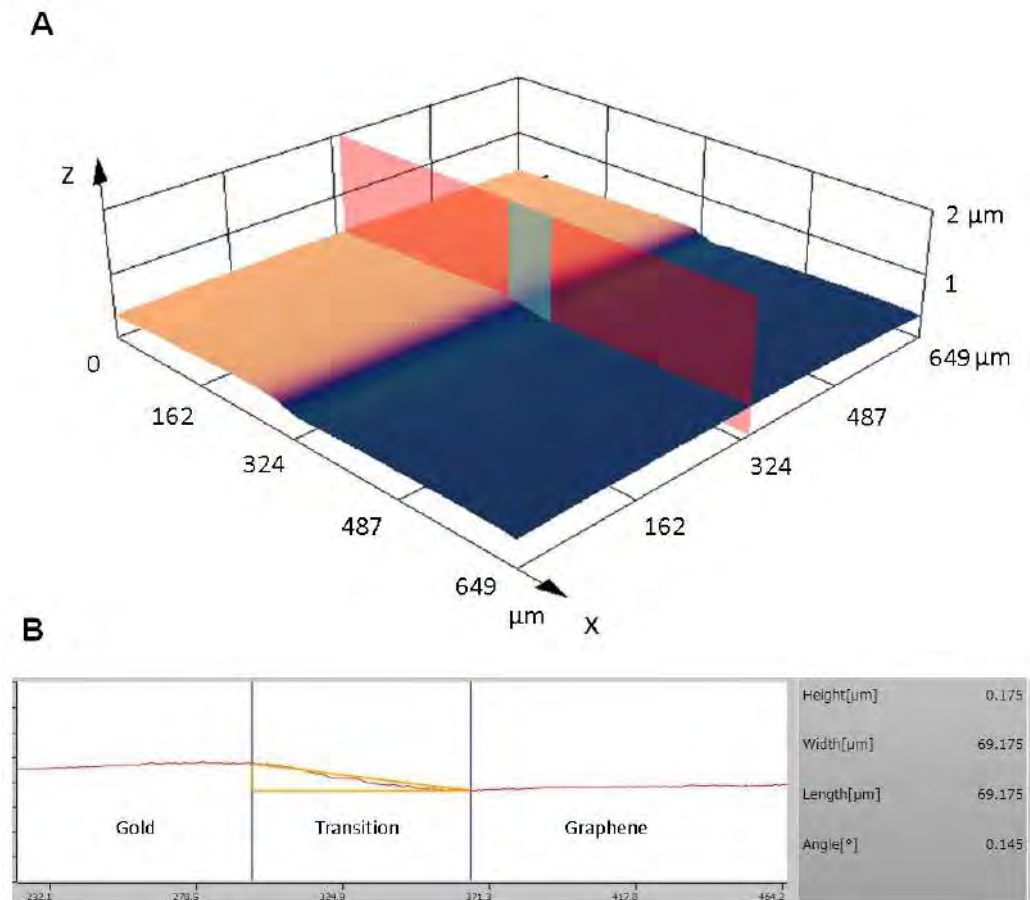
Figure 4.7: Interface between the gold electrodes and graphene.

As mentioned in 4.1 the substrate was annealed at 250°C with nitrogen gas flow for 30 min after the deposition of the Au electrodes. The intention of this annealing process was to improve the interaction with the linker by cleaning the surface of the graphene and also improve the contact resistances demonstrated by AFM analysis for Wojcik et al. [72]. The improvement in the electrical characteristics by the annealing process in this present sensing element is mentioned in a previous investigation where the electrical resistance of graphene was reduced by $38\% \pm 15\%$ [129].

The images in Figure 4.8 correspond to a FESEM characterization at 10 kV. They show the interface between the electrode of gold and the graphene, Figures 4.8(A) and (B) at 50X and 4500X respectively, depict the distribution of gold on the surface of graphene. Since the interface is around 70 μm the presence of the gold is increasing throughout this length as the Figures 4.8 (C) to (E) show (red arrow direction) at 10 000X. It was observed that the gold content on the surface is gradual and not staggered. Also a EDS line scan at 20 kV was performed, the increase of the Au concentration in all the section of this length is

observed (Figure 4.9) with a smooth transition at the interphase, possible generated during the annealing process where The vertical black line shows the beginning of this transition.

The surface of the Au electrodes was also evaluated at 30 000X (Figure 4.10), where it is possible to observe that the gold is homogeneous and appropriately deposited over the graphene surface and with the non existence of areas with little Au concentration or defects.
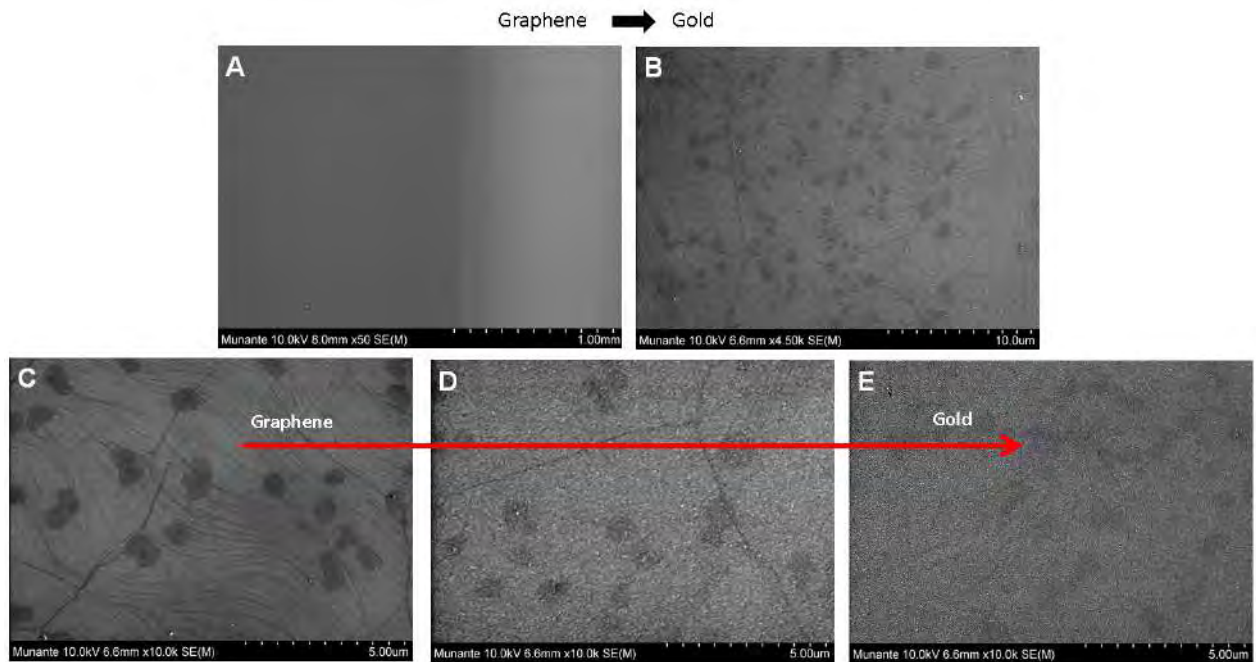
Figure 4.8: 10kV FESEM images of interface between Au electrodes and graphene. All images were performed using SE(M) mode. (A)50X, (B)450X, (C-E)10 000X.

The AFM analysis of the graphene channel after the annealing process was performed in two different areas designated as B1 (Figure 4.11) and B2 (Figure 4.12). They show an improvement in height characteristics. The images show that the average height of the graphene surface above the substrate after the annealing was reduced to < 1.5 nm in both areas. The height profile also shows fencing structures of ∼ 2.3 nm in B2 area (blue arrows in Figure 4.12). Comparing the two AFM images it can be noticed that there were some defects of graphene and contamination of the environment that were removed after the annealing. Additionally the RMS surface roughnesses were 1.427 and 1.430 nm for area B1 and B2 respectively, these results indicate a smoother and cleaner graphene area unlike the 3.224 and 1.586 nm values for the bare graphene. As mentioned before the surface quality of graphene is of vital importance for its use as a FET biosensor demonstrated by Jin Heak Jung et al. [117] and Wojcik et al. [72].
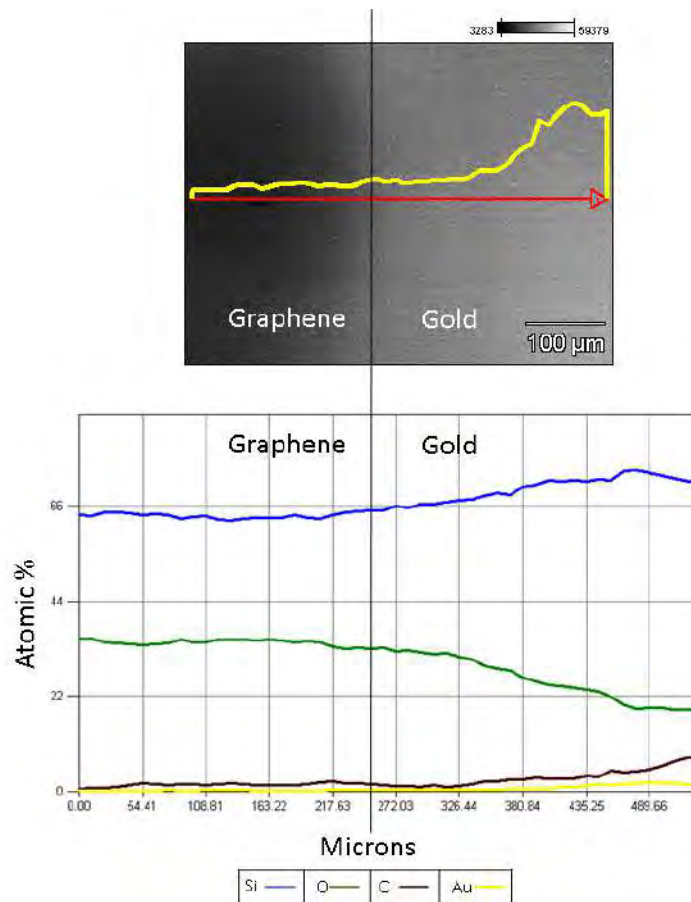
Figure 4.9: EDS Line Scan of the interface between Au electrodes and graphene performed at 20 kV.
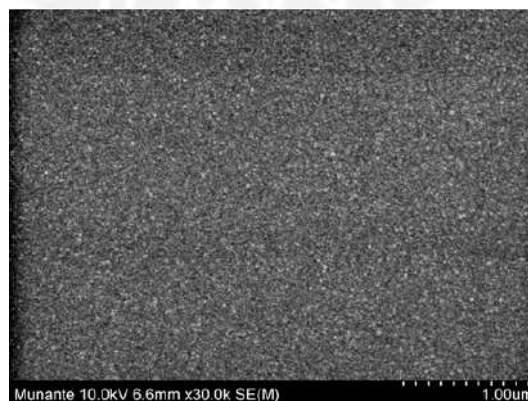
Figure 4.10: 10kV FESEM image of the Au electrode surface at 30 000X. Image was performed using SE(M).

52
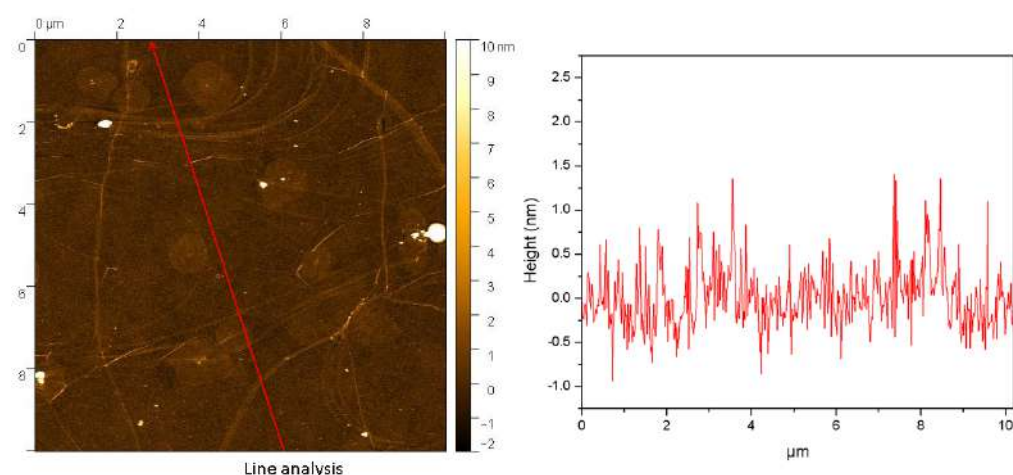
Figure 4.11: AFM image of graphene channel after annealing (left) and line analysis (right) taken in B1 area.
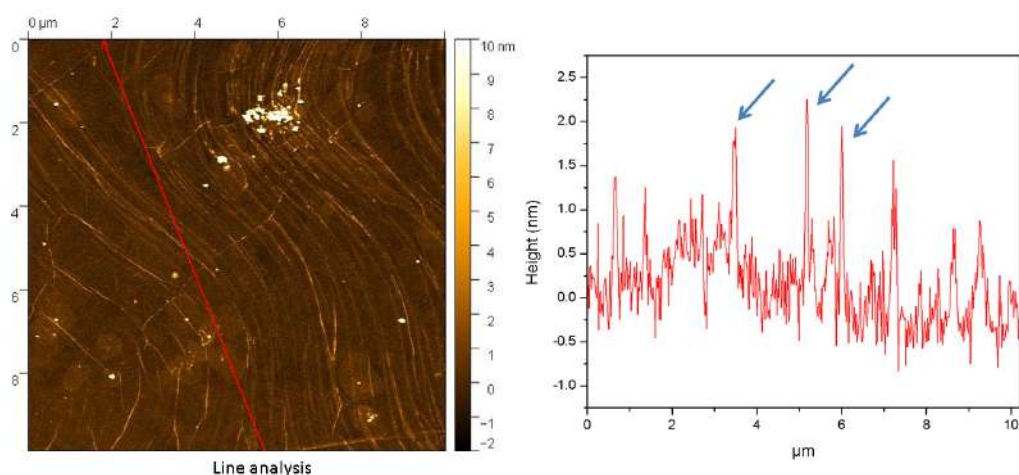
Figure 4.12: AFM image of graphene channel after annealing (left) and line analysis (right) taken in B2 area.

4.3 Addition of the linker

In the process of the addition of the linker (solubilized in methanol) and after the drying of the solution on the surface, two areas with different morphology can be observed in the FE-SEM images (Figure 4.13(A) at 50X) performed on the graphene channel since the solution dry over the surface first and then in the borders. Figure 4.13 (B-C) show zones that are close to the edge of the PDMS wall performed at 10 kV and 1000X, the solution dry at the end showing that there are some agglomerations of the solution on the surface. The images (B) and (C) are the same but with different detector setting of SE(M) and SE(U,LA100) respectively. Since the agglomerations generate a differentiation in the chemical composition it is observed that the image (C) performed with SE(U,LA100) provides more information,

emphasized the analysis of the edges to the compositinal/topographic information, thus improving the depth of field in this zone.

On the other hand, Figure 4.13 (D-E) show zones in the middle of the graphene channel performed at 10kV and 1000X, where it is possible to observe that the surface is complete homogeneous showing tenuously some areas of islands of graphene (yellow circles). Also, images (D) and (E) are the same but with different detector setting of SE(M) and SE(U,LA100) respectively. Since it is wanted to observe how the molecules to add are embedded in the surface, the detector SE(M) gives more information focusing on the surface information and topographic contrast.
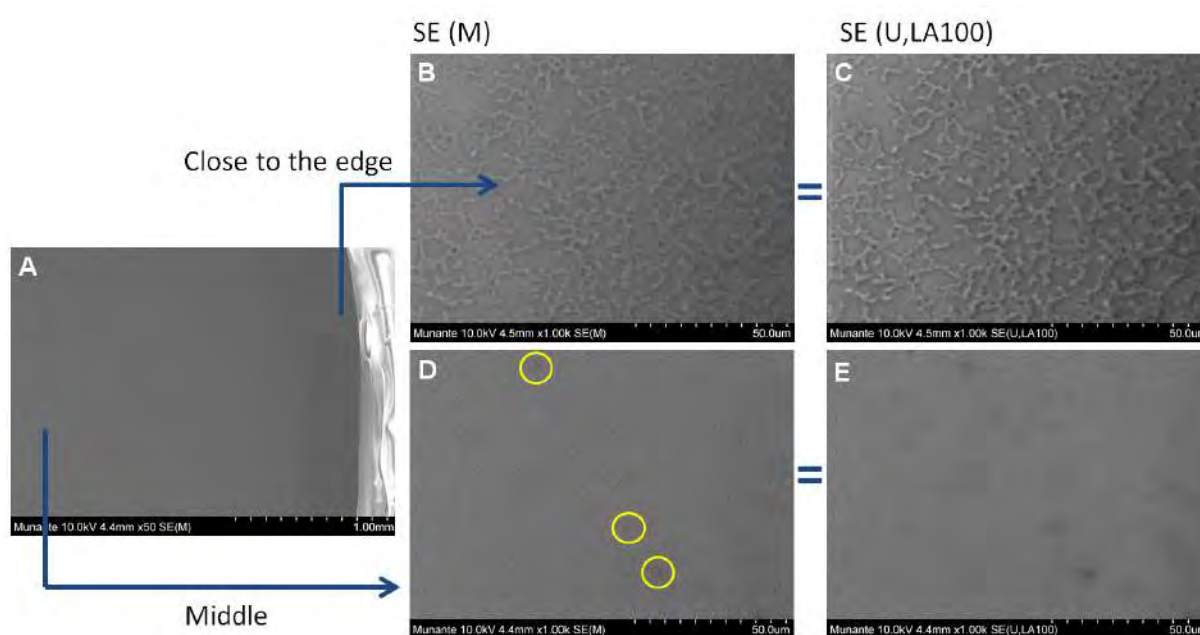
Figure 4.13: 10kV FESEM images of the graphene channel with the addition of Linker. (A)50X - SE(M), (B) and (C) are the same image close to the edge but with detector setting of SE(M) and SE(U,LA100) at 1000X respectively. (D) and (E) same image in the middle but with detector setting of SE(M) and SE(U,LA100) at 1000X respectively.

An AFM analysis of the graphene channel is shown in the Figure 4.14 where the average height of the element above the surface obtained by line analysis as indicated is $\sim$<5 nm with fencing like structures of around $\sim$8 nm (blue arrows). The RMS surface roughnesses was 2.235 nm which is a notable increase compared to the 1.427 and 1.430 nm for the annealing graphene.

Figure 4.14: AFM image of graphene channel after addition of linker (left) and line analysis (right).

An EDS at 10 kV was performed over the graphene channel, the main elements that correspond to the graphene substrate (C, O, Si) (Figure 4.15) were observed, very similar to bare graphene (Figure 4.5), but with higher concentration of oxygen and less carbon due to the addition of the solution.

Element	Weight %	Weight % error	Atomic %	Atomic % error
C K	0.94	± 0.16	1.75	0.29
O K	32.54	± 0.36	45.39	0.50
Si K	66.52	± 0.41	52.86	0.32
Total	100.00		100.00	
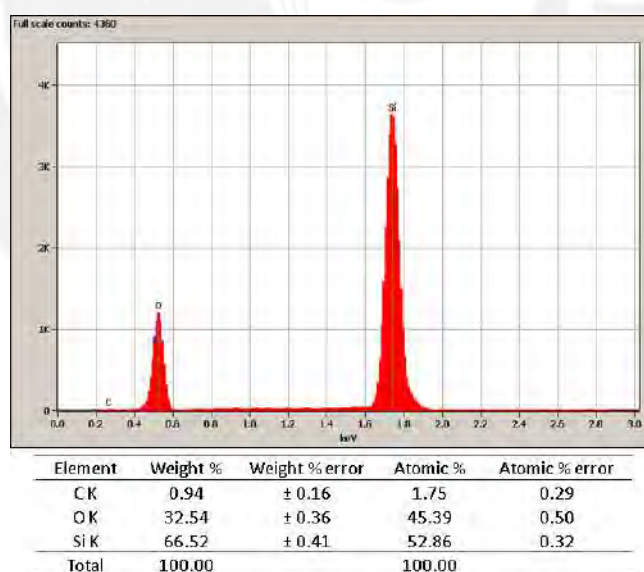
Figure 4.15: EDS at 10kV analysis of graphene channel in after addition of linker.

4.4 Nanostructured sensing element (addition of the probe)

Subsequently, in the process of the addition of the probe (dissolved in PBS) and after the drying of the solution on the surface, a pattern similar to the addition of the linker can be observed in the FESEM image (Figure 4.16 (A) performed at 10 kV, detector setting of SE(M) and at 50X) where the solution is first dried in the center and at the end at the edges. Figures 4.16 (B) and (D) performed at 10 kV, detector setting of SE(M) and at 1000X and 4500X respectively show the central zone of the graphene channel where a homogeneous surface is observed free of defects. On the other hand, Figures 4.16 (C) and (E) performed at 10 kV, detector setting of SE(U,LA100) and at 1000X and 4500X respectively depict similar agglomerations of the solution added but with a different morphology than when the linker was added and are presumed to be segregated from the salts contained in the phosphate buffer solution (PBS).

The AFM analysis was performed to make sure that the probe was properly immobilized on the interaction area surface of the graphene channel. The AFM image in Figure 4.17 shows structures roughly a few hundred nanometers wide and an average of 2.5-7.5 nm tall with fencing like structures of 10 nm and 15 nm approximately (blue arrows in Figure 4.17). Whereas the bare graphene region does not have a distinguishable structure except for a few nanometer tall ridges which might be coming from the fabrication process. The tall structures are assumed to be poles of oligonucletoides with linker binding to the graphene layer which is also confirmed by looking into the height profiles of the red line analysis. The RMS surface roughnesses was 2.306 nm which constitutes an increase in comparison with the addition of the linker.

It is also possible to confirm the relative roughness of the surface using images as inputs and 3D reconstruction converting them in roughness patterns by using the Gwyddion software. Figure 4.18 shows the comparison, with the help of the software, of the sample of graphene with the final part of the manufacturing process of the sensing element(until the probe), where Figures 4.18(A) and (B) were FESEM images performed at high vacuum, 1 kV and 1500X and Figures 4.18(C) and (D) the 3D reconstruction respectively. It can be observed that the surface increases in height but remains homogenous due to a good affinity between the aggregate solutions.
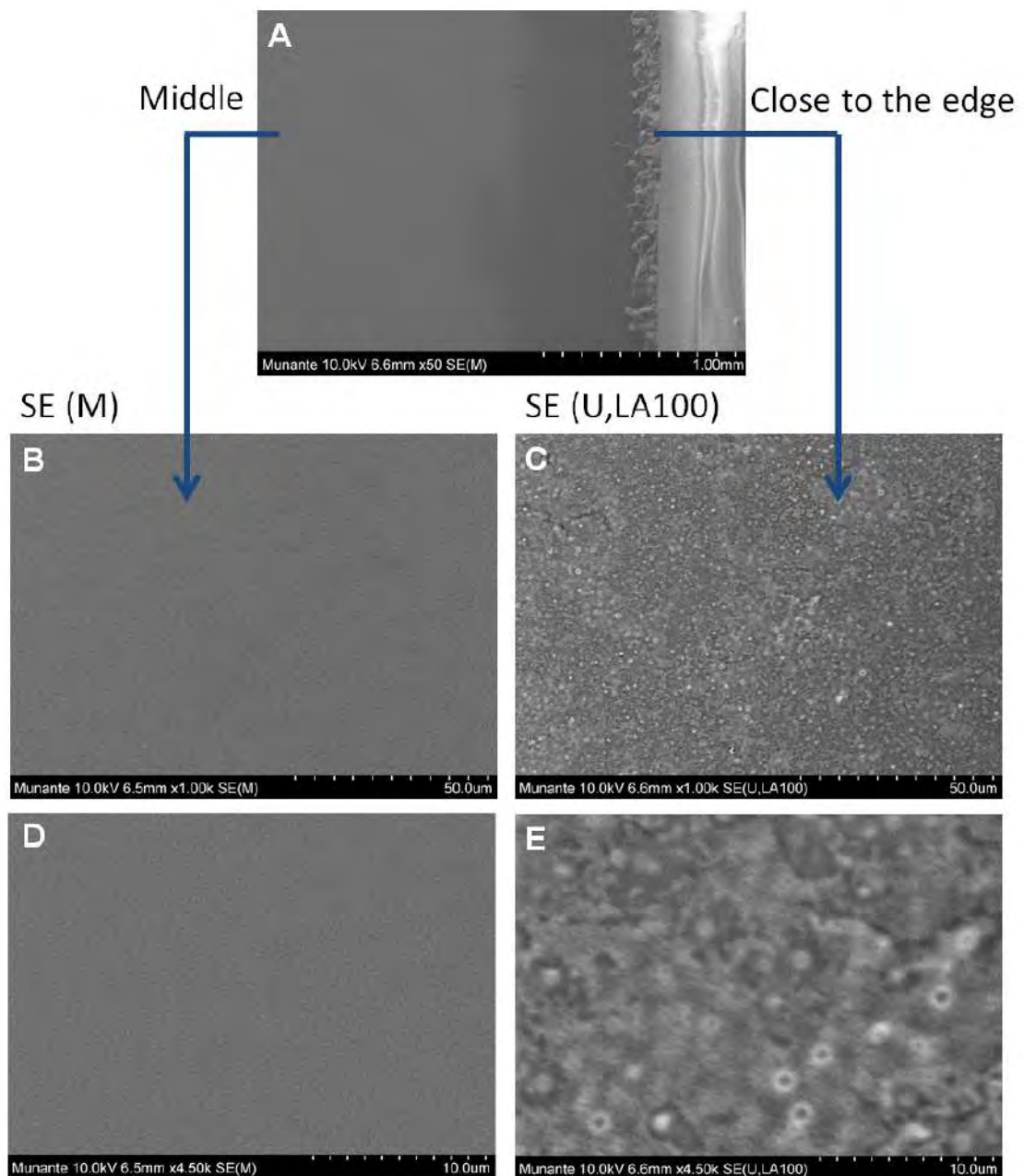
Figure 4.16: 10kV FESEM images of the graphene channel with the addition of oligonu-cleotide (probe). (A) 50X - SE(M). The images to the left (B) and (D) cor-respond to the central area of the GFET using SE(M) at 1000X and 4500X respectively. The images to the right (C) and (E) correspond to the edge of the GFET using SE(U,LA100) at 1000X and 4500X respectively.
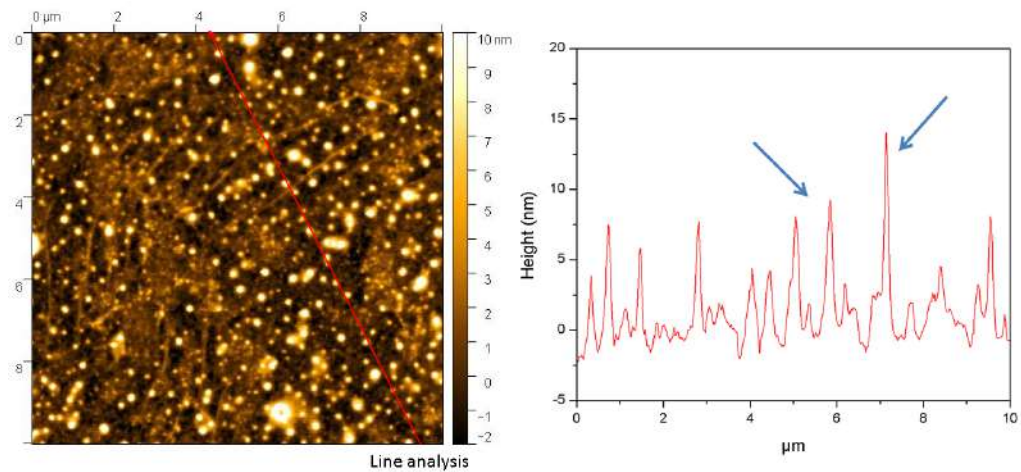
Figure 4.17: AFM image of graphene channel after addition of the probe (left) and line analysis (right).
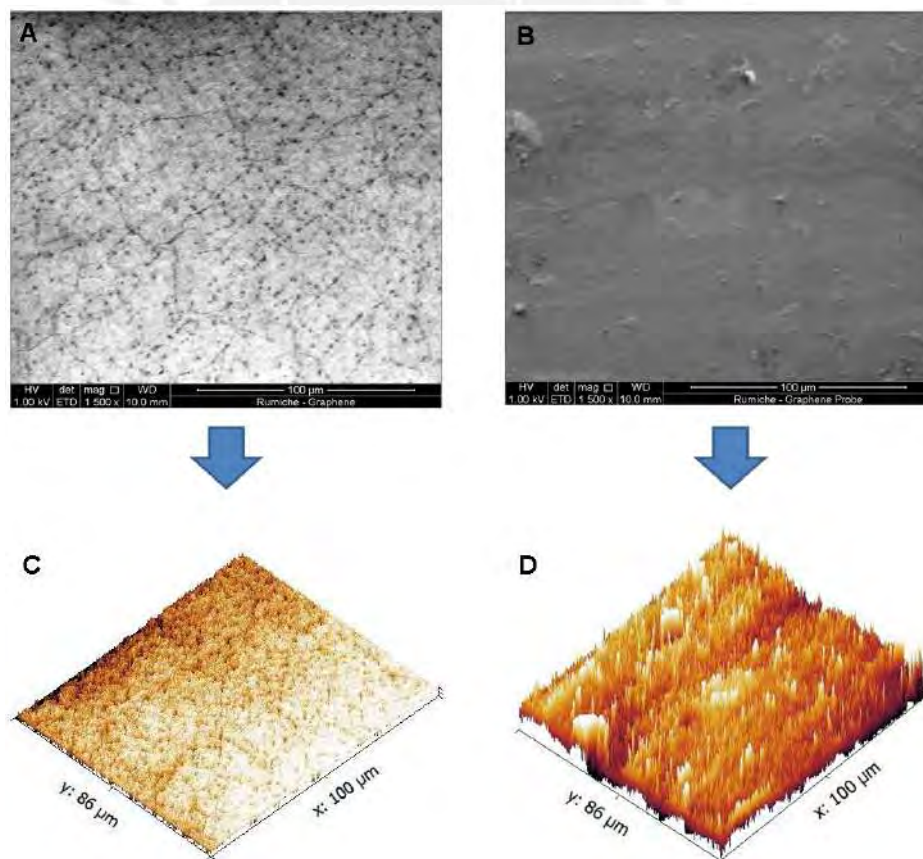
Figure 4.18: Comparing between bare graphene and the sensing element with the probe, through the Gwyddion software.(A) and (B) FESEM images performed at high vacuum, 1 kV and 1500X of G and G-L-O respectively. (C) and (D) 3D reconstruction of G and G-L-O respectively.

A EDS at 10 kV was performed over the interaction area of the graphene channel in two different zones, in the middle and close to the edge. The results in Figure 4.19 performed in the middle show the presence of sodium on the surface and the results of Figure 4.20 performed in the edges show, in addition to the presence of sodium, a small percentage of phosphorus. These elements belong to the salts that make up the phosphate buffer solution (PBS) and that correspond to the FESEM images on Figures 4.16(C) and (E).

Element	Weight %	Weight % error	Atomic %	Atomic % error
C K	0.92	± 0.12	1.71	0.23
O K	32.24	± 0.34	45.06	0.47
Na K	0.11	± 0.05	0.11	0.05
Si K	66.72	± 0.39	53.12	0.31
Total	100.00		100.00	
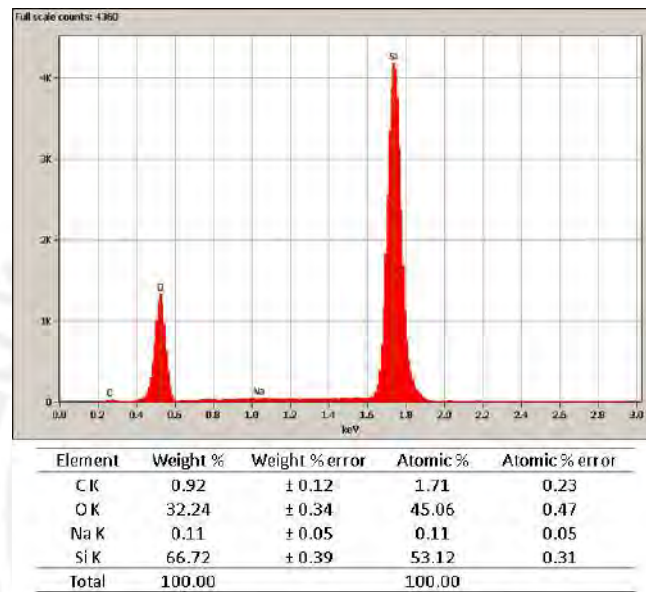
Figure 4.19: EDS at 10kV analysis of graphene channel (middle) after addition of the probe.

Element	Weight %	Weight % error	Atomic %	Atomic % error
C K	1.38	± 0.2	2.52	0.36
O K	34.64	± 0.36	47.27	0.49
Na K	3.50	± 0.11	3.33	0.11
Si K	57.70	± 0.39	44.90	0.31
P K	2.80	± 0.2	1.98	0.14
Total	100.00		100.00	
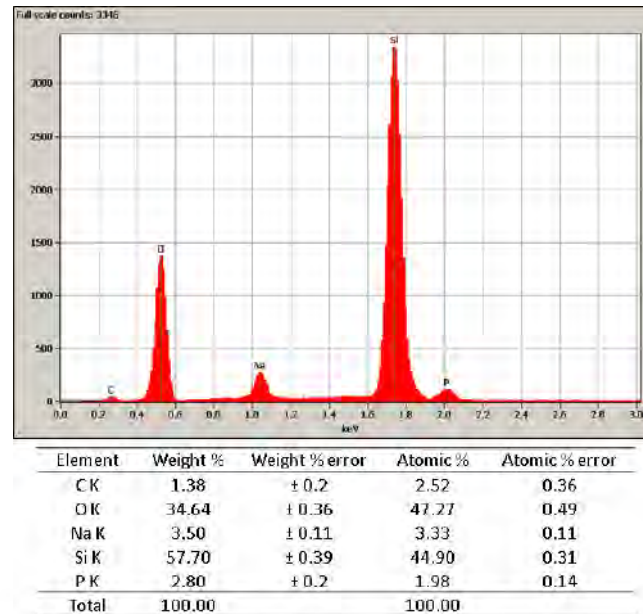
Figure 4.20: EDS at 10kV analysis of graphene channel (close to the edge) after addition of the probe.

The characterization contemplates up to this point how the surface of the sensing element is for its next use as a sensing element with a "DNA Target" sample or a "Non-complementary DNA" sample.

4.5 Nanostructured sensing element + "DNA Target"

The FESEM images in Figure 4.21(A) performed at 10 kV, detector setting of SE(M) and at 50X presented the same pattern that when the linker and the oligonucleotide were added, given the compatibility between the "DNA Target" and the probe the correct hybridization was carried out, resulting in a homogeneous surface free from defects or non-hybridization elements. Figures 4.21(B) and (D) performed at 10 kV, detector setting of SE(M) and at 1000X and 4500X respectively show the central zone of the graphene channel where a homogeneous surface is observed free of defects. On the other hand, Figures 4.21(C) and (E) performed at 10 kV, detector setting of SE(U,LA100) and at 1000X and 4500X respectively depict the same salt agglomerations of the previous step but in greater quantity, these elements belong to the PBS solution used for the probe and for the "DNA Target". Despite these salts segregated the area is homogeneous on its surface.

Figure 4.21: 10kV FESEM images of the graphene channel with the addition of the "DNA Target".(A) 50X - SE(M). The images to the left (B) and (D) correspond to the central area of the GFET using SE(M) at 1000X and 4500X respectively. The images to the right (C) and (E) correspond to the edge of the GFET using SE(U,LA100) at 1000X and 4500X respectively.

The AFM analysis of the graphene channel is shown in the Figure 4.22, the large white spots could be attributable to the agglomeration of probes or linker molecules, even though the density of inmmobilized probes was not directly measured, the change in roughness indicate the hybridization of "DNA Target" to probes on the limited graphene surface. Thus the surfaces roughness of the surface increased from 1.430 nm in the annealing graphene to 2.306 nm with the probe and finally reaches 2.622 nm with the "DNA Target" demonstrating an affinity between the elements, similar behavior has been demonstrated by Yeon Hwa Hwak et al. [115], Shi-Rui Guo et al. [116] and Jin Heak Jung et al. [117].
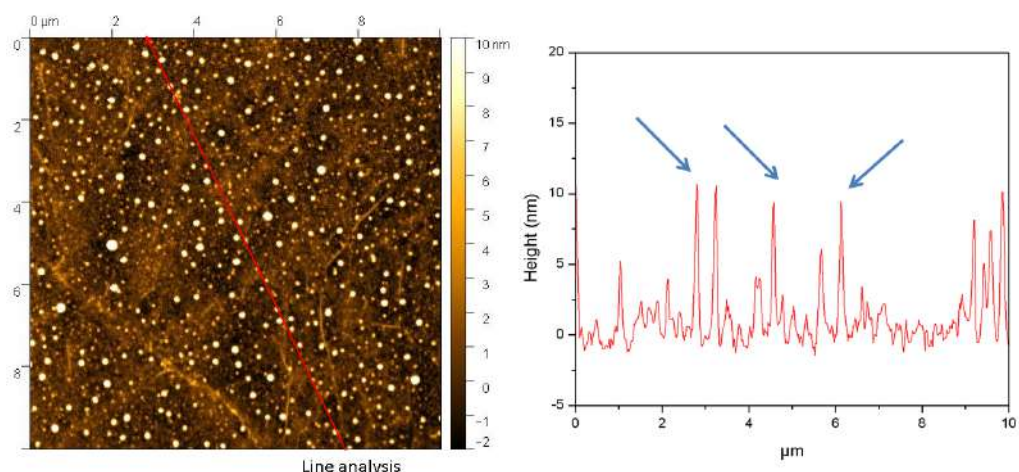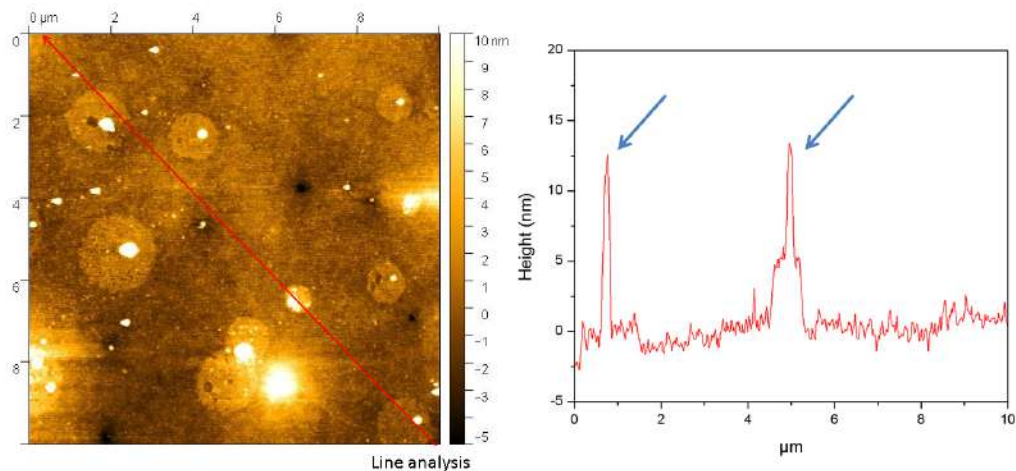

Figure 4.22: AFM image of graphene channel after addition of "DNA Target"(left) and line analysis (right).

A EDS at 10 kV was performed over the graphene channel also in two different zones, in the middle and close to the edge. The results in Figure 4.23 performed in the middle show an increase in sodium concentration to 0.26 in weight % and the results of Figure 4.34 performed in the edges also show an increase in sodium and phosphorus concentration to 12.40 and 7.60 weight % respectively. This result is due to the addition of the "DNA Target" on the surface associated with the increase of the salt concentration which come from the phosphate buffer solution.

Element	Weight %	Weight % error	Atomic %	Atomic % error
C K	1.90	± 0.18	3.48	0.33
O K	33.36	± 0.32	45.83	0.44
Na K	0.26	± 0.05	0.25	0.05
Si K	64.47	± 0.36	50.45	0.28
Total	100.00		100.00	
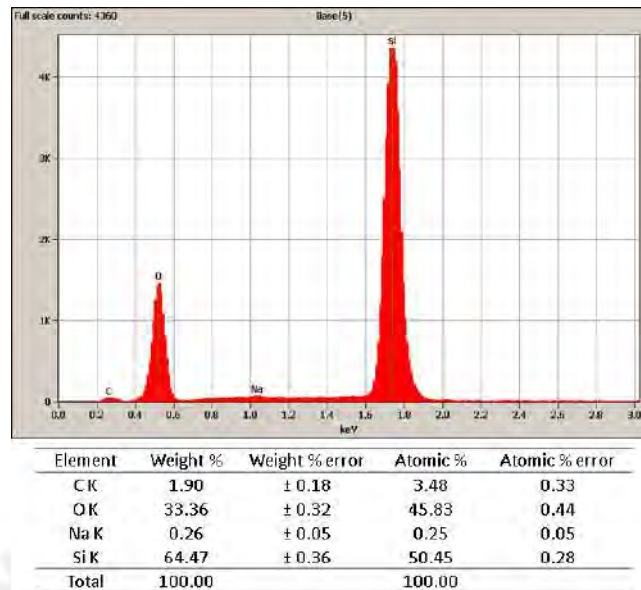
Figure 4.23: EDS at 10 kV analysis of graphene channel (middle) after addition of "DNA Target".

Element	Weight %	Weight % error	Atomic %	Atomic % error
C K	5.21	± 0.21	8.76	0.36
O K	39.59	± 0.38	50.03	0.47
Na K	12.40	± 0.17	10.90	0.15
Si K	35.21	± 0.33	25.35	0.23
P K	7.60	± 0.25	4.96	0.13
Total	100.00		100.00	
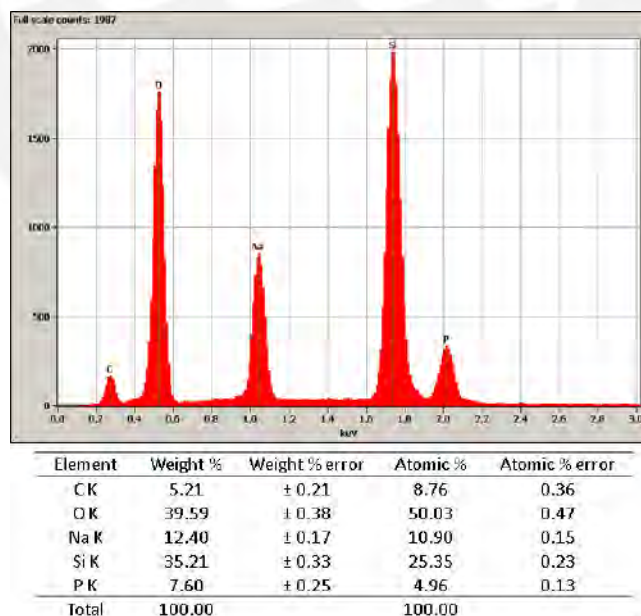
Figure 4.24: EDS at 10kV analysis of graphene channel (close to the edge) after addition of "DNA Target".

The spectrum Raman allowed to understand the structure of the interaction zone, Figure 4.25 shows a spectrum of silicon which is the pattern of the Raman spectrometer that helps as a basis for the following spectra, it must be taken into account that the corresponding peaks in the range of 493 cm^{-1} and 531 cm^{-1} correspond to the peak of $\sim$520 cm^{-1} characteristic of silicon. Two different areas over the graphene channel were analyzed, designated as C1 and C2. Figure 4.27 (C1 area) shows the Raman spectrum where it is assumed that the peaks marked with red correspond to at assigned frequencies of DNA taking as reference Benavides et al. research [130]. The peak $\sim$615 cm^{-1} is assigned to the presence of adedine, cytosine and thymine; the peak 678 cm^{-1} to guanine and thymine. Figure 4.27 (C2 area) can be seen the same peak of $\sim$615 cm^{-1} and another of 1342 cm^{-1} which is assigned to adenine and guanine. Additionally, the Raman Spectroscopy can confirm the doping after functionalization by linker molecules. The G and 2D bands decreased from 1592 and 2690 to 1585 and 2685 cm^{-1} in the C2 area shown in the Figures 4.28 and 4.29 for the G and 2D bands respectively. Based on the research developed by Das et al. [131] and Jin Heak Jung et al. [117] on the characteristics of the G and 2D bands. it can be concluded that the G band has a different behavior to electron and hole doping nevertheless the decrease in the 2D band is presumed to be assigned to the increase in n doping.
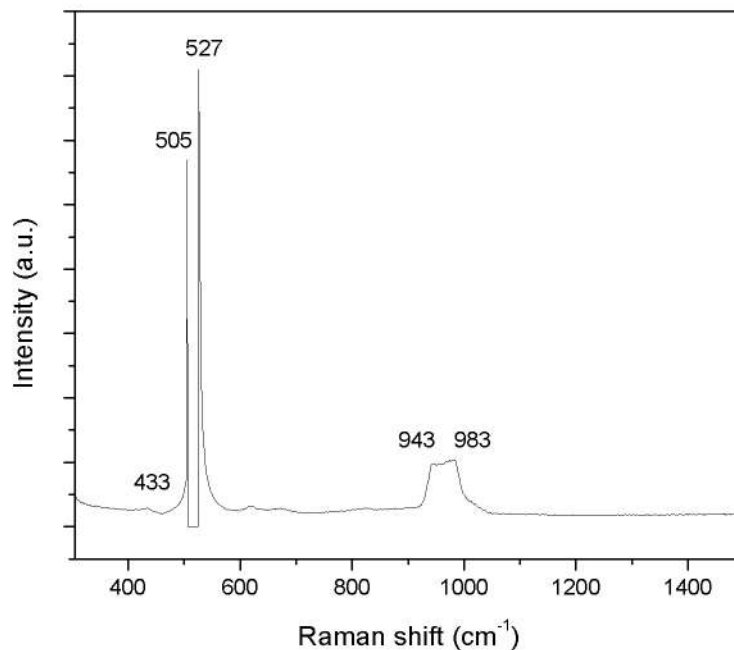
Figure 4.25: Silicon spectrum pattern of the Raman spectrometer.
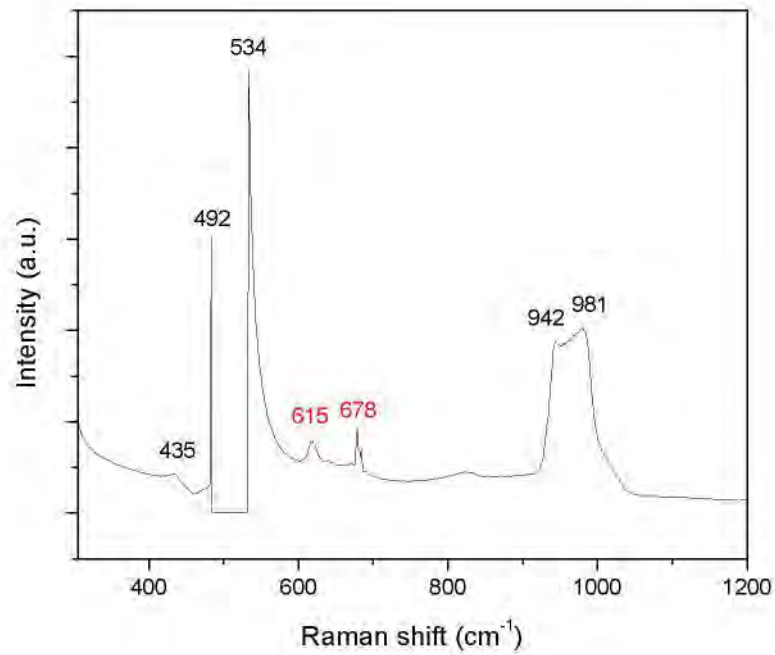
Figure 4.26: Raman spectra of the nanostructure sensing element over the graphene channel for C1 area.
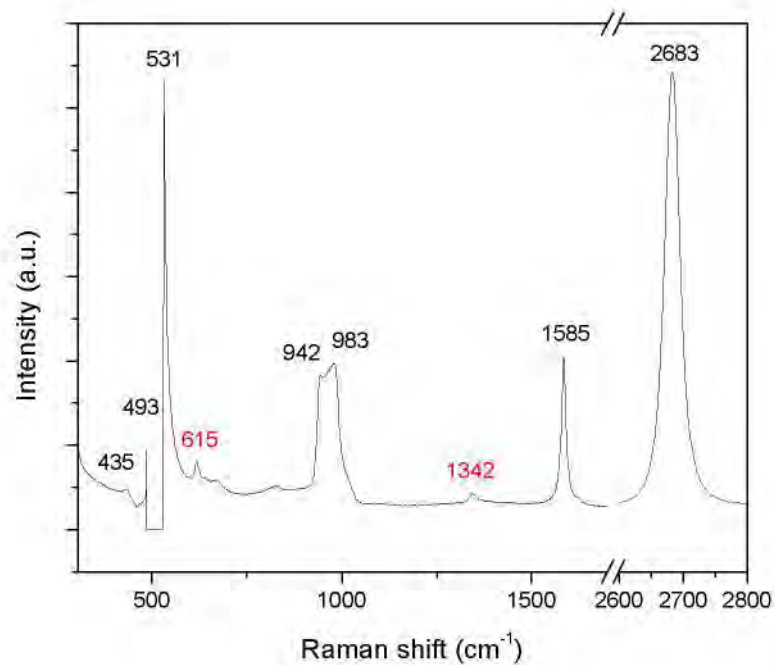
Figure 4.27: Raman spectra of the nanostructure sensing element over the graphene channel for C2 area.
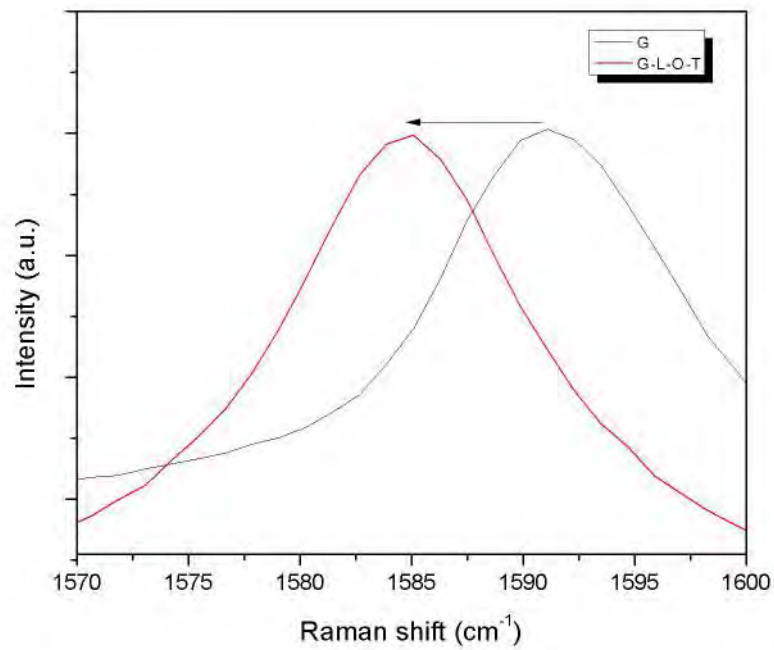
Figure 4.28: The variations in the Raman spectra in G band position.
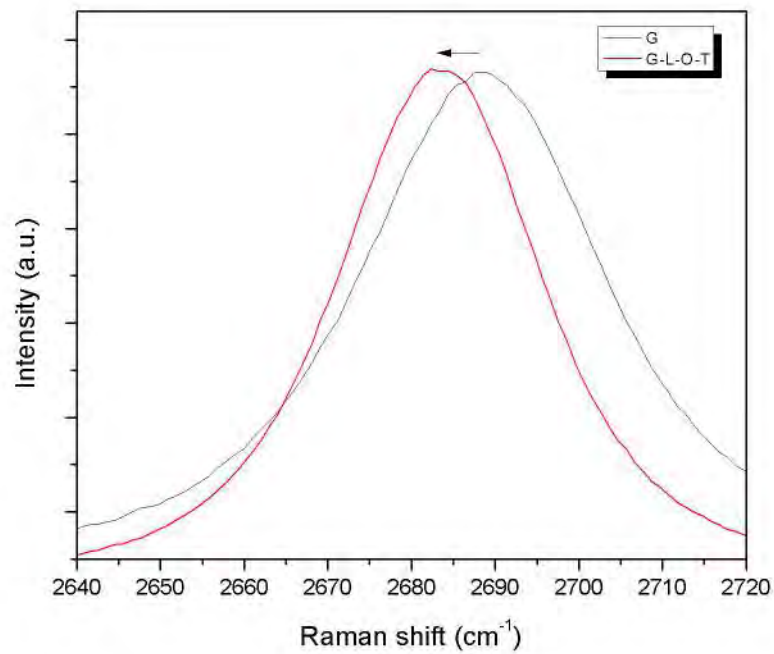
Figure 4.29: The variations in the Raman spectra in 2D band position.

Comparing a complementary thesis in relation to the electronic properties, Rojas et al. [129] developed the I-V curves of two identical transistors (sensing elements), designated as D1 and D2. D1 was evaluated in all the stages of the fabrication process while d2 was evaluated only at the G-L-O and G-L-O-T conditions. Figures 4.30(A) and (B) show the I-V curves for transistors D1 and D2 ($I_d = f(V_d)$). For D1 transistor the I_d-V_d slopes are identical for all three G, G-L and G-L-O states, and lower for G-L-O-T state; a decrease of 24% is evidenced. For D2, a similar decrease in the slope of G-L-O-T compared to the G-L-O state is registered (26%). This behavior has been widely discussed in the literature and it has been proposed that DNA introduction produces an n doping effect on the graphene corroborated with decrease of the band 2D in the raman spectrum (see Figure 4.29). The displacements are attributed to the linkage of the pyrene group of the linker with the graphene by π-π interactions, to the bonding of the linker ester group with the aminated termination of the DNA recognition sequence (probe) and finally to the hybridization of the recognition DNA sequences and objective. It can be concluded that after functionalization of the graphene surfaces with the linker molecules through π-π interactions, probes for the detection of tuberculosis were successfully attached on linker functionalized graphene channels due to the response generated by the "DNA Target".
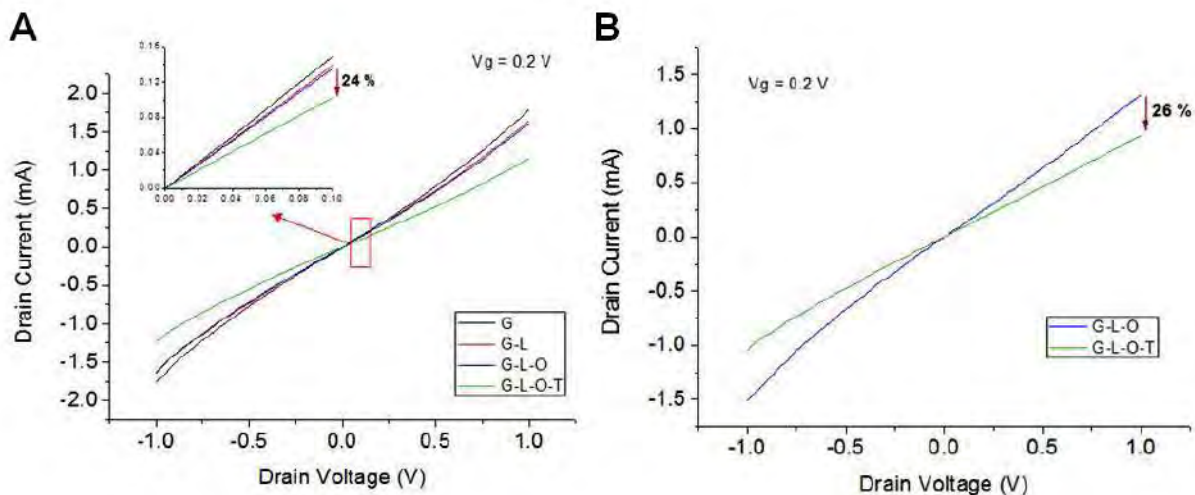
Figure 4.30: I-V curves for transistors D1 (A) and D2 (B) obtained at different fabrication stages. G-L-O-T indicates the DNA hybridization stage, "DNA Target" concentrations was 0.01 nM[129].

4.6 Nanostructured sensing element + "Non-complementary DNA"

Case totally opposite to the FESEM Figure 4.21 where the "DNA Target" was added, now instead of the "DNA Target" the "Non-complementary DNA" was added being this macro-molecule incompatible with the structure developed. The FESEM results are observed in Figure 4.31(A) performed at 10 kV, detector setting of SE(M) and at 50X where it can be seen a heterogeneous surface with an appreciate products derived from salts over the graphene channel. Figures 4.31(B) and (D) performed at 10 kV, detector setting of SE(M) and at 1000X and 4500X respectively show the central zone of the graphene channel where a heterogeneous surface is observed with different defects from the salts belonging to the PBS solutions. The same pattern is observed in Figures 4.31(C) and (E) performed at 10 kV, detector setting of SE(U,LA100) and at 1000X and 4500X respectively where they show the same salt agglomerations found in the central zone belonging to the salts of the PBS solution with a considerable increase of them unlike the previous stages also it is observed that these salt segregates are heterogeneously dispersed throughout the surface of the edges.

The AFM analysis in Figure 4.32 shows specific areas with residues with height of ∼25-30 nm, which can be attributed to the inhibition of effective hybridization of probe molecules with the "Non-complementary DNA" due to the inherent difficulty of affinity of the nitrogenous sequences that compose them. The AFM line analysis image shows a remarkably increased roughness from 2.306 with the probe to a 6.606 nm, comparatively higher than the 2.622 nm obtained with the addition of the "DNA Target".

An EDS analysis at 10 kV was perfomed over the graphene channel area also in two different zones, in the middle and close to the edge. The results follow the same pattern as the previous ones, Figure 4.19 performed in the middle shows an increase in sodium concentration to 1.03 in weight % but also a small amount of phosphorus of 0.81 in weight %. Additionally the results of Figure 4.20 performed in the edges also show an increase in sodium and phosphorus concentration to 27.10 and 17.13 weight % respectively. These results show a noticeable increase in the concentration of the salts compared to the previous stages, this is due to the poor interaction between the probe and the "Non-complementary DNA" increasing the number of elements segregated in the surface, thus showing more agglomerations of salts.
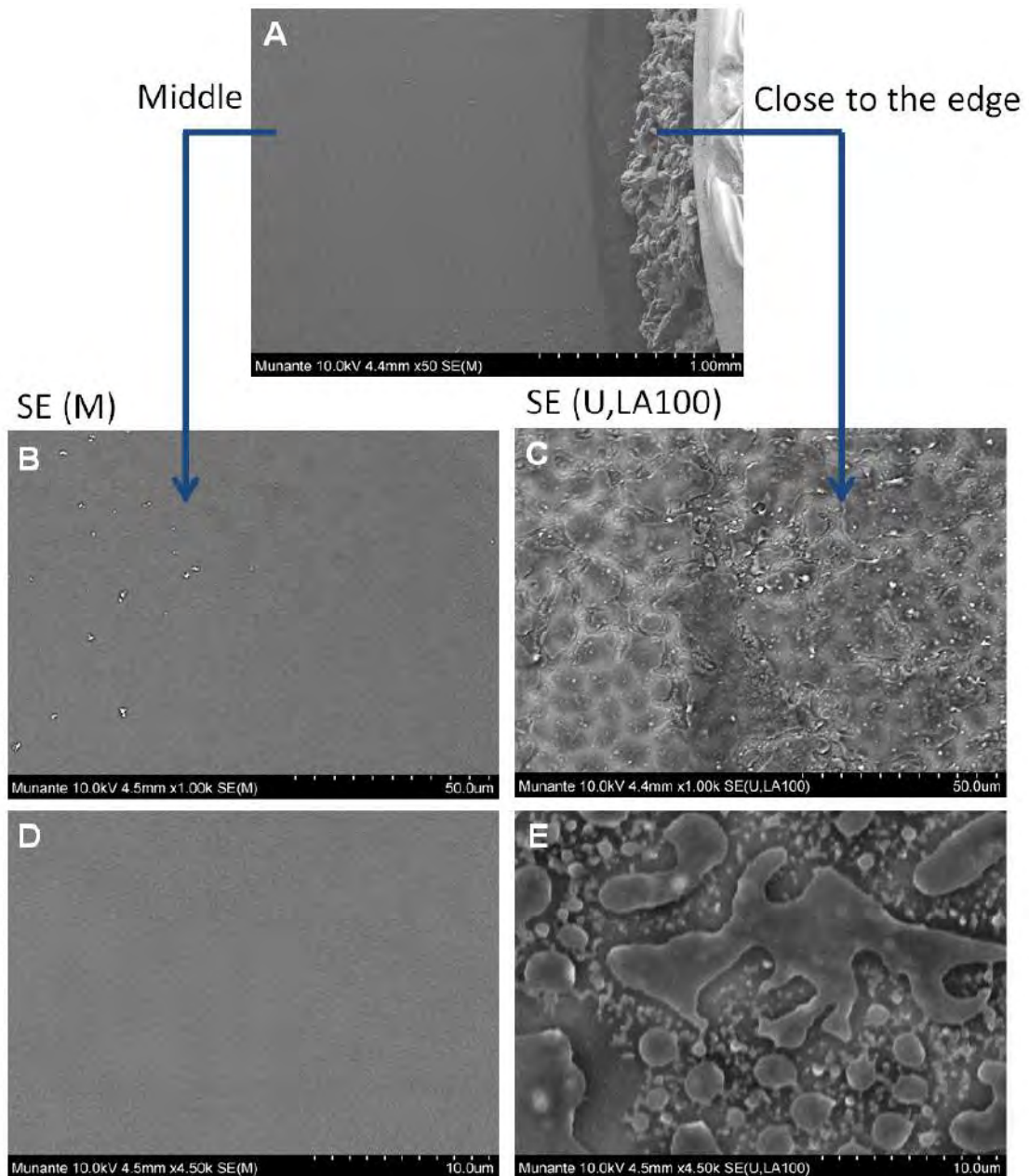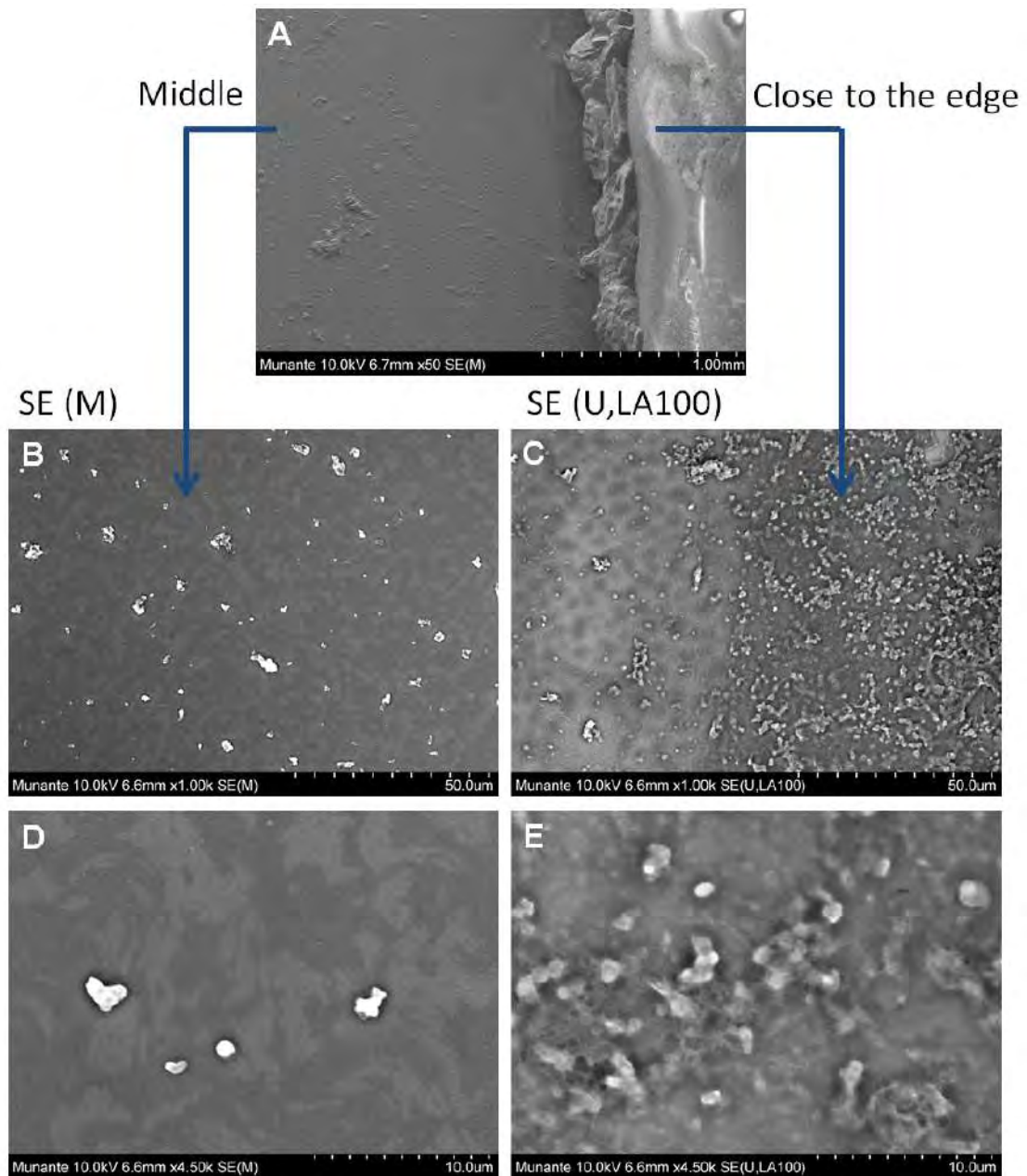
Figure 4.31: 10kV FESEM images of the graphene channel with the addition of the "Non-complementary DNA". (A) 50X - SE(M). The images to the left (B) and (D) correspond to the central area of the GFET using SE(M) at 1000X and 4500X respectively. The images to the right (C) and (E) correspond to the edge of the GFET using SE(U,LA100) at 1000X and 4500X respectively.
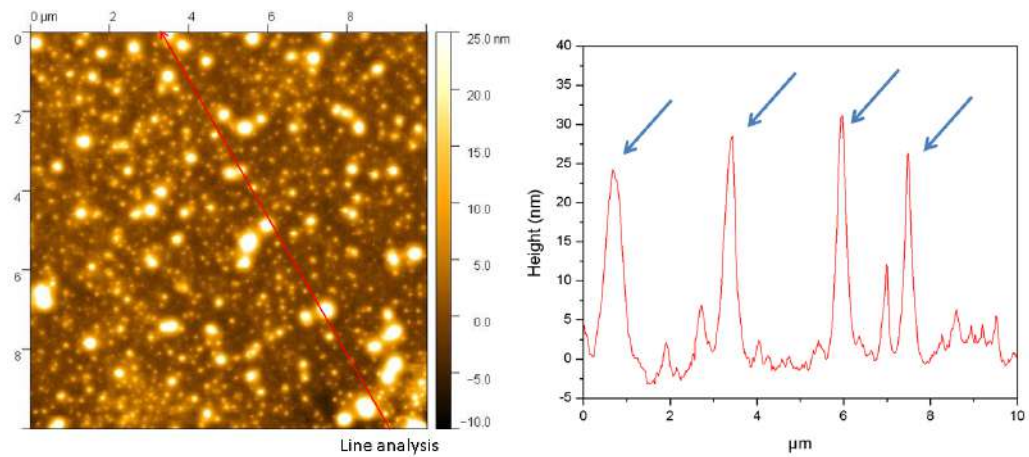
Figure 4.32: AFM image of graphene channel after addition of "Non-complementary DNA" (left) and line analysis (right).

Element	Weight %	Weight % error	Atomic %	Atomic % error
C K	1.32	± 0.19	2.43	0.34
O K	33.36	± 0.33	46.06	0.46
Na K	1.03	± 0.09	0.99	0.08
Si K	63.49	± 0.37	49.94	0.29
P K	0.81	± 0.16	0.57	0.11
Total	100.00		100.00	
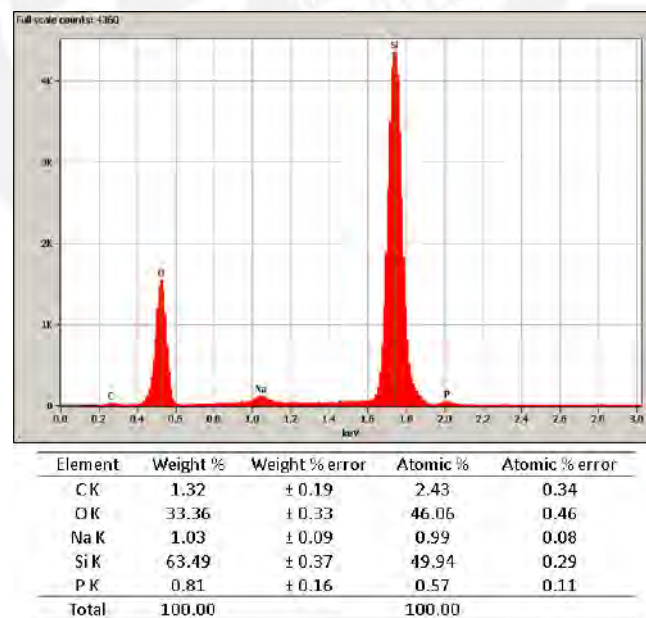
Figure 4.33: EDS at 10 kV analysis of graphene channel (middle) after addition of "Non-complementary DNA".

Element	Weight %	Weight % error	Atomic %	Atomic % error
C K	4.06	± 0.26	6.60	0.42
O K	44.82	± 0.43	54.75	0.52
Na K	27.10	± 0.26	23.04	0.22
Si K	6.90	± 0.22	4.80	0.15
P K	17.13	± 0.32	10.81	0.20
Total	100.00		100.00	
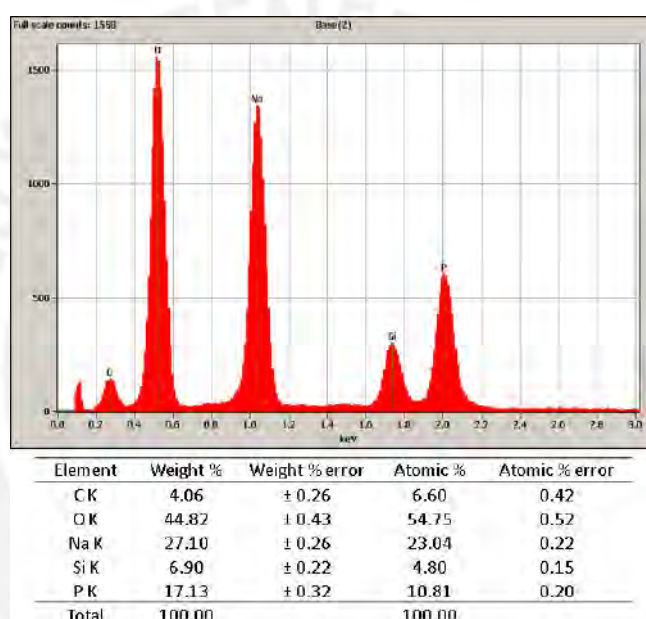
Figure 4.34: EDS at 10kV analysis of graphene channel (close to the edge) after addition of "Non-complementary DNA".

5 Conclusions and Future Work

From the work presented in this thesis, the following are the most important conclusions and possible future works that will allow to improve the performance of the sensing element.

5.1 Conclusions

- Has been successfully fabricated a graphene based FET-like sensing element for the detection of tuberculosis.

- A structural, chemical and morphological characterization of the fabricated element in each stage of the manufacturing process, has been performed. This was satisfactorily attained by enlightening the behavior of the different elements added thanks to specialized characterization techniques.

- The advanced characterization techniques used in the present work complement each other by the fact that information revealed by one, in which assumptions can be made, can be corroborated and validated by another. Raman spectroscopy facilitated the verification of the graphene structure, the detection of possible defects in it, the possible behavior to doping of the surface and the DNA presence. Optical microscopy showed the basic morphology of the graphene substrate. The analysis by FESEM corroborated the information of the optical microscopy showing also the homogeneity of the surface in the different stages of the manufacturing process but also the presence of salt segregates in the edges of the sensing element corroborated by the EDS analysis when evaluating its chemical composition. The LSM facilitated the obtaining of how the Au electrodes were distributed over the graphene surface and their height. The AFM analysis corroborates the homogeneity of the surface and helped evaluate the probe binding verification and the "DNA Target" hybridization.

- The initial characterization of the substrate is fundamental to be able to evaluate its future performance as a sensing element and evaluate the next stage in the manufacturing process. The Raman spectrum pointed out the presence of monolayer graphene, both the FESEM and AFM image showed the presence of common defects in the surface and some environmental contaminants. This aided in improving the fabrication process with an annealing, where AFM analysis reveals an increase in the homogeneity of the graphene surface, which is corroborated by several investigations that a surface

with less defects free of impurities will have a better behavior in its use as a sensing element.

- It is possible to enlighten that the process of manufacture was adequate since in the results in the FESEM and AFM a homogeneous surface is observed in the step of the addition of the linker (interaction π-π) and the step of the addition of the probe (functionalization) observing an increase in roughness.

- The affinity in the hybridization between the DNA probe and the "DNA Target" is concluded, since a homogeneous surface is observed in the center of the sample demonstrated by FESEM and AFM analysis, unlike when the "Non-complementary DNA" is added where a heterogeneous surface is observed with the presence of segregated salts on the entire surface.

- It is possible to appreciate a difference in the behavior of the sensing element for the detection of the "DNA Target" and the non-compatibility with the "Non-complementary DNA", both for its electrical characteristics and its morphology, despite the presence of salt segregations produced by the phosphate buffer solution (PBS) observed in the FESEM and EDS.

- The FESEM and EDS analysis revealed the presence of segregated agglomerates of salt accumulated at the edge of the sample corroborated with their morphology and the chemical analysis, it is possible that these elements vary the behavior of the sensing element in service although the AFM analysis at nanometric scale performed in the center of the graphene channels show a similar behavior developed by different investigations, with an increase in roughness of 1.430 nm of annealing graphene to 2.622 nm with the "DNA Target". However the analysis of the electronic properties show a good behavior that can possibly be improved by eliminating those elements.

- The Raman spectroscopy is a great tool used for many researchers for the analysis of the graphene surface due to the behavior of the D, G and 2D bands, also for the possible n or p doping over the surface, for the effect that the annealing may cause by measure the D band that is related to the defects over the surface and for the analysis of the signal given by the oligonucleotides added. In the present thesis G and 2D bans (1592 and 2690 cm^{-1}) and the intensity 2D/G ratio of about 1.4 evidenced a monolayer graphene, the decrease in the 2D band demonstrated the n doping corroborated by the I-V curves, since the annealing were performed at relative low temperature (250°C) and time (30 min) no defect due to the annealing can be observed, and finally the bands $\sim$615, 678 and 1342 cm^{-1} corroborate the presence of DNA over the surface.

5.2 Future work

- In the process of deposition of the gold electrodes, the mask used was home made. The improvement of the dimensions of this mask could be investigated to improve the area of interaction analyzing possible changes in the electronic characteristics. Likewise a finer and more accurate deposition would be achieved with a lithographic process.

- In the present investigation, only one probe sequence of oligonucleotide was used, an investigation can be followed with other similar sequences to observe its behavior and improvement in the sensing element. A research currently being developed is comparing two related sequences evaluating their electronic properties.

- In the results shown, especially in the deposition of the probe and the "DNA Target", the presence of salt segregations pertaining to the PBS solution was observed. A more detailed study of the concentrations of the solutions should be carried out. Also a change in technique to add the solutions must be analyzed, since the drop casting technique does not leave a totally homogeneous surface a possible alternative to investigate could be spin coating.

- In the process of deposition of the "DNA Target" a good hybridization is desired. This step is fundamental for the correct interaction of the probe with the corresponding sequences belonging to the complementary sequences of the "DNA Target". Different factors can influence to achieve this, one of them is a homogeneous graphene channel surface achieved by the annealing. Another important factor to investigate in detail is the correct temperature at which the "DNA Target" is added.

- A further investigation of the behavior of the Raman spectra by changing different characteristics in the manufacturing process can be made. For example by changing the temperature and time in the annealing process evaluating the D band for defects, changes in the functionalization process for the evaluation of p or n doping evaluating the G and 2D band behavior, changes In the selected DNA sequences revealing characteristic bands.

- The work presented was done with a single concentration of "DNA Target". A more detailed investigation should be carried out with different concentrations to evaluate the sensitivity of the sensing element and its behavior at all levels.

Bibliography

[1] TELENTI, A. ; IMBODEN, P. ; MARCHESI, F. ; MATTER, L. ; SCHOPFER, K. ; BODMER, T. ; LOWRIE, D. ; COLSTON, M. J. ; COLE, S.: Detection of rifampicin-resistance mutations in Mycobacterium tuberculosis. In: *The Lancet* 341 (1993), Nr. 8846, S. 647–651. `http://dx.doi.org/10.1016/0140-6736(93)90417-F`. – DOI 10.1016/0140–6736(93)90417–F. – ISBN 0140–6736

[2] CASTRO, Kenneth G. ; LOBUE, Philip: Bridging implementation, knowledge, and ambition gaps to eliminate tuberculosis in the united states and globally. In: *Emerging Infectious Diseases* 17 (2011), Nr. 3, S. 337–342. `http://dx.doi.org/10.3201/eid1703.110031`. – DOI 10.3201/eid1703.110031. – ISBN 1080–6040\r1080–6059

[3] WHO: Global Tuberculosis Report 2014. In: *WHO Report* 2014 (2014), Nr. 4, 171. `http://dx.doi.org/10.1155/2014/187842`. – DOI 10.1155/2014/187842. – ISBN 9789241564809

[4] ZHANG, Zehua ; LI, Litao ; LUO, Fei ; CHENG, Peng ; WU, Feng ; WU, Zheng ; HOU, Tianyong ; ZHONG, Min ; XU, Jianzhong: Rapid and accurate detection of RMP- and INH-resistant Mycobacterium tuberculosis in spinal tuberculosis specimens by CapitalBio™ DNA microarray: a prospective validation study. In: *BMC infectious diseases* 12 (2012), Nr. 1, 303. `http://dx.doi.org/10.1186/1471-2334-12-303`. – DOI 10.1186/1471–2334–12–303. – ISBN 1471–2334 (Electronic)\r1471–2334 (Linking)

[5] WANG, Hong ; CHEN, Hui-Wen ; HUPERT, Mateusz L. ; CHEN, Pin-Chuan ; DATTA, Proyag ; PITTMAN, Tana L. ; GOETTERT, Jost ; MURPHY, Michael C. ; WILLIAMS, Diana ; BARANY, Francis ; SOPER, Steven a.: Fully Integrated Thermoplastic Genosensor for the Highly Sensitive Detection and Identification of Multi-Drug-Resistant Tuberculosis. In: *Angewandte Chemie (International ed. in English)* (2012), 4349–4353. `http://dx.doi.org/10.1002/anie.201200732`. – DOI 10.1002/anie.201200732. – ISBN 1521–3773 (Electronic)\r1433–7851 (Linking)

[6] ZHOU, Jia: Electrochemical biosensor based on modified graphene oxide for tuberculosis diagnosis. In: *2011 9th IEEE International Conference on ASIC* (2011), 653–656. `http://dx.doi.org/10.1109/ASICON.2011.6157290`. – DOI 10.1109/ASICON.2011.6157290. – ISBN 978–1–61284–193–9

[7] OHNO, Yasuhide ; MAEHASHI, Kenzo ; MATSUMOTO, Kazuhiko: Chemical and biological sensing applications based on graphene field-effect transistors. In: *Biosensors and Bioelectronics* 26 (2010), Nr. 4, 1727–1730. `http://dx.doi.org/10.1016/j.bios.2010.08.001`. – DOI 10.1016/j.bios.2010.08.001. – ISBN 1873–4235 (Electronic)\n0956–5663 (Linking)

[8] Chiu, Nan-Fu ; Huang, Teng-Yi ; Kuo, Chun-Chuan ; Lee, Wei-Che ; Hsieh, Min-Hua ; Lai, Hsin-Chih: Single-Layer Graphene based SPR biochips for tuberculosis bacillus detection. In: *Proc. of SPIE Vol. 8427* 8427 (2012), 84273M–84273M–7. `http://dx.doi.org/10.1117/12.922698`. – DOI 10.1117/12.922698. – ISBN 9780819491190

[9] Li, Fang ; Yu, Yuqi ; Li, Qi ; Zhou, Ming ; Cui, Hua: A homogeneous signal-on strategy for the detection of rpoB genes of Mycobacterium tuberculosis based on electrochemiluminescent graphene oxide and ferrocene quenching. In: *Analytical Chemistry* 86 (2014), Nr. 3, S. 1608–1613. `http://dx.doi.org/10.1021/ac403281g`. – DOI 10.1021/ac403281g. – ISBN 1520–6882 (Electronic)\n0003–2700 (Linking)

[10] Yue, Weiwei ; Jiang, Shouzhen ; Xu, Shicai ; Bai, Chengjie: Fabrication of integrated field-effect transistors and detecting system based on CVD grown graphene. In: *Sensors and Actuators, B: Chemical* 195 (2014), 467–472. `http://dx.doi.org/10.1016/j.snb.2014.01.071`. – DOI 10.1016/j.snb.2014.01.071. – ISBN 0925–4005

[11] Kwak, Yeon H. ; Choi, Dong S. ; Kim, Ye N. ; Kim, Hyeongkeun ; Yoon, Dae H. ; Ahn, Sang S. ; Yang, Ji W. ; Yang, Woo S. ; Seo, Sungkyu: Flexible glucose sensor using CVD-grown graphene-based field effect transistor. In: *Biosensors and Bioelectronics* 37 (2012), Nr. 1, 82–87. `http://dx.doi.org/10.1016/j.bios.2012.04.042`. – DOI 10.1016/j.bios.2012.04.042. – ISBN 0956–5663

[12] C. Corbella Roca: Thin Film Structures of Diamond-Like Carbon Prepared By Pulsed Plasma Techniques. In: *Thesis in Universitat de Barcelona. Departament de Física Aplicada i Òptica* (2006)

[13] Iijima, Sumio: *Helical microtubules of graphitic carbon*

[14] Neto, Antonio C. ; Guinea, Francisco ; Peres, Nuno M.: Drawing conclusions from graphene. In: *Physics World* 19 (2006), Nr. 11, S. 33–37. `http://dx.doi.org/[193.171.33.83`. – DOI [193.171.33.83. – ISBN 0953–8585

[15] Weber, J. W. ; Calado, V. E. ; Van De Sanden, M. C M.: Optical constants of graphene measured by spectroscopic ellipsometry. In: *Applied Physics Letters* 97 (2010), Nr. 9. `http://dx.doi.org/10.1063/1.3475393`. – DOI 10.1063/1.3475393. – ISBN 2001501005

[16] Heyrovska, Raji: Atomic Structures of Graphene, Benzene and Methane with Bond Lengths as Sums of the Single, Double and Resonance Bond Radii of Carbon. In: *arXiv preprint arXiv:0804.4086* (2008), 1–4. `http://dx.doi.org/10.2174/1874199100802010001`. – DOI 10.2174/1874199100802010001. – ISSN 18741991

[17] Lemme, M: Current Status of Graphene Transistors. In: *Diffusion and defect data. Solid state data. Part B* (2010), 1–12. `http://dx.doi.org/10.4028/www.scientific.net/SSP.156-158.499`. – DOI 10.4028/www.scientific.net/SSP.156–158.499. – ISSN 1662–9779

[18] SINGH, Virendra ; JOUNG, Daeha ; ZHAI, Lei ; DAS, Soumen ; KHONDAKER, Saiful I. ; SEAL, Sudipta: Graphene based materials: Past, present and future. In: *Progress in Materials Science* 56 (2011), Nr. 8, 1178–1271. `http://dx.doi.org/10.1016/j.pmatsci.2011.03.003`. – DOI 10.1016/j.pmatsci.2011.03.003. – ISBN 0079–6425

[19] LEE, Changgu ; WEI, Xiaoding ; KYSAR, Jeffrey W. ; HONE, James ; =: Measurement of the Elastic Properties and Intrinsic Strength of Monolayer Graphene. In: *Science* 321 (2008), Nr. 18 July 2008, S. 385–388. `http://dx.doi.org/10.1126/science.1157996`. – DOI 10.1126/science.1157996. – ISBN 0036–8075

[20] LEE, Changgu ; WEI, Xiaoding ; LI, Qunyang ; CARPICK, Robert ; KYSAR, Jeffrey W. ; HONE, James: Elastic and frictional properties of graphene. In: *Physica Status Solidi (B)* 246 (2009), Nr. 11, 2562–2567. `http://dx.doi.org/10.1002/pssb.200982329`. – DOI 10.1002/pssb.200982329. – ISBN 1521–3951

[21] FRANK, I. W. ; TANENBAUM, D. M. ; ZANDE, Arend M. d. ; MCEUEN, Paul L.: Mechanical properties of suspended graphene sheets. In: *Journal of Vacuum Science & Technology B: Microelectronics and Nanometer Structures* 25 (2007), Nr. 6, S. 2558. `http://dx.doi.org/10.1116/1.2789446`. – DOI 10.1116/1.2789446. – ISBN 1071–1023

[22] TSOUKLERI, Georgia ; PARTHENIOS, John ; PAPAGELIS, Konstantinos ; JALIL, Rashid ; FERRARI, Andrea C. ; GEIM, Andre K. ; NOVOSELOV, Kostya S. ; GALIOTIS, Costas: Subjecting a graphene monolayer to tension and compression. In: *Small* 5 (2009), Nr. 21, S. 2397–2402. `http://dx.doi.org/10.1002/smll.200900802`. – DOI 10.1002/smll.200900802. – ISBN 1613–6829

[23] VAN LIER, Gregory ; VAN ALSENOY, Christian ; VAN DOREN, Vic ; GEERLINGS, Paul: Ab initio study of the elastic properties of single-walled carbon nanotubes and graphene. In: *Chemical Physics Letters* 326 (2000), Nr. 1-2, 181–185. `http://dx.doi.org/10.1016/S0009-2614(00)00764-8`. – DOI 10.1016/S0009–2614(00)00764–8. – ISBN 0009–2614

[24] REDDY, C D. ; RAJENDRAN, S ; LIEW, K M.: Equilibrium configuration and continuum elastic properties of finite sized graphene. In: *Nanotechnology* 17 (2006), Nr. 3, S. 864–870. `http://dx.doi.org/10.1088/0957-4484/17/3/042`. – DOI 10.1088/0957–4484/17/3/042. – ISBN 0957–4484

[25] NIKA, D. L. ; POKATILOV, E. P. ; ASKEROV, A. S. ; BALANDIN, A. A.: Phonon thermal conduction in graphene: Role of Umklapp and edge roughness scattering. In: *Physical Review B - Condensed Matter and Materials Physics* 79 (2009), Nr. 15, S. 1–12. `http://dx.doi.org/10.1103/PhysRevB.79.155413`. – DOI 10.1103/PhysRevB.79.155413. – ISBN 1098–0121

[26] JIANG, Jin-Wu ; LAU, Jinghua ; WANG, Jian-sheng ; LI, Baowen ; LAN, Jinghua ; WANG, Jian-sheng ; LI, Baowen: Isotopic effects on the thermal conductivity of graphene nanoribbons: localization mechanism. In: *Arxiv:1007.5358V1* 054314 (2010), Nr. 2010, 9–13. `http://dx.doi.org/10.1063/1.3329541`. – DOI 10.1063/1.3329541. – ISBN 0021–8979

[27] GOENKA, Sumit ; SANT, Vinayak ; SANT, Shilpa: Graphene-based nanomaterials for drug delivery and tissue engineering. In: *Journal of Controlled Release* 173 (2014), Nr. 1, 75–88. `http://dx.doi.org/10.1016/j.jconrel.2013.10.017`. – DOI 10.1016/j.jconrel.2013.10.017. – ISBN 1873–4995 (Electronic)\r0168–3659 (Linking)

[28] MAHANTA, Nayandeep K. ; ABRAMSON, Alexis R.: Thermal conductivity of graphene and graphene oxide nanoplatelets. In: *13th InterSociety Conference on Thermal and Thermomechanical Phenomena in Electronic Systems* (2012), 1–6. `http://dx.doi.org/10.1109/ITHERM.2012.6231405`. – DOI 10.1109/ITHERM.2012.6231405. – ISBN 978–1–4244–9532–0

[29] KIM, P ; SHI, L ; MAJUMDAR, A ; MCEUEN, P L.: Thermal Transport Measurements of Individual Multiwalled Nanotubes. In: *Physical Review Letters* 87 (2001), Nr. 21, 215502. `http://dx.doi.org/10.1103/PhysRevLett.87.215502`. – DOI 10.1103/PhysRevLett.87.215502. – ISBN 0031–9007

[30] E., Pop ; D., Mann ; Q., Wang ; K., Goodson ; H, Dai: Thermal Conductance of an Individual Single-Wall Carbon Nanotube above Room Temperature. In: *Nano Lett.* 6 (2006), Nr. 1, S. 96. `http://dx.doi.org/10.1021/nl052145f`. – DOI 10.1021/nl052145f. – ISSN 1530–6984

[31] SCHWAMB, Timo ; BURG, Brian R. ; SCHIRMER, Niklas C. ; POULIKAKOS, Dimos: An electrical method for the measurement of the thermal and electrical conductivity of reduced graphene oxide nanostructures. In: *Nanotechnology* 20 (2009), Nr. 40, S. 405704. `http://dx.doi.org/10.1088/0957-4484/20/40/405704`. – DOI 10.1088/0957–4484/20/40/405704. – ISBN 0957–4484

[32] BALANDIN, Alexander A. ; GHOSH, Suchismita ; BAO, Wenzhong ; CALIZO, Irene ; TEWELDEBRHAN, Desalegne ; MIAO, Feng ; LAU, Chun N.: Superior thermal conductivity of single-layer graphene. In: *Nano Letters* 8 (2008), Nr. 3, S. 902–907. `http://dx.doi.org/10.1021/nl0731872`. – DOI 10.1021/nl0731872. – ISBN 1530–6984

[33] GHOSH, S. ; CALIZO, I. ; TEWELDEBRHAN, D. ; POKATILOV, E. P. ; NIKA, D. L. ; BALANDIN, A. A. ; BAO, W. ; MIAO, F. ; LAU, C. N.: Extremely high thermal conductivity of graphene: Prospects for thermal management applications in nanoelectronic circuits. In: *Applied Physics Letters* 92 (2008), Nr. 15, S. 2–4. `http://dx.doi.org/10.1063/1.2907977`. – DOI 10.1063/1.2907977. – ISBN 0003–6951

[34] SEOL, Jae H. ; SEOL, Jae H. ; JO, Insun ; MOORE, Arden L. ; LINDSAY, Lucas ; AITKEN, Zachary H. ; PETTES, Michael T. ; LI, Xuesong ; YAO, Zhen ; HUANG, Rui ; BROIDO, David ; MINGO, Natalio: Two-Dimensional Phonon Transport in Supported Graphene. 213 (2010), Nr. 2010. `http://dx.doi.org/10.1126/science.1184014`. – DOI 10.1126/science.1184014. – ISSN 0036–8075

[35] BAE, Sukang ; KIM, Hyeongkeun ; LEE, Youngbin ; XU, Xiangfan ; PARK, Jae-Sung ; ZHENG, Yi ; BALAKRISHNAN, Jayakumar ; LEI, Tian ; RI KIM, Hye ; SONG, Young I. ; KIM,

Young-Jin ; Kim, Kwang S. ; Özyilmaz, Barbaros ; Ahn, Jong-Hyun ; Hong, Byung H. ; Iijima, Sumio: Roll-to-roll production of 30-inch graphene films for transparent electrodes. In: *Nature Nanotechnology* 5 (2010), Nr. 8, 574–578. `http://dx.doi.org/10.1038/nnano.2010.132`. – DOI 10.1038/nnano.2010.132. – ISBN 1748–3387

[36] Nair, R. R. ; Blake, P. ; Grigorenko, a. N. ; Novoselov, K. S. ; Booth, T. J. ; Stauber, T. ; Peres, N. M. R. ; Geim, a. K.: Fine Structure Constant Defines Visual Transperency of Graphene. In: *Science* 320 (2008), Nr. June, S. 2008. `http://dx.doi.org/10.1126/science.1156965`. – DOI 10.1126/science.1156965. – ISBN 0036–8075

[37] Kravets, V. G. ; Grigorenko, A. N. ; Nair, R. R. ; Blake, P. ; Anissimova, S. ; Novoselov, K. S. ; Geim, A. K.: Spectroscopic ellipsometry of graphene and an exciton-shifted van Hove peak in absorption. In: *Physical Review B - Condensed Matter and Materials Physics* 81 (2010), Nr. 15, S. 1–6. `http://dx.doi.org/10.1103/PhysRevB.81.155413`. – DOI 10.1103/PhysRevB.81.155413. – ISBN 1098–0121

[38] Gonzalez Carmona, J. ; Hernandez, M.ª A. ; Guinea, F: Electronica del grafeno. In: *Investigacion y Ciencia* 408 (2010), 42–49. `http://www.investigacionyciencia.es/files/6818.pdf{%}5Cnhttp://www.investigacionyciencia.es/investigacion-y-ciencia/numeros/2010/9/electrnica-del-grafeno-8316`

[39] Novoselov, K S. ; Geim, A K. ; Morozov, S V. ; Jiang, D ; Katsnelson, M I. ; Grigorieva, I V. ; Dubonos, S V. ; Firsov, A A.: Two-dimensional gas of massless Dirac fermions in graphene. In: *Nature* 438 (2005), Nr. 7065, 197–200. `http://dx.doi.org/10.1038/nature04233`. – DOI 10.1038/nature04233. – ISBN 9780080431529

[40] Berger, Claire ; Song, Zhimin ; Li, Xuebin ; Wu, Xiaosong ; Brown, Nate ; Naud, Cécile ; Mayou, Didier ; Li, Tianbo ; Hass, Joanna ; Marchenkov, Alexei N. ; Conrad, Edward H. ; First, Phillip N. ; Heer, Walt A.: Electronic Confinement and Coherence in Patterned Epitaxial Graphene. In: *Science* 312 (2006), Nr. 5777, 1191–1196. `http://dx.doi.org/10.1126/science.1125925`. – DOI 10.1126/science.1125925. – ISBN 0036–8075

[41] Bolotin, K. I. ; Sikes, K. J. ; Jiang, Z. ; Klima, M. ; Fudenberg, G. ; Hone, J. ; Kim, P. ; Stormer, H. L.: Ultrahigh electron mobility in suspended graphene. In: *Solid State Communications* 146 (2008), Nr. 9-10, S. 351–355. `http://dx.doi.org/10.1016/j.ssc.2008.02.024`. – DOI 10.1016/j.ssc.2008.02.024. – ISBN 0038–1098

[42] Morozov, S. V. ; Novoselov, K. S. ; Katsnelson, M. I. ; Schedin, F. ; Elias, D. C. ; Jaszczak, J. A. ; Geim, A. K.: Giant intrinsic carrier mobilities in graphene and its bilayer. In: *Physical Review Letters* 100 (2008), Nr. 1, S. 11–14. `http://dx.doi.org/10.1103/PhysRevLett.100.016602`. – DOI 10.1103/PhysRevLett.100.016602. – ISBN 0031–9007

[43] Hwang, E. H. ; Adam, S. ; Sarma, S. D.: Carrier transport in two-dimensional graphene layers. In: *Physical Review Letters* 98 (2007), Nr. 18, S. 2–5. `http://dx.doi.org/10.1103/PhysRevLett.98.186806`. – DOI 10.1103/PhysRevLett.98.186806. – ISBN 0031–9007

[44] ARTILES, Mayra S. ; ROUT, Chandra S. ; FISHER, Timothy S.: Graphene-based hybrid materials and devices for biosensing. In: *Advanced Drug Delivery Reviews* 63 (2011), Nr. 14-15, 1352–1360. `http://dx.doi.org/10.1016/j.addr.2011.07.005`. – DOI 10.1016/j.addr.2011.07.005. – ISBN 1872–8294 (Electronic)\r0169–409X (Linking)

[45] NGUYEN, Phong ; BERRY, Vikas: Graphene interfaced with biological cells: Opportunities and challenges. In: *Journal of Physical Chemistry Letters* 3 (2012), Nr. 8, S. 1024–1029. `http://dx.doi.org/10.1021/jz300033g`. – DOI 10.1021/jz300033g. – ISBN 1948–7185

[46] ZHONG, M ; XU, D ; YU, X ; HUANG, K ; LIU, X ; QU, Y ; XU, Y ; YANG, D: Interface coupling in graphene/fluorographene heterostructure for high-performance graphene/silicon solar cells. In: *Nano Energy* 28 (2016), 12–18. `http://dx.doi.org/10.1016/j.nanoen.2016.08.031`. – DOI 10.1016/j.nanoen.2016.08.031. – ISSN 22112855 (ISSN)

[47] AKINWANDE, Deji ; TAO, Li ; YU, Qingkai ; LOU, Xiaojing ; PENG, Peng ; KUZUM, Duygu: Large-Area Graphene Electrodes: Using CVD to facilitate applications in commercial touch-screens, flexible nanoelectronics, and neural interfaces. In: *IEEE Nanotechnology Magazine* 9 (2015), Nr. 3, S. 6–14. `http://dx.doi.org/10.1109/MNANO.2015.2441105`. – DOI 10.1109/MNANO.2015.2441105. – ISSN 19324510

[48] LALWANI, Gaurav ; HENSLEE, Allan M. ; FARSHID, Behzad ; LIN, Liangjun ; KASPER, Fred K. ; QIN, Yi-Xian ; MIKOS, Antonios G. ; SITHARAMAN, Balaji: Two-Dimensional Nanostructure- Reinforced Biodegradable Polymeric Nanocomposites for Bone Tissue Engineering. In: *Biomacromolecules* (2013). `http://dx.doi.org/10.1021/bm301995s`. – DOI 10.1021/bm301995s. – ISSN 1526–4602

[49] RAFIEE, Mohammad A. ; RAFIEE, Javad ; WANG, Zhou ; SONG, Huaihe ; YU, Zhong Z. ; KORATKAR, Nikhil: Enhanced mechanical properties of nanocomposites at low graphene content. In: *ACS Nano* 3 (2009), Nr. 12, S. 3884–3890. `http://dx.doi.org/10.1021/nn9010472`. – DOI 10.1021/nn9010472. – ISBN 19360851

[50] LIU, Zhang ; ROBINSON, Joshua T. ; SUN, Xiaoming ; DAI, Hongjie: PEGylated Nano-Graphene Oxide for Delivery of Water Insoluble Cancer Drugs (b). In: *J Am Chem Soc* 130 (2008), Nr. 33, S. 10876–10877. `http://dx.doi.org/10.1021/ja803688x`. – DOI 10.1021/ja803688x. – ISBN 1160011605

[51] YANG, Kai ; WAN, K J. ; ZHANG, K S. ; ZHANG, Youjiu ; LEE, Shuit-tong ; LIU, Zhuang: PEGylated Graphene in Mice. In: *ACS Nano* 5 (2011), Nr. 1, S. 516–522

[52] NOVOSELOV, K. S. ; GEIM, A. K. ; MOROZOV, S.V. ; JIANG, D. ; ZHANG, Y. ; DUBONOS, S. V. ; GRIGORIEVA, I. V. ; FIRSOV, A. A.: Electric Field Effect in Atomically Thin Carbon Films. In: *Science* 306 (2004), Nr. 5696, 666–669. `http://dx.doi.org/10.1126/science.1102896`. – DOI 10.1126/science.1102896. – ISBN 0036–8075

[53] SCHEDIN, F. ; GEIM, A.K. ; MOROZOV, S.V. ; HILL, E W. ; BLAKE, P. ; KATSNELSON, M.I. ; NOVOSELOV, K.S.: Detection of individual gas molecules adsorbed on graphene. In:

Nature materials 6 (2007), Nr. 9, 652–5. `http://dx.doi.org/10.1038/nmat1967`. – DOI 10.1038/nmat1967. – ISBN 1476–1122

[54] Chen, Tzu-Yin ; Loan, Phan Thi K. ; Hsu, Chang-Lung ; Lee, Yi-Hsien ; Tse-Wei Wang, Jacob ; Wei, Kung-Hwa ; Lin, Cheng-Te ; Li, Lain-Jong: Label-free detection of DNA hybridization using transistors based on CVD grown graphene. In: *Biosensors & bioelectronics* 41 (2013), 103–9. `http://dx.doi.org/10.1016/j.bios.2012.07.059`. – DOI 10.1016/j.bios.2012.07.059. – ISBN 0956–5663

[55] Huang, Yinxi ; Dong, Xiaochen ; Liu, Yuxin ; Li, Lain-Jong ; Chen, Peng: Graphene-based biosensors for detection of bacteria and their metabolic activities. In: *Journal of Materials Chemistry* 21 (2011), S. 12358–12362. `http://dx.doi.org/10.1039/c1jm11436k`. – DOI 10.1039/c1jm11436k. – ISBN 0959–9428

[56] Soldano, Caterina ; Mahmood, Ather ; Dujardin, Erik: Production, properties and potential of graphene. In: *Carbon* 48 (2010), Nr. 8, 2127–2150. `http://dx.doi.org/10.1016/j.carbon.2010.01.058`. – DOI 10.1016/j.carbon.2010.01.058. – ISBN 0008–6223

[57] Geim, a K.:   Status and Prospects. In: *Science* 324 (2009), Nr. June, 1530–1534. `http://dx.doi.org/10.1126/science.1158877`. – DOI 10.1126/science.1158877. – ISBN 0036–8075

[58] Robinson, Jeremy T. ; Perkins, F K. ; Snow, Eric S. ; Wei, Zhongqing ; Sheehan, Paul E. ; Robinson, Jeremy T. ; Perkins, F K. ; Snow, Eric S. ; Wei, Zhongqing ; Sheehan, Paul E.: Reduced Graphene Oxide Molecular Sensors. 8 (2008), Nr. September, S. 3137–3140. `http://dx.doi.org/10.1021/nl8013007`. – DOI 10.1021/nl8013007

[59] Bunch, J S. ; Zande, Arend M. d. ; Verbridge, Scott S. ; Frank, Ian W. ; Tanenbaum, David M. ; Parpia, Jeevak M. ; Craighead, Harold G. ; McEuen, Paul L.: Electromechanical resonators from graphene sheets. In: *Science (New York, N.Y.)* 315 (2007), Nr. 5811, 490–3. `http://dx.doi.org/10.1126/science.1136836`. – DOI 10.1126/science.1136836. – ISBN 1095–9203

[60] Jones, Authors A. ; Ph, D ; Safron, Nathaniel: Mechanical Exfoliation to Make Graphene and Visualization Mechanical Exfoliation to Make Graphene and Visualization. (2004), S. 2–4

[61] Vaziri, Sam: *Fabrication and Characterization of Graphene Field Effect Transistors*, Diss., 2011

[62] Heer, Walt A. ; Berger, Claire ; Wu, Xiaosong ; First, Phillip N. ; Conrad, Edward H. ; Li, Xuebin ; Li, Tianbo ; Sprinkle, Michael ; Hass, Joanna ; Sadowski, Marcin L. ; Potemski, Marek ; Martinez, Gérard: Epitaxial graphene. In: *Solid State Communications* 143 (2007), Nr. 1-2, S. 92–100. `http://dx.doi.org/10.1016/j.ssc.2007.04.023`. – DOI 10.1016/j.ssc.2007.04.023. – ISBN 0038–1098

[63] BERGER, Claire ; SONG, Zhimin ; LI, Tianbo ; LI, Xuebin ; OGBAZGHI, Asmerom Y. ; FENG, Rui ; DAI, Zhenting ; MARCHENKOV, Alexei N. ; CONRAD, Edward H. ; FIRST, Phillip N. ; HEER, Walt a.: Ultrathin Epitaxial Graphite: 2D Electron Gas Properties and a Route toward Graphene-based Nanoelectronics. In: *Journal of Physical Chemistry B* 108 (2004), Nr. 52, 19912–19916. `http://dx.doi.org/doi:10.1021/jp040650f`. – DOI doi:10.1021/jp040650f. – ISBN 1520–6106

[64] GOGNEAU, N. ; TRABELSI, A.B.G. ; SILLY, M.G. ; RIDENE, M. ; PORTAIL, M. ; MICHON, A. ; OUESLATI, M. ; BELKHOU, R. ; SIROTTI, F. ; OUERGHI, A.: Investigation of structural and electronic properties of epitaxial graphene on 3C?SiC(100)/Si(100) substrates. In: *Nanotechnology, Science and Applications* 7 (2014), S. 85–95. `http://dx.doi.org/10.2147/NSA.S60324`. – DOI 10.2147/NSA.S60324. – ISSN 11778903

[65] MATTEVI, Cecilia ; KIM, Hokwon: A review of chemical vapour deposition of graphene on copper. In: *J. Mater. Chem.* 21 (2011), Nr. 10, 3324–3334. `http://dx.doi.org/10.1039/C0JM02126A`. – DOI 10.1039/C0JM02126A. – ISBN 0959–9428

[66] OBRAZTSOV, A. N. ; OBRAZTSOVA, E. A. ; TYURNINA, A. V. ; ZOLOTUKHIN, A. A.: Chemical vapor deposition of thin graphite films of nanometer thickness. In: *Carbon* 45 (2007), Nr. 10, S. 2017–2021. `http://dx.doi.org/10.1016/j.carbon.2007.05.028`. – DOI 10.1016/j.carbon.2007.05.028. – ISBN 0008–6223

[67] REINA, Alfonso ; JIA, Xiaoting ; HO, John ; NEZICH, Daniel ; SON, Hyungbin ; BULOVIC, Vladimir ; DRESSELHAUS, Mildred S. ; JING, Kong: Large area, few-layer graphene films on arbitrary substrates by chemical vapor deposition. In: *Nano Letters* 9 (2009), Nr. 1, S. 30–35. `http://dx.doi.org/10.1021/nl801827v`. – DOI 10.1021/nl801827v. – ISBN 1530–6984

[68] KIM, Keun S. ; ZHAO, Yue ; JANG, Houk ; LEE, Sang Y. ; KIM, Jong M. ; KIM, Kwang S. ; AHN, Jong-hyun ; KIM, Philip ; CHOI, Jae-young ; HONG, Byung H.: Large-scale pattern growth of graphene films for stretchable transparent electrodes. In: *Nature* 457 (2008), Nr. 7230, 706–710. `http://dx.doi.org/10.1038/nature07719`. – DOI 10.1038/nature07719. – ISSN 0028–0836

[69] LI, Xiaolin ; ZHANG, Guangyu ; BAI, Xuedong ; SUN, Xiaoming ; WANG, Xinran ; WANG, Enge ; DAI, Hongjie: Highly conducting graphene sheets and Langmuir – Blodgett films. 3 (2008), Nr. September, S. 1–5. `http://dx.doi.org/10.1038/nnano.2008.210`. – DOI 10.1038/nnano.2008.210

[70] NOVOSELOV, K S. ; FAL'KO, V I. ; COLOMBO, L ; GELLERT, P R. ; SCHWAB, M G. ; KIM, K: A roadmap for graphene. In: *Nature* 490 (2012), Nr. 7419, 192–200. `http://dx.doi.org/10.1038/nature11458`. – DOI 10.1038/nature11458. – ISBN 1476–4687 (Electronic)\r0028–0836 (Linking)

[71] ZHU, Hongying ; SUTER, Jonathan D. ; WHITE, Ian M. ; FAN, Xudong: Aptamer Based Microsphere Biosensor for Thrombin Detection. In: *Sensors* 6 (2006), Nr. 8, S. 785–795. `http://dx.doi.org/10.3390/s6080785`. – DOI 10.3390/s6080785. – ISBN 0157388425

[72] Wojcik, Peter M.: *Fabrication and Characterization of a Label Free Graphene Field Effect Transistor Biosensor*, Diss., 2012

[73] Curreli, Marco ; Zhang, Rui ; Ishikawa, Fumiaki N. ; Chang, Hsiao-kang ; Cote, Richard J. ; Zhou, Chongwu ; Thompson, Mark E.: Real-Time , Label-Free Detection of Biological Entities Using Nanowire-Based FETs. 7 (2008), Nr. 6, S. 651–667

[74] Ingebrandt, S ; Offenhausser, a: Label-free detection of DNA using field-effect transistors. In: *Physica Status Solidi A - Applications and Materials Science* 203 (2006), Nr. 14, S. 3399–3411. http://dx.doi.org/10.1002/pssa.200622465. – DOI 10.1002/pssa.200622465. – ISBN 0031–8965

[75] Wang, Wayne U. ; Chen, Chuo ; Lin, Keng-hui ; Fang, Ying ; Lieber, Charles M.: Label-free detection of small-molecule-protein interactions by using nanowire nanosensors. In: *Proceedings of the National Academy of Sciences of the United States of America* 102 (2005), Nr. 9, S. 3208–3212. http://dx.doi.org/10.1073/pnas.0406368102. – DOI 10.1073/pnas.0406368102. – ISBN 0027–8424 (Print)\r0027–8424 (Linking)

[76] Ohno, Yasuhide ; Maehashi, Kenzo ; Matsumoto, Kazuhiko: Label-free biosensors based on aptamer-modified graphene field-effect transistors. In: *Journal of the American Chemical Society* 132 (2010), Nr. 51, S. 18012–18013. http://dx.doi.org/10.1021/ja108127r. – DOI 10.1021/ja108127r. – ISBN 0002–7863

[77] Gowtham, S. ; Scheicher, Ralph H. ; Ahuja, Rajeev ; Pandey, Ravindra ; Karna, Shashi P.: Physisorption of nucleobases on graphene: Density-functional calculations. In: *Physical Review B - Condensed Matter and Materials Physics* 76 (2007), Nr. 3, S. 2–5. http://dx.doi.org/10.1103/PhysRevB.76.033401. – DOI 10.1103/PhysRevB.76.033401. – ISBN 1098–0121

[78] Lin, Cheng-Te ; Loan, Phan Thi K. ; Chen, Tzu-Yin ; Liu, Keng-Ku ; Chen, Chang-Hsiao ; Wei, Kung-Hwa ; Li, Lain-Jong: Label-Free Electrical Detection of DNA Hybridization on Graphene using Hall Effect Measurements: Revisiting the Sensing Mechanism. In: *Advanced Functional Materials* 23 (2013), Nr. 18, 2301–2307. http://dx.doi.org/10.1002/adfm.201202672. – DOI 10.1002/adfm.201202672. – ISBN 1111111111

[79] Yun, Je M. ; Kim, Kyoung N. ; Kim, Ju Y. ; Shin, Dong O. ; Lee, Won J. ; Lee, Sun H. ; Lieberman, Marya ; Kim, Sang O.: DNA origami nanopatterning on chemically modified graphene. In: *Angewandte Chemie - International Edition* 51 (2012), Nr. 4, S. 912–915. http://dx.doi.org/10.1002/anie.201106198. – DOI 10.1002/anie.201106198. – ISBN 1521–3773

[80] Varghese, Neenu ; Mogera, Umesha ; Govindaraj, Achutharao ; Das, Anindya ; Maiti, Prabal K. ; Sood, Ajay K. ; Rao, C. N R.: Binding of DNA nucleobases and nucleosides with graphene. In: *ChemPhysChem* 10 (2009), Nr. 1, S. 206–210. http://dx.doi.org/10.1002/cphc.200800459. – DOI 10.1002/cphc.200800459. – ISBN 1439–4235

[81] LU, Chun H. ; YANG, Huang H. ; ZHU, Chun L. ; CHEN, Xi ; CHEN, Guo N.: A graphene platform for sensing biomolecules. In: *Angewandte Chemie - International Edition* 48 (2009), Nr. 26, S. 4785–4787. http://dx.doi.org/10.1002/anie.200901479. – DOI 10.1002/anie.200901479. – ISBN 1521–3773

[82] HOBZA, P.: Stacking interactions. In: *Phys. Chem. Chem. Phys.* 10 (2008), S. 2581–2583. http://dx.doi.org/10.1039/B805489B. – DOI 10.1039/B805489B. – ISBN 1463–9076

[83] OHNO, Yasuhide ; MAEHASHI, Kenzo ; INOUE, Koichi ; MATSUMOTO, Kazuhiko: Label-free aptamer-based immunoglobulin sensors using graphene field-effect transistors. In: *Japanese Journal of Applied Physics* 50 (2011), Nr. 7 PART 1. http://dx.doi.org/10.1143/JJAP.50.070120. – DOI 10.1143/JJAP.50.070120. – ISBN 0021–4922

[84] OHNO, Yasuhide ; MAEHASHI, Kenzo ; YAMASHIRO, Yusuke ; MATSUMOTO, Kazuhiko: Electrolyte-Gated Graphene Field-Effect Transistors for Detecting pH and Protein Adsorption. (2009), S. 2–6

[85] HER, Jim L. ; PAN, Tung M. ; LIN, Wan Y. ; WANG, Kai S. ; LI, Lain J.: Label-free detection of alanine aminotransferase using a graphene field-effect biosensor. In: *Sensors and Actuators, B: Chemical* 182 (2013), 396–400. http://dx.doi.org/10.1016/j.snb.2013.03.026. – DOI 10.1016/j.snb.2013.03.026. – ISSN 09254005

[86] MAEHASHI, Kenzo ; SOFUE, Yasuyuki ; OKAMOTO, Shogo ; OHNO, Yasuhide ; INOUE, Koichi ; MATSUMOTO, Kazuhiko: Selective ion sensors based on ionophore-modified graphene field-effect transistors. In: *Sensors and Actuators, B: Chemical* 187 (2013), 45–49. http://dx.doi.org/10.1016/j.snb.2012.09.033. – DOI 10.1016/j.snb.2012.09.033. – ISSN 09254005

[87] HUANG, Yinxi ; DONG, Xiaochen ; LIU, Yuxin ; LI, Lain-Jong ; CHEN, Peng: Graphene-based biosensors for detection of bacteria and their metabolic activities. In: *Journal of Materials Chemistry* 21 (2011), Nr. 33, S. 12358. http://dx.doi.org/10.1039/c1jm11436k. – DOI 10.1039/c1jm11436k. – ISBN 0959–9428

[88] SKOOG: *Summary for Policymakers*. Bd. 6. 2008. – 1–30 S. http://dx.doi.org/10.1017/CBO9781107415324.004. http://dx.doi.org/10.1017/CBO9781107415324.004. – ISBN 9788578110796

[89] GOLDSTEIN, Joseph ; NEWBURY, Dale E. ; JOY, David C. ; LYMAN, Charles E. ; ECHLIN, Patrick ; LIFSHIN, Eric ; SAWYER, Linda ; MICHAEL, J R.: *Scanning Electron Microscopy and X-ray Microanalysis*. 2003. – 689 S. – ISBN 0306472929

[90] GAO, Libo ; REN, Wencai ; LI, Feng ; CHENG, Hui M.: Total color difference for rapid and accurate identification of graphene. In: *ACS Nano* 2 (2008), Nr. 8, S. 1625–1633. http://dx.doi.org/10.1021/nn800307s. – DOI 10.1021/nn800307s. – ISBN 1936–0851

[91] NI, Z H. ; WANG, H M. ; KASIM, J ; FAN, H M. ; YU, T ; WU, Y H. ; FENG, Y P. ; SHEN, Z X. ; ABOUT, More ; ARTICLE, This: Reflection and Contrast Spectroscopy Graphene Thickness

Determination Using Reflection and Contrast Spectroscopy. In: *Nano letters* 7 (2007), Nr. 9, S. 2758–2763. `http://dx.doi.org/10.1021/nl071254m`. – DOI 10.1021/nl071254m. – ISSN 1530–6984, 1530–6992

[92] Ni, Z. ; Wang, Y. ; Yu, T. ; Shen, Z.: Raman spectroscopy and imaging of graphene. In: *Nano Research* 1 (2008), Nr. 4, 273–291. `http://dx.doi.org/10.1007/s12274-008-8036-1`. – DOI 10.1007/s12274–008–8036–1. – ISBN 1998–0124

[93] Fabia Cristina Rossetti, Livia Vieira D. ; Bentley, Maria Vitoria Lopes B. ; Lagali, Neil S. (Hrsg.): *Confocal Laser Microscopy - Principles and Applications inMedicine, Biology, and the Food Sciences - Chapter 6.* InTech, 2013. – 99–140 S.

[94] Meng, Fangang ; Liao, Baoqiang ; Liang, Shuang ; Yang, Fenglin ; Zhang, Hanmin ; Song, Lianfa: Morphological visualization, componential characterization and microbiological identification of membrane fouling in membrane bioreactors (MBRs). In: *Journal of Membrane Science* 361 (2010), Nr. 1-2, 1–14. `http://dx.doi.org/10.1016/j.memsci.2010.06.006`. – DOI 10.1016/j.memsci.2010.06.006. – ISBN 0376–7388

[95] Pawley, James B. (Hrsg.): *Handbook of Biological Confocal Microscopy.* Third Edit. 2015. – 956–963 S. `http://dx.doi.org/10.1017/CBO9781107415324.004`. `http://dx.doi.org/10.1017/CBO9781107415324.004`. – ISBN 9788578110796

[96] Goldstein, Gi ; Newbury, De ; Echlin, P ; Joy, Dc ; FIori, C ; Lifshin, E: *Scanning electron microscopy and microanalysis.* 1st editio. A Division of Plenum Publishing Corporation, 1981. – 679 S. – ISBN 030640768X

[97] Yao, Nan: *Handbook of Microscopy for Nanotechnology.* KLUWER ACADEMIC PUBLISHERS, 2005. – 745 S. `http://dx.doi.org/10.1016/S1369-7021(05)71039-7`. `http://dx.doi.org/10.1016/S1369-7021(05)71039-7`. – ISBN 1402080034

[98] Northern Arizona University: *Class notes: Electron Microanalysis Core Facility.* `http://nau.edu/cefns/labs/electron-microprobe/glg-510-class-notes/signals/`

[99] Binnig, G. ; Quate, C. F.: Atomic Force Microscope. In: *Physical Review Letters* 56 (1986), Nr. 9, S. 930–933. `http://dx.doi.org/10.1103/PhysRevLett.56.930`. – DOI 10.1103/PhysRevLett.56.930. – ISBN 0031–9007

[100] Eaton, Peter ; West, Paul: Atomic Force Microscopy. In: *Oxford University Press* (2010), 257. `http://dx.doi.org/10.1093/acprof:oso/9780199570454.001.0001`. – DOI 10.1093/acprof:oso/9780199570454.001.0001. – ISBN 9780199570454

[101] Maver, Uroš ; Velnar, Tomaž ; Gaberšček, Miran ; Planinšek, Odon ; Finšgar, Matjaž: Recent progressive use of atomic force microscopy in biomedical applications. In: *TrAC Trends in Analytical Chemistry* 80 (2016), 96–111. `http://dx.doi.org/10.1016/j.trac.2016.03.014`. – DOI 10.1016/j.trac.2016.03.014. – ISBN 0165–9936

[102] DRESSELHAUS, M S. ; DRESSELHAUS, G ; HOFMANN, M: Raman spectroscopy as a probe of graphene and carbon nanotubes. In: *Philosophical transactions. Series A, Mathematical, physical, and engineering sciences* 366 (2008), Nr. 1863, 231–236. `http://dx.doi.org/10.1098/rsta.2007.2155`. – DOI 10.1098/rsta.2007.2155. – ISBN 1364–503X

[103] WANG, Yan ; ALSMEYER, Daniel C. ; MCCREERY, Richard L.: of Observed Spectra. In: *Carbon* (1990), Nr. 10, S. 557–563. `http://dx.doi.org/10.1021/cm00011a018`. – DOI 10.1021/cm00011a018. – ISBN 0897–4756

[104] MANUEL, Víctor ; SOLER, Freire: *Fabrication and Characterization of Macroscopic Graphene Layers on Metallic Substrates Fabrication and Characterization of Macroscopic Graphene Layers on Metallic Substrates*, Diss.

[105] FERRARI, A. C. ; MEYER, J. C. ; SCARDACI, V. ; CASIRAGHI, C. ; LAZZERI, M. ; MAURI, F. ; PISCANEC, S. ; JIANG, D. ; NOVOSELOV, K. S. ; ROTH, S. ; GEIM, A. K.: Raman spectrum of graphene and graphene layers. In: *Physical Review Letters* 97 (2006), Nr. 18, S. 1–4. `http://dx.doi.org/10.1103/PhysRevLett.97.187401`. – DOI 10.1103/PhysRevLett.97.187401. – ISBN 0031–9007

[106] PIMENTA, M.A. ; DRESSELHAUS, G. ; DRESSELHAUS, M.S. ; CANÇADO, L.G. ; JORIO, Ado ; SAITO, R.: Studying disorder in graphite-based systems by Raman spectroscopy. In: *Physical Chemistry Chemical Physics* 9 (2007), Nr. 11, 1276–1291. `http://dx.doi.org/10.1039/b613962k`. – DOI 10.1039/b613962k. – ISBN 1463–9076

[107] NI, Zhenhua ; WANG, Yingying ; YU, Ting ; SHEN, Zexiang: Raman spectroscopy and imaging of graphene. In: *Tsinghue Pres and Springer-Verlag* (2008), 1–32. `http://dx.doi.org/10.1007/s12274-008-8036-1`. – DOI 10.1007/s12274–008–8036–1. – ISBN 1998–0124\n1998–0000

[108] BASKO, DM ; PISCANEC, S. ; FERRARI, AC: Electron-electron interactions and doping dependence of the two-phonon Raman intensity in graphene. In: *Physical Review B* 80 (2009), Nr. 16, 165413. `http://dx.doi.org/10.1103/PhysRevB.80.165413`. – DOI 10.1103/PhysRevB.80.165413. – ISBN 1098–0121

[109] NEMANICH, R. J. ; SOLIN, S. A. ; G??ERARD, D.: Raman scattering from intercalated donor compounds of graphite. In: *Physical Review B* 16 (1977), Nr. 6, S. 2965–2972. `http://dx.doi.org/10.1103/PhysRevB.16.2965`. – DOI 10.1103/PhysRevB.16.2965. – ISSN 01631829

[110] MAY, Patrick ; LAZZERI, Michele ; VENEZUELA, Pedro ; HERZIGER, Felix ; CALLSEN, Gordon ; REPARAZ, Juan S. ; HOFFMANN, Axel ; MAURI, Francesco ; MAULTZSCH, Janina: Signature of the two-dimensional phonon dispersion in graphene probed by double-resonant Raman scattering. In: *Physical Review B - Condensed Matter and Materials Physics* 87 (2013), Nr. 7, S. 1–6. `http://dx.doi.org/10.1103/PhysRevB.87.075402`. – DOI 10.1103/PhysRevB.87.075402. – ISBN 1098–0121

[111] Yoon, Duhee ; Moon, Hyerim ; Son, Young W. ; Choi, Jin S. ; Park, Bae H. ; Cha, Young H. ; Kim, Young D. ; Cheong, Hyeonsik: Interference effect on Raman spectrum of graphene on SiO2 /Si. In: *Physical Review B - Condensed Matter and Materials Physics* 80 (2009), Nr. 12, S. 1–6. `http://dx.doi.org/10.1103/PhysRevB.80.125422`. – DOI 10.1103/PhysRevB.80.125422. – ISBN 1098–0121\r1550–235X

[112] Lee, Jaesung ; Zheng, Xuqian ; Roberts, Robert C. ; Feng, Philip X L.: Scanning electron microscopy characterization of structural features in suspended and non-suspended graphene by customized CVD growth. In: *Diamond and Related Materials* 54 (2015), Nr. 1, 64–73. `http://dx.doi.org/10.1016/j.diamond.2014.11.012`. – DOI 10.1016/j.diamond.2014.11.012. – ISSN 09259635

[113] Giacchetti, Benjamin M. ; Hsu, Allen ; Wang, Han ; Kim, Ki K. ; Kong, Jing ; Palacios, Tomas.: CVD-Grown Graphene Solution-gated Field Effect Transistors for pH Sensing. In: *MRS Proceedings* 1283 (2011), Nr. Carbon-Based Electronic Devices, No pp. given. `http://dx.doi.org/10.1557/opl.2011.583`. – DOI 10.1557/opl.2011.583. – ISBN 9781618394996

[114] Saltzgaber, Grant ; Wojcik, Peter ; Sharf, Tal ; Leyden, Matthew R. ; Wardini, Jenna L. ; Heist, Christopher a. ; Adenuga, Adeniyi a. ; Remcho, Vincent T. ; Minot, Ethan D.: Scalable graphene field-effect sensors for specific protein detection. In: *Nanotechnology* 24 (2013), Nr. 35, 355502. `http://dx.doi.org/10.1088/0957-4484/24/35/355502`. – DOI 10.1088/0957–4484/24/35/355502. – ISBN 1361–6528 (Electronic)\r0957–4484 (Linking)

[115] Kwak, Yeon H. ; Choi, Dong S. ; Kim, Ye N. ; Kim, Hyeongkeun ; Yoon, Dae H. ; Ahn, Sang S. ; Yang, Ji W. ; Yang, Woo S. ; Seo, Sungkyu: Flexible glucose sensor using CVD-grown graphene-based field effect transistor. In: *Biosensors and Bioelectronics* 37 (2012), Nr. 1, 82–87. `http://dx.doi.org/10.1016/j.bios.2012.04.042`. – DOI 10.1016/j.bios.2012.04.042. – ISBN 0956–5663

[116] Guo, S R. ; Lin, J ; Penchev, M ; Yengel, E ; Ghazinejad, M ; Ozkan, C S. ; Ozkan, M: Label Free DNA Detection Using Large Area Graphene Based Field Effect Transistor Biosensors. In: *Journal of Nanoscience and Nanotechnology* 11 (2011), Nr. 6, S. 5258–5263. `http://dx.doi.org/10.1166/jnn.2011.3885`. – DOI 10.1166/jnn.2011.3885. – ISBN 1533–4880

[117] Jung, Jin H. ; Sohn, Il Y. ; Kim, Duck J. ; Kim, Bo Y. ; Jang, Mi ; Lee, Nae E.: Enhancement of protein detection performance in field-effect transistors with polymer residue-free graphene channel. In: *Carbon* 62 (2013), 312–321. `http://dx.doi.org/10.1016/j.carbon.2013.05.069`. – DOI 10.1016/j.carbon.2013.05.069. – ISBN 0008–6223; 1873–3891

[118] Organización Panamericana de la salud: Manual para el diagnóstico bacteriológico de la tuberculosis. Normas y guía técnica. parte 2 Cultivo. In: *Tuberculosis* (2008), S. 114. `http://dx.doi.org/10.2105/AJPH.21.11.1289`. – DOI 10.2105/AJPH.21.11.1289. – ISSN 1527–3288

[119] Médecins Sans Frontières: *Tuberculosis – Practical guide for clinicians, nurses, laboratory technicians and medical auxiliaries*. 5th Editio. Paris, Francia, 2014. – ISBN 2906498963

[120] Mendoza-Ticona, Alberto: Tuberculosis como enfermedad ocupacional. In: *Revista Peruana de Medicina Experimental y Salud Publica* 29 (2012), Nr. 2, S. 232–236. `http://dx.doi.org/10.4321/S1137-66272005000200014`. – DOI 10.4321/S1137–66272005000200014. – ISBN 17264634

[121] Peru-Government: *Supreme decret N° 021-2016-SA, Law N°30287*. 2016

[122] Farga, Victorino ; Caminero, José A. ; Mediterraneo (Hrsg.): *Tuberculosis*. 3rd. 2011. – 196 S.

[123] Saba, Yahir Alberto P.: *Diseño de un sistema automático de preparación de muestras de esputo para el diagnóstico de TBC*, Pontificia Universidad Católica del Perú Escuela de Posgrado, Diss., 2013

[124] Pang, Yu ; Liu, Guan ; Wang, Yufeng ; Zheng, Suhua ; Zhao, Yan L.: Combining COLD-PCR and high-resolution melt analysis for rapid detection of low-level, rifampin-resistant mutations in Mycobacterium tuberculosis. In: *Journal of Microbiological Methods* 93 (2013), Nr. 1, 32–36. `http://dx.doi.org/10.1016/j.mimet.2013.01.008`. – DOI 10.1016/j.mimet.2013.01.008. – ISBN 1872–8359 (Electronic)\n0167–7012 (Linking)

[125] *Graphenea*. `https://www.graphenea.com/collections/buy-graphene-films/products/monolayer-graphene-si02-pack-4u`

[126] *ThermoFisher Scientific*. `https://www.thermofisher.com/uk/en/home.html`

[127] Raimond, J M. ; Brune, M ; Computation, Quantum ; Martini, F D. ; Monroe, C ; Moehring, D L. ; Knight, P L. ; Plenio, M B. ; Vedral, V ; Polzik, E S. ; Variables, Continuous ; Braunstein, S L. ; Pati, A K. ; Lukin, M D. ; Cirac, I J. ; Zoller, P ; Han, C ; Xue, P ; Guo, G C. ; Polyakov, S V. ; Kuzmich, A ; Kimble, H J. ; Cirac, J I. ; Kennedy, T A B. ; Horodecki, P ; Horodecki, R ; Divincenzo, D P. ; Smolin, J A. ; Beige, A ; Kwek, L C. ; Kok, P ; Sauer, J A. ; You, L ; Zangwill, A ; Chapman, M S. ; Nielsen, M: Electric Field Effect in Atomically Thin Carbon Films. In: *Science* 306 (204), S. 20–23. `http://dx.doi.org/10.1126/science.1102896`. – DOI 10.1126/science.1102896. – ISSN 0036–8075

[128] Lee, Jaesung ; Zheng, Xuqian ; Roberts, Robert C. ; X-L Feng, Philip: Scanning electron microscopy characterization of structural features in suspended and non-suspended graphene by customized CVD growth. In: *Diamond & Related Materials* 54 (2015), S. 64–73. `http://dx.doi.org/10.1016/j.diamond.2014.11.012`. – DOI 10.1016/j.diamond.2014.11.012

[129] Rojas, Merlyn: *Caracterización de propiedades electrónicas de sensores nanoestructurados en base a carbono para la deteccion de tuberculosis*, Pontificia Universidad Católica del Perú, Diss., 2016

[130] Benevides, J. M. ; Wang, A. H. ; Marel, G. A. d. ; Boom, J. H. ; Thomas, G. J.: Crystal and Solution Structures of the B-DNA Dodecamer d(CGCAAATTTGCG) Probed by Raman Spectroscopy : Heterogeneity in the Crystal Structure Does Not Persist in the Solution Structure. In: *Biochemestry* 27 (1988), Nr. 1987, S. 931–938

[131] Das, A ; Pisana, S ; Chakraborty, B ; Piscanec, S ; Saha, S K. ; Waghmare, U V. ; Novoselov, K S. ; Krishnamurthy, H R. ; Geim, A K. ; Ferrari, A C. ; Sood, A K.: Monitoring dopants by Raman scattering in an electrochemically top-gated graphene transistor. In: *Nature nanotechnology* 3 (2008), Nr. 4, 210–215. `http://dx.doi.org/10.1038/nnano.2008.67`. – DOI 10.1038/nnano.2008.67. – ISBN 1748–3395 (Electronic)\r1748–3387 (Linking)